

Interaction of Hydrogen with Novel Carbon Materials

Thesis by

Yun Ye

In Partial Fulfillment of the Requirements
for the Degree of
Doctor of Philosophy



California Institute of Technology
Pasadena, California

2001

(Submitted August 8th, 2000)

© 2001

Yun Ye

All Rights Reserved

Acknowledgements

My most sincere thanks must go to my advisor, Professor Brent Fultz for guiding my scientific research, for being a caring mentor and a source of inspiration, support and encouragement.

I am far more grateful than a few words can express, to Dr. Channing Ahn, who has been collaborating with me on this work. He was always willing to help, to talk and listen.

Dr. Charles K. Witham patiently trained me on the Sievert's apparatus and shared with me lots useful knowledge, both in and out of the lab and office.

Dr. Robert C. Bowman, Jr., and Dr. Ratnakumar V. Bugga of the Jet Propulsion Laboratory provided a lot of useful advise on my research. I am also thankful to Dr. John Vajo at Hughes Research Laboratory, for his sharp and inspiring discussion on the work.

I would like to thank Professor. George R. Gavalas and his graduate student Re Lai for helping me with the BET measurements.

Professor George R. Rossman and Dr. Elizabeth Arredondo in Geological and Planetary Science Division kindly provided Fourier Transform Infrared equipment and guided me to operate the equipment and interpret the data.

I am grateful to Professor Glen Cass for his kindness, friendship and generosity.

The work was supported in part by the grant number DE-FG03-94ER 14493 from the DOE Office of Science, and by a gift from HRL Laboratory.

Finally I would like to thank my family and all the people at Caltech who made my life in the past five years enjoyable.

Abstract

The hydrogen storage properties of some carbon materials were studied. Graphite nanofibers (GNF) were synthesized by catalytic decomposition of ethylene and hydrogen. Catalyst supported carbon materials were prepared by impregnation process. Hydrogen desorption and adsorption properties of graphite nanofibers, single-walled carbon nanotubes (SWNT), fullerene materials and catalysts supported carbon materials were measured volumetrically using a Sievert's apparatus. The hydrogen desorption capacity of GNF was typically less than 0.2 wt.%. A phase transition between crystal SWNT and a new hydride phase was found at high pressures at 80K. The phase transition was of first order, and involved the separation of the individual tubes within a rope, exposing a high surface area for hydrogen adsorption. From the change in chemical potential of the hydrogen gas upon adsorption, we were able to calculate the cohesive van der Waals energy between the tubes as 5 meV/C atom. This is much smaller than expected from previous theoretical work, and shows that defects in the crystal structure cause large suppressions of the cohesive energy. We were able to alter this cohesive energy by changing the state of the material. Over several cycles of isotherm measurements at 77 K, the hydrogen storage capacities of one of the fullerite samples increased from an initial value of 0.4 wt% for the first cycle to a capacity of 4.2 wt% for the fourth cycle. Correspondingly, the surface area increased from 0.9 m²/gm to 11 m²/gm, and showed a phase transformation, characterized by X-ray powder diffraction. By adding Ni particles onto the sample, the hydrogen storage capacity of fullerite and activated carbon sample was increased. The adsorption of hydrogen on Ni particle can not account for the total increased capacity even by assuming complete coverage of hydrogen molecules on the Ni particle surface.

Contents

Acknowledgements	iii
Abstract	iv
1 Introduction	1
1.1 Hydrogen	1
1.1.1 General Aspects	1
1.1.2 Production of Hydrogen	3
1.1.3 Storage Methods	5
1.2 Fuel Cells	8
1.2.1 Fuel Cell Principles	9
1.2.2 Classification of Fuel Cells	9
1.2.3 Fuel Choice for Fuel Cell Vehicles	14
1.3 Carbon Materials	15
1.3.1 Graphite and Graphite Materials	15
1.3.2 Activated Carbon	19
1.3.3 Fullerenes	19
1.3.4 Nanotubes	24
1.3.5 Graphite Nanofibers	28
1.4 Physisorption and Chemisorption	29
1.4.1 Langmuir Isotherm	31
1.4.2 BET Isotherm	34
Bibliography	35
2 Experimental Techniques, Equipment, and Data Analysis	40
2.1 Sample Preparation and Modification	40

2.1.1	Nanofiber Synthesis	40
2.1.2	Krättschmer-Huffman Method - Synthesis of Fullerenes	41
2.1.3	Single-Walled Nanotubes Production	41
2.1.4	Sonication and Filtration	43
2.1.5	Catalyst Impregnation	44
2.2	Sample Characterization	47
2.2.1	X-ray Diffraction	47
2.2.2	Transmission Electron Microscopy	49
2.2.3	BET	50
2.2.4	Fourier Transform Infrared Spectroscopy	53
2.3	Sample Measurement and Data Analysis	54
2.3.1	Sievert's Apparatus	54
2.3.2	Hydrogen Compressibility and Ideal Gas Correction	57
	Bibliography	60
3	Hydrogen Desorption and Adsorption Measurements on Graphite	
	Nanofibers	62
3.1	History and Commercial Interests	62
3.2	Catalysts and Sample Preparation	63
3.3	Sample Morphology	63
3.4	Isotherm Measurement and Data Analysis	64
3.5	Results	67
3.6	Discussion	68
3.7	Conclusions	72
	Bibliography	76
4	Hydrogen Adsorption and Cohesive Energy of Single-Walled Carbon	
	Nanotubes	77
4.1	Background	77
4.2	Experiments	78

4.3	Isotherm Results and Cohesive Energy Calculation	79
4.4	Discussion	85
4.5	Conclusion	87
	Bibliography	88
5	Hydrogen Adsorption and Phase Transitions in Fullerites	91
5.1	Background	91
5.2	Experiments	92
5.3	X-Ray Diffraction Pattern and Phase Transformation of Fullerite . . .	96
5.4	Discussion	100
	Bibliography	103
6	Carbon Supported Catalysts	105
6.1	Ni Catalyst Particle Size Control and Calculation	105
6.1.1	Ni/Activated Carbon	107
6.1.2	Ni/Fullerite	108
6.2	Results and Analysis	109
6.2.1	Isotherm Measurement	109
6.2.2	Isotherm Results	110
6.2.3	Fourier Transform Infrared Spectrometry	112
6.3	Conclusion	113
	Bibliography	116
7	Conclusions and Outlook for Further Work	118
7.1	Conclusions	118
7.2	Further Work	120

List of Figures

1.1	Compressed hydrogen density (data are obtained from [1]).	7
1.2	PEM fuel cell (Ballard Inc.).	10
1.3	The crystal structure of graphite showing ABAB stacking.	16
1.4	Proposed model of the tangled structure of vitreous carbon [10].	17
1.5	(a) The icosahedral C_{60} molecule. (b) The rugby ball-shaped C_{70} molecule.	20
1.6	The fcc crystal structure of C_{60}	21
1.7	Classification of carbon nanotubes: (a) armchair, (b) zigzag, and (c) chiral nanotubes.	24
1.8	The unrolled honeycomb lattice of a nanotube (from [40]). When we connect sites O and A , and B and B' , a nanotube can be constructed. Here, $C_h = (4, 2)$	25
1.9	The IUPAC classification of adsorption isotherms.	32
2.1	The configuration in the 2" system with about 1 g/day production rate (from [8]).	42
2.2	Vacuum trap for filtration (from [10]).	44
2.3	Physical adsorption isotherms: Langmuir ($K=30$) and BET ($c=30$) isotherm.	51
2.4	Micromeritics ASAP 2010 BET surface analysis apparatus.	52
2.5	Schematic drawing of Sievert's apparatus.	55
2.6	Compressibility factor for hydrogen.	59
3.1	High magnification TEM shot of graphite nanofiber sample #2 showing herringbone structure.	65
3.2	Low magnification TEM shot of graphite nanofiber sample #5.	66
3.3	SEM micrograph of graphite nanofibers in sample #5.	66

3.4	High resolution image from end of graphite nanofiber showing herringbone morphology. Inset at lower left shows lattice planes from boxed region.	67
3.5	TEM micrograph of carbon nanotubes in GNF sample #5.	68
3.6	Raw data of desorption steps at room temperature.	69
3.7	Calculated Δx (room temperature) for saran carbon sample and the empty reactor.	69
3.8	Desorption isotherms for saran carbon at room temperature and liquid nitrogen temperature (77 K).	70
3.9	A set of runs of desorption isotherm for saran carbon sample at liquid nitrogen temperature.	71
3.10	A set of runs of desorption isotherm for GNF sample #4 at room temperature.	71
3.11	Desorption isotherms for GNF sample #5, #7, and #8 at room temperature.	74
3.12	Log-log plot of 77 and 300 K isotherm data showing amount of adsorbed hydrogen/carbon for GNF sample #5 and #8, as a function of pressure. When multiple runs were taken, error bars are shown, with only the top half of the error bars drawn for clarity. Traces from saran carbon are also shown for comparison.	75
4.1	A low resolution transmission electron micrograph of the SWNT materials, showing the rope structure.	78
4.2	High resolution transmission electron micrographs of the SWNT materials. (a) as-prepared, showing cross sections of tubes towards lower center, and (b) after sonication in dimethyl formamide.	80
4.3	X-ray diffraction pattern of single-walled materials (a) as-prepared and (b) after sonication in dimethyl formamide.	81
4.4	Chemical potential of hydrogen gas at 77 K.	82

4.5	Isotherms of composition versus pressure at 80 K for samples of as-prepared SWNT material, the SWNT material after sonication in dimethylformamide, and a high surface area saran carbon. Adjacent pairs of curves (labeled "SWNT") were sequential runs on the same sample. Also shown is the curve of the saran carbon scaled to lower H/C ratio by the surface area ratio of 285/1600.	83
5.1	Desorption isotherms of composition versus pressure at 77 K for two different batches of fullerite sample #1 of C ₆₀ -C ₇₀ fullerite materials. The upper set includes a trace for Saran carbon. The lower set shows identical isotherm behavior as a function of adsorption/desorption cycle number.	93
5.2	Transmission electron micrograph of fullerite #1, C ₆₀ /C ₇₀ . (a) low magnification bright field, and (b) higher magnification dark field of inset area showing recondensed fullerite nanocrystals.	96
5.3	Phase diagram showing the various phases of C ₇₀ , the possible phase transitions, and the stacking of the molecules [14].	97
5.4	X-ray diffraction pattern of (b) pure C ₆₀ (99.9+%) and (a) simulated with Crystallographica.	101
5.5	X-ray diffraction of all fullerene samples.	102
6.1	Dark field TEM images of Ni catalyst particles supported on the Darco activated carbon.	107
6.2	X-ray diffraction patterns of Ni/activated carbon samples.	108
6.3	X-ray diffraction patterns of Ni/fullerite samples. (a) fullerite from Ac-sea, (b) fullerite from MER, and (c) fullerite from MER with sonication used for catalyst preparation process.	109
6.4	Desorption isotherms of composition versus pressure at 77K for fullerite and Ni/fullerite samples.	110
6.5	Desorption isotherms of composition versus pressure at 300K and 450K respectively, for Ni/fullerite samples.	111

6.6	Adsorption isotherms of composition versus pressure at 300K and 450K respectively, for Darco activated carbon, Ni/DAC, fullerite and Ni/fullerite samples.	112
6.7	Fourier transform infrared spetrum of Darco activated carbon and Ni/DAC samples.	114
6.8	Fourier transform infrared spetrum of fullerite sample and Ni/fullerite samples.	115

List of Tables

1.1	General properties of hydrogen.	2
1.2	Physical properties of C ₆₀ molecules and crystals.	22
1.3	Physical properties of C ₇₀ molecules and crystals.	22
2.1	Selection of metals and metal compounds.	45
2.2	Absorbance wavenumbers of some functional groups and molecules.	54
3.1	Range of catalyst compositions and reactant gases used to produce graphite nanofibers.	64
3.2	Comparison of surface area as measured by BET, desorbed atomic ratio of H to carbon, and total H ₂ coverage assuming diameter of solid molecular H ₂ of 0.351 nm[11].	70
5.1	H ₂ storage capacities and BET surface areas of fullerenes.	94
6.1	Preparation and characterization of carbon supported Ni catalyst particles.	106
6.2	Hydrogen storage capacities of carbon samples with or without catalysts.	111
7.1	Summary of hydrogen storage capacities and surface areas of carbon samples.	118

Chapter 1 Introduction

1.1 Hydrogen

In this section, we shall discuss the properties of hydrogen, its economic and technological importance and its storage methods.

1.1.1 General Aspects

Hydrogen has been proposed as a clean fuel for the future, both in transportation and stationary power applications.

The future use of hydrogen to generate electricity, heat homes and businesses, and fuel vehicles will require the creation of a distribution infrastructure of gas and cost-effective transport and storage. Present storage methods are too expensive and will not meet the performance requirements of future applications.

Potential uses of hydrogen as a fuel and energy carrier include powering vehicles, running turbines or fuel cells to produce electricity, and cogenerating heat and electricity for buildings. Research in hydrogen utilization is focused on technologies that will most directly facilitate the progression to a hydrogen energy economy.

Transport technologies will need to be developed based on the production and storage systems that come into use as the hydrogen energy economy evolves.

General Properties of Hydrogen

Hydrogen is a colorless, tasteless, and odorless gas. It liquefies at atmospheric pressure at 20.27 K. Some of its physical properties are listed in Table 1.1 [1].

Quantity	Value
atomic weight	1.00794
melting point	-259.14°C (14 K)
boiling point	-252.88°C (20.27 K)
density at STP	0.0899 kg/m ³
density of liquid	70.78 kg/m ³
density of solid	70.6 kg/m ³
specific heat at constant pressure	14.5 J/g·K
latent heat of vaporization	445.5 J/g

Table 1.1: General properties of hydrogen.

Advantages and Disadvantages of Hydrogen as a Fuel

Advantages

Hydrogen can be produced from almost any energy source, including renewable energy sources and most of all the future primary energy sources. Hydrogen can be produced from electricity and can be converted into electricity at relatively high efficiencies.

When combusted with air the only products are water vapor and oxides of nitrogen (the NO_x can be controlled and suppressed by selection of combustion conditions). Thus hydrogen is environmentally compatible. Hydrogen can be combined with gasoline, ethanol, methanol, or natural gas. It is proposed to add hydrogen into gasoline to boost performance and reduce pollution. Adding just 5% hydrogen can the gasoline/air mixture in an internal combustion engine could reduce nitrogen oxide emissions by 30% to 40%.

Energy density based on per unit weight for hydrogen is larger than for any other practical fuel. Gasoline is 14 KHW/kg, while the hydrogen is 38 KHW/kg.

Hydrogen is an excellent general purpose fuel, probably better than any other practical fuel. This is partly because in air mixtures the range of flammability is very broad (4.1% to 74%) [2]. Spills of hydrogen dissipate rapidly under conditions of good ventilation and it is less toxic than other fuels.

Disadvantages

Hydrogen is gas at room temperature. Compact storage requires high pressures,

liquefaction, or chemical combination. The temperature of liquefaction is extremely low (20.3K or -253 C°) and the liquid has relatively low density (0.07) g/cm³. Liquefaction of hydrogen consumes energy. The heat of combustion per unit volume at STP is relatively small due to the low density of the gas.

Hydrogen is explosive. In air mixtures, the range of flammability is very broad (4% to 74%) and the maximum flame velocity is quite high. The ignition energy is very small and easily generated from a spark of static electricity. This could cause safety concern.

Hydrogen can be transported by pipelines similar to hose used to transport natural gas. However, hydrogen tends to leak more readily than most gases, and can embrittle some metals used for pipelines.

The major drawbacks to the use of hydrogen are its cost and the problems of storage. However, as hydrocarbon fuels become relatively more expensive as low-cost reserves diminish, and as the atmospheric CO₂ level rises, increasing the mean temperatures as predicted by the greenhouse effect, hydrogen will become increasingly more attractive as a universal energy carrier and fuel.

1.1.2 Production of Hydrogen

The choice of production methods will vary, depending on the quantity and desired purity of hydrogen. The future vision is that it will be cost-effectively produced from renewable energy sources.

Steam Reforming of Natural Gas

Hydrogen is now produced primarily by this method, which has been the most efficient, economical and practical technique available for several decades. It is a two-step process. The natural gas is exposed to high temperature steam to produce hydrogen, carbon monoxide, and carbon dioxide. Next the gas is further reformed with steam to convert carbon monoxide to produce additional hydrogen. The yield of hydrogen by this process is approximately 70% to 90% Hydrogen can be converted

from hydrocarbons ranging from methane to heavy naphtha using steam reforming method [3].

Electrolysis

For applications requiring extremely pure hydrogen, electrolysis is used to produce hydrogen. It is a relatively expensive process that uses electricity to dissociate water into hydrogen and oxygen gas. The efficiency of this process is about 67%. Renewable energy sources of electricity such as solar, wind, and hydropower can be used in electrolysis.

Photoelectrolysis

Photoelectrochemical (PEC) production uses semiconductor technology in a one-step process of splitting water directly upon sunlight illumination. A PEC system combines a photovoltaic cell material that produces electric current when exposed to light) and an electrolyzer in a single device. The process has shown excellent potential for producing low-cost renewable hydrogen.

Biomass Gasification and Pyrolysis

The production of hydrogen can result from high-temperature gasifying and low-temperature pyrolysis of biomass (feedstocks include wood chips and forest and agricultural residues). In pyrolysis, biomass is broken down into highly reactive vapors and a carbonaceous residue, or char. The vapors, when condensed into pyrolysis oils, can be steam reformed to produce hydrogen. A typical biomass feedstock produces about 65% oils and 8% char by weight, with the remainder consisting of water and gas. The char is burned to provide the required process heat for the pyrolysis reaction. For hydrogen production, a fast-pyrolysis reactor is directly linked to a steam reformer. Such processes have yields from 12% to 17% hydrogen by weight of dry biomass.

Photobiological Production

Most photobiological systems use the natural activity of bacteria and green algae to produce hydrogen. Chlorophyll absorbs sunlight and enzymes use the energy to dissociate hydrogen from water. Photobiological technology holds great promise for long-term sustainable hydrogen production. Employing catalysts and engineered systems, H₂ production efficiency could reach 24%.

1.1.3 Storage Methods

The potential uses of hydrogen as a fuel and energy carrier includes powering vehicles, running turbines or fuel cells to produce electricity, and cogenerating heat and electricity for buildings. Different applications will require different types of storage technologies. Utility electricity generation for buildings will have storage fixed in one location (stationary storage), thus the size and weight will be less important than energy efficiency and costs of the system. Powering a vehicle, however, will require hydrogen storage in an on-board system (mobile storage) with weight and size similar to the gasoline tank in today's vehicle.

Compressed Gas Storage Tanks

Hydrogen used today in industrial applications is generally in the form of compressed gas or cryogenic liquid, referred to as "physical storage." Due to its relative simplicity, rapid refueling capability, excellent dormancy characteristics, and low infrastructure impact, on-board high-pressure hydrogen storage provides a possibly best near-term solution for the commercialization of fuel-cell-powered motor vehicles [4]. Vehicle range, storage system weight, cost, durability, and compatibility of component materials are all key issues.

New materials, such as high-strength carbon fiber composite, have permitted storage tanks to be fabricated to hold hydrogen at extremely high pressures. Selected plastic liner materials with low hydrogen permeability and long-term durability give better tankage performance. Thiokol Propulsion is working with DOE on the devel-

opment of conformable tanks with a minimum burst pressure of up to 12,000 psi [5]. Safety and performance standards for high-pressure vehicle storage were applied to ensure safe operation over the tank being 15-20 year design life.

Liquid Hydrogen

Condensing hydrogen gas into the more dense liquid form enables a larger quantity of hydrogen to be stored and transported. The density of liquid hydrogen is 70.8 g/liter, which is three times higher than room temperature compressed hydrogen at 34.5 MPa (5,000psi), or equivalent to the density of compressed gas at 110.2 MPa (15,980 psi). Figure 1.1 shows the density for compressed hydrogen and liquid hydrogen. However, converting hydrogen gas to liquid hydrogen is costly and requires a large input of energy. The boil-off of liquid hydrogen is an issue that takes special consideration.

Metal Hydrides

Various pure or alloyed metals can combine with hydrogen, producing stable metal hydrides. Because of their high volumetric density, safety, and the ability to deliver pure hydrogen at a constant pressure, metal hydrides have a great potential for hydrogen storage. There are more than 80 metals in existence that form metal hydrides by absorbing and retaining hydrogen under certain temperature and pressure conditions. Hydrogen will be released by changing the condition, such as heating.

Due to their low gravimetric density, metal hydrides may be of limited use in vehicles. New metal alloys have been developed that offer better hydrogen storage characteristics than single metal hydrides. Hydrogen storage capacities of the alloys vary between 2.5 wt% and 6.2 wt% depending on the composition. Thin film alloys of magnesium-iron-aluminum-nickel-titanium have exhibited improved gravimetric and volumetric energy densities. Efforts are being made to scale up production of these alloys.

A new class of materials, known as nonclassical polyhydride metal complexes (PMCs), has also been developed. Classical PMCs are known to have relatively high

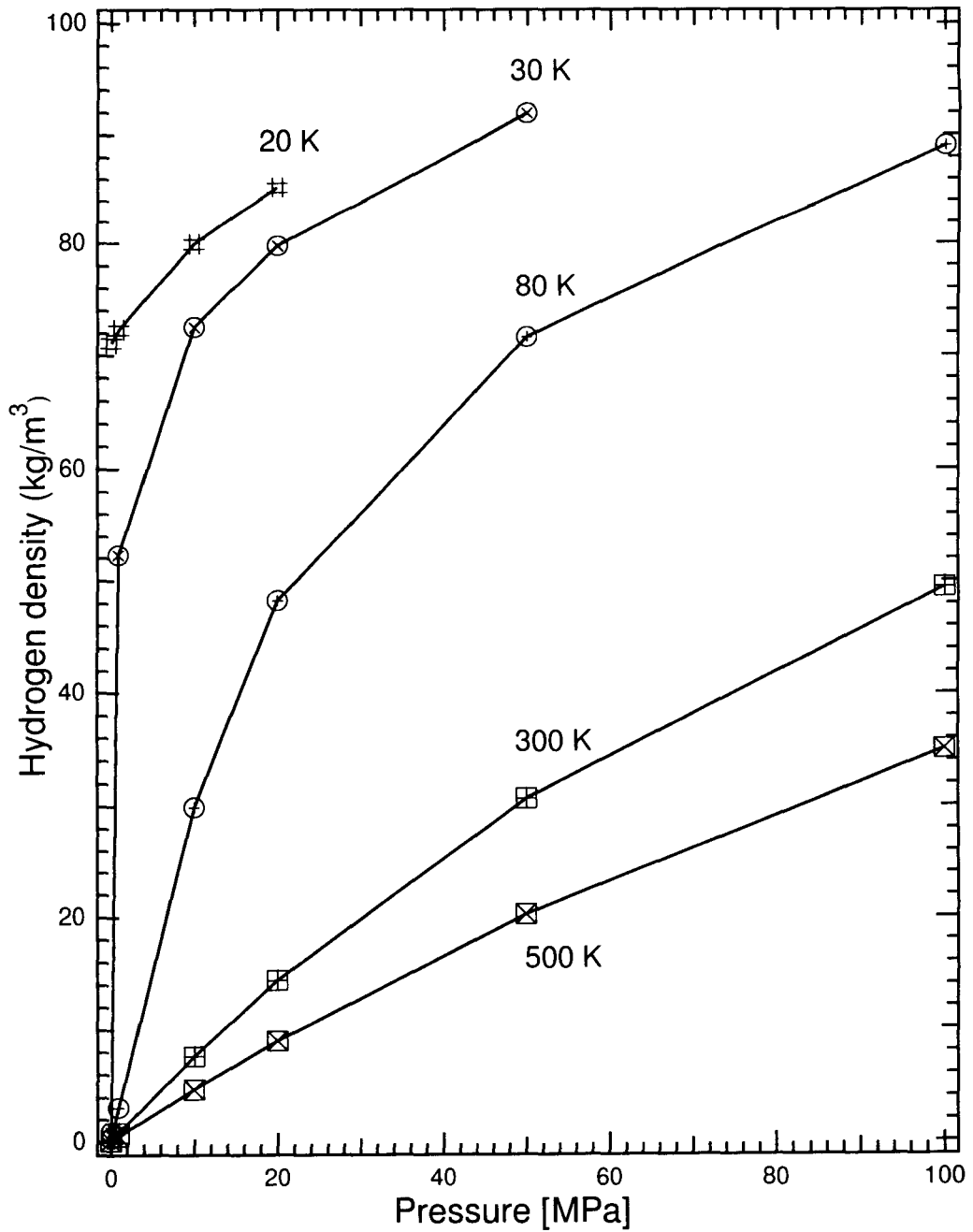


Figure 1.1: Compressed hydrogen density (data are obtained from [1]).

gravimetric densities, but they generally undergo irreversible dihydrogen elimination. In the nonclassical PMCs, hydrogen bonds to the metal while still retaining significant hydrogen-to-hydrogen bonding, allowing a complete release of hydrogen under mild conditions and without high vacuum. This unique activity illustrates the high potential of this type of PMC as a hydrogen storage material.

Gas-on-Solids Adsorption

The ability of high-surface-area carbons, when chemically activated, to retain hydrogen on their surfaces is well known. This process is called *adsorption* (1.4) and usually takes place with these materials at relatively high pressures and low temperatures.

Microspheres

Very small glass spheres, with diameters from 25 to 500 μm and wall thicknesses of approximately 1 μm , can hold hydrogen at high pressures. At temperatures of 200°C to 400°C, the increased permeability of the glass permits the spheres to be filled by hydrogen under pressure by immersion in high-pressure hydrogen gas. When cooled to ambient temperature, the glass is no longer permeable and the hydrogen is locked inside the spheres. Subsequent raising of the temperature will release the hydrogen. Research has determined that a small bed of such microspheres can contain hydrogen at about 62 MPa with a hydrogen mass fraction of 10% [6].

1.2 Fuel Cells

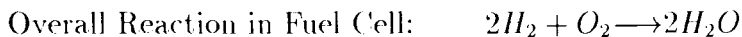
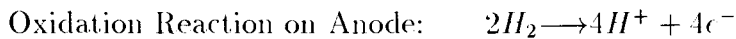
The fuel cell is a nineteenth-century invention. However, it took more than a hundred years until the National Aeronautics and Space Administration (NASA) demonstrated some of its potential applications as a power source for the space flights in early 1960s. Today, research on fuel cell is driven by technical, economic, and social forces such as high performance characteristics, reliability, durability, low cost, and environmental benefits.

1.2.1 Fuel Cell Principles

A fuel cell is an electrochemical device that continuously converts the chemical energy of a fuel directly into electrical energy. It is two to three times more efficient than an internal combustion engine. Water is the only emission when hydrogen is used as fuel.

A single cell consists of an electrolyte that is sandwiched between two porous gas diffusion electrodes, an anode and a cathode. As hydrogen flows into the fuel cell on the anode side, a platinum catalyst facilitates the separation of the hydrogen molecules into electrons and protons (hydrogen ions). The hydrogen ions migrate through the electrolyte membrane and again with the help of a platinum catalyst, combine with oxygen and electrons on the cathode side to form water. The electrons, which can not pass through the insulating membrane, flow from the anode to the cathode through an external circuit containing a motor or other electric load, which consumes the power generated by the cell. The voltage from one single cell is about 0.7 volts [7]. When the cells are combined into stacks, the operating voltage increases to the value of electrical power required.

The electrochemical reaction inside a fuel cell is:



1.2.2 Classification of Fuel Cells

There are several types of classifications of fuel cells, based on different criteria [7]: fuel used, operating temperature, electrolyte, direct and indirect systems, primary and regenerative systems, and the types of electrolytes.

Polymer Electrolyte Membrane Fuel Cell (PEMFC)

In the PEMFC, the polymer electrolyte membrane is a solid, organic polymer, usually poly-perfluorosulfonic acid. A typical membrane material, such as the most

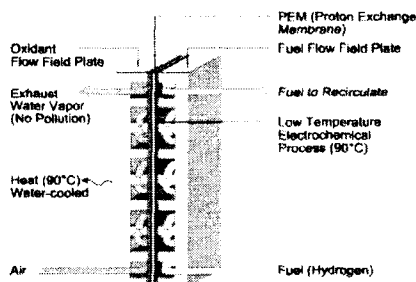


Figure 1.2: PEM fuel cell (Ballard Inc.).

prevalent membrane, Nafion produced by DuPont, consists of three regions:

1. the Teflon-like, fluorocarbon backbone, hundreds of repeating $-CF_2 - CF_2 - CF_2 - CF_2-$ units in length;
2. the side chains, $-O - CF_2 - CF_2 - O - CF_2 - CF_2-$, which connect the molecular backbone to the third region;
3. the ion clusters consisting of sulfonic acid ions, $SO_3^- H^+$.

The negative ions, SO_3^- , are permanently attached to the side chain and can not move. However, when the membrane becomes hydrated by absorbing water, the hydrogen ions become mobile. Ion movement occurs by protons, bonded to water molecules, hopping from SO_3^- site to SO_3^- site within the membrane. Because of this mechanism, the solid hydrated electrolyte is an excellent conductor for hydrogen ions, or protons. Thus PEM fuel cells are sometimes called proton exchange membrane fuel cells.

The operating temperature of the polymer electrolyte membrane fuel cells is limited by the range over which water is liquid since the presence of water is essential for the conductivity of electrolytes. The protons are carried from the anode to the cathode by means of hydronium (H_3O^+) ion within the membrane, which is the characteristic of *acid fuel cell*. Operating PEM fuel cells at temperatures exceeding $100^\circ C$ is possible under pressurized conditions, but shortens the life of the cell.

The only stable electrocatalysts in acidic electrolytes are platinum and its alloys. The best way to lower the Pt catalyst levels is to construct the catalyst layer with

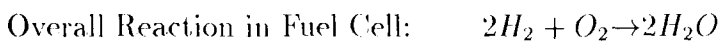
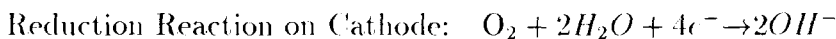
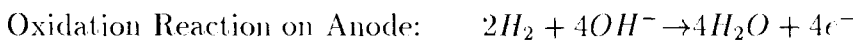
the highest possible surface area. Fine Pt particles are dispersed on high-surface-area carbon in the active layer of the electrode.

Impurities often present in the H_2 fuel, such as CO, may adsorb onto the surface of the Pt catalyst in the anode, preventing H_2 oxidation by blocking Pt catalyst sites. Thus the anode is very sensitive to CO poisoning. CO tolerance level for Pt-Ru catalyst is ~ 50 ppm.

Very thin membranes (10-100 μm) are used in the fuel cell to minimize ohmic resistance losses and hence attain high efficiencies and power densities.

Alkaline Fuel Cells (AFC)

Alkaline fuel cells are characterized by hydroxyl (OH^-) ions. The alkaline electrolyte is 35% potassium hydroxide (KOH), immobilized in a reconstituted asbestos matrix. The electrochemical reactions in AFC are:



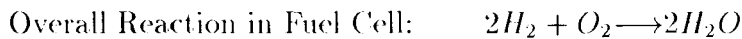
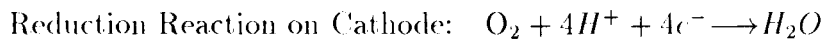
The operation temperature of AFC's is 60° . The advantages of AFC's are:

- reliability and high efficiency ($\geq 60\%$);
- cathode performance is much better than for acid fuel cells;
- materials of construction tend to be low in cost.

An attractive feature of AFC's is: unlike in acid fuel cells, a wide range of electrocatalysts can be used including nickel, silver, metal oxides, spinels, as well as noble metals. A major problem with AFC is that the CO_2 tolerance level is very low. CO_2 forms solid carbonate depositing in the porous gas diffusion electrode and carbonates the electrolyte, which can block flow channels, restrict reactant transport to the active site on the electrode, and reduce the ionic conductivity of the electrolyte.

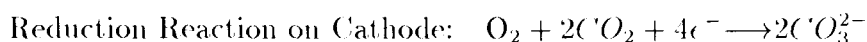
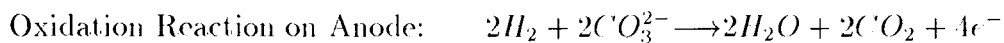
Phosphoric Acid Fuel Cells (PAFC)

The PAFC is the only type of fuel cell that has reached the commercialization stage in the twentieth century. Phosphoric acid (H_3PO_4) is an excellent electrolyte for fuel cells using hydrogen produced by steam-reforming/shift conversion of organic hydrocarbons and alcohols (methanol or ethanol). The electrochemical reactions in PAFC are:



Molten-Carbonate Fuel Cells (MCFC)

Molten carbonate fuel cells employ an alkali metal (Li, K, Na) carbonate as the electrolyte. Since these salts can function as electrolyte only when in the liquid phase, the cell operates at 600 to 700°C, which is above the melting points of the respective carbonates. In an MCFC, the cathodic reaction consumes oxygen and carbon dioxide to produce carbonate ions, which are transported through the electrolyte to the anode, where hydrogen reacts with the carbonate to produce water and carbon dioxide. The CO_2 is recycled back to the cathodic stream. The electrochemical reactions in MCFC are:



The advantages of MCFC include:

- due to the high operating temperature, noble metal electrocatalysts are not necessary;
- CO_2 is a fuel rather than a poison;
- the waste heat from the fuel cell is high enough for additional electric power generation in a bottoming-cycle steam or gas turbine and/or heat for chemical

processes resulting in high efficiency;

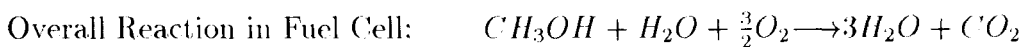
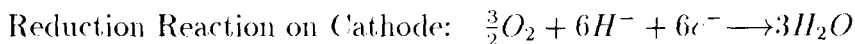
- it is possible to carry out the fuel-processing of natural gas in the fuel cell.

Solid Oxide Fuel Cells (SOFC)

Solid oxide fuel cell uses a solid, nonporous metal oxide as electrolyte. The operating temperature is 600 to 1000°C. Therefore, it also has *high temperature advantages*, which include higher efficiency, and the flexibility to use more types of fuels and inexpensive catalysts as the reactions involving breaking of carbon to carbon bonds in larger hydrocarbon fuels occur much faster as the temperature is increased. However, high temperature also enhances breakdown of cell components.

Direct Methanol Fuel Cells (DMFC)

Direct methanol fuel cell is similar to PEM fuel cell in that both use the same type of electrolyte - a poly-perfluorosulfonic acid proton exchange membrane. The main difference is DMFCs use liquid, such as 1 M methanol in water. At the anode, the methanol is oxidized to CO₂ and protons and electrons. The electrochemical reactions in DMFC are:



The technical and economical advantages of DMFC over the PEMFC are

- it eliminates the need for a fuel processor to produce hydrogen on-board, thus reduces the weight, volume, complexity and the cost of the system;
- methanol is a liquid with a high energy density and is considerably easier to carry on board the vehicle than hydrogen;
- by using about 1 M methanol directly in the fuel cell, the problems of water and thermal management are greatly minimized.

The challenges in developing DMFC's are:

- finding electrocatalysts to enhance the kinetics of electro-oxidation of methanol at the anode by ~ 3 orders of magnitude;
- minimizing crossover of methanol and hence the loss of faradic efficiency;
- reducing the performance degradation caused by poisoning of the electrocatalyst by adsorbed reaction intermediates, especially CO.

1.2.3 Fuel Choice for Fuel Cell Vehicles

Eight major automakers have set the timeframe to commercialize fuel cell vehicles to 2004 - 2005. Everyone faces the key issue of how to provide hydrogen to the fuel cells. The DOE Hydrogen Technical Advisory Panel gave an overview on this issue in May 1999 [8]. There are two fuel choice options: either produce the hydrogen on the ground and then store it onboard the vehicle (the direct hydrogen option); or produce the hydrogen on the vehicle by means of a mini onboard hydrogen plant (the onboard fuel processor option). Each option has multiple feedstock choices to produce the hydrogen. Onboard fuel processors can produce hydrogen from natural gas, methanol, ethanol, gasoline, or diesel stored onboard the vehicle. Ground-base hydrogen processors can also use hydrogen from all these feedstocks, or from the electrolysis of water with electricity from many potential renewable energy sources.

Considering the efficiency, technical difficulty, cost, and existing energy supply infrastructures, preferred feedstock choices for each fuel choice option have mostly narrowed to gasoline or methanol for fuel cell vehicles with onboard fuel processors, and natural gas for direct hydrogen. At this point, methanol appears to have an advantage over gasoline for onboard fuel processors due to better vehicle performance and less technical difficulty, despite more costly changes needed to make methanol widely available at fueling stations. For direct hydrogen vehicles, the hydrogen can be stored onboard either as a compressed gas at about 5,000 psi, or as a cryogenic liquid.

Each option has advantages and disadvantages associated with vehicle efficiency, technical difficulty, cost, fuel infrastructure requirements, safety, and long-term societal benefits. Performance, technical difficulty, and societal benefits favor direct hydrogen. Costs on a per vehicle basis are comparable for both options. But due to concerns over fuel infrastructure requirements and, to a lesser extent safety, industry is strongly favoring the onboard processing option.

1.3 Carbon Materials

Structural and chemical versatility together with a low atomic weight make carbon-based materials interesting and potentially useful as hydrogen storage media. The carbon atom has an atomic number of 6 and is in a $1s^2 2s^2 2p^2$ electronic ground state configuration. The atomic mass of carbon atom is 12.01115 amu. The atomic radius of carbon is 0.77 Å, which is measured as half the equilibrium distance between two carbon atoms of the planar graphite structure. Carbon has two major types of bonding, tetrahedral sp^3 bonding and trigonal sp^2 , in diamond and graphite, respectively. In the sp^2 hybridization state, one delocalized non-hybridized p electron is perpendicular to the plane of the other three hybrid sp^2 orbitals and becomes available to form the subsidiary π bond. The existence of π -*electron* bonding is responsible for carbon's versatile talents. Those materials having extended π -electron clouds are called π -*electron materials*, or sometimes as *supercarbon* [9], because of their fabulous multiformity and versatile properties. They include graphite, carbon nanotubes, fullerenes and various carbonaceous materials.

1.3.1 Graphite and Graphite Materials

Under ambient conditions and in bulk form, graphite is the stable phase of carbon. The crystal structure of graphite consists of series of stacked parallel layers with sp^2 bonding, as shown in Figure 1.3. Within each layer plane known as a *graphene plane*, the nearest-neighbor distance is 1.421 Å. The interplanar distance is relatively large, which is 3.35 Å. This gives an in-plane lattice constant a of 2.462 Å and a c -axis

lattice constant c of 6.708 Å. The structure is consistent with the $D_{6h}^1(P6_3/mmc)$ space group [11].

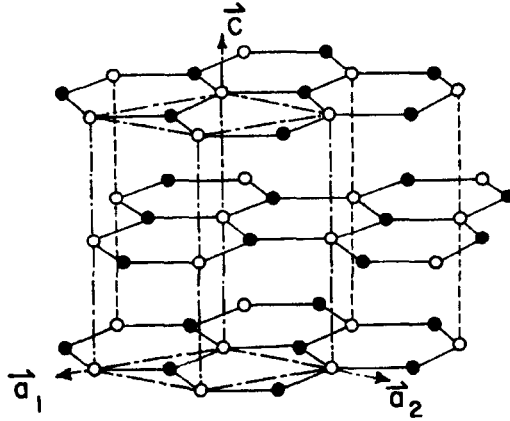


Figure 1.3: The crystal structure of graphite showing ABAB stacking.

Since the in-plane C-C bonding is very strong compared to the weak interplanar bonding, impurity species tend to occupy interstitial position *between the layer planes*. The weak interplanar bonding also allows entire planes of dopant atoms or molecules to be intercalated between the carbon layers, forming graphite intercalation compounds (GICs) [12].

Faults in the ABAB stacking give rise to a small increase in the interlayer distance. This continues until an inter-layer spacing of about 3.440 Å is reached, where the stacking of the individual carbon layers becomes uncorrelated. This structure with no three-dimensional order is called *turbostatic graphite*.

Other than natural single-crystal graphite flakes, there are many synthetic graphite materials, such as pyrolytic graphite, carbon fibers, vitreous carbon, and carbon black, which are actually aggregates of graphite crystallites, or polycrystalline graphites.

Generally, graphite is black, opaque, and metallic in luster. It has a density of 2.09 to 2.2 g/cm^3 .

Graphite Whisker is a graphitic material formed by rolling a graphene sheet into a scroll. Graphite whiskers are formed in a dc discharge between carbon electrodes using 75-80 V and 70-76 A [10]. The whiskers are to be found up to 3 cm long

and 1-5 μm in diameter. The growth of graphite whiskers has many similarities to the growth of carbon nanotubes.

Vitreous carbon or glassy carbon, is a common carbon material processed by slow, controlled degradation of certain organic precursor at temperatures typically from 600°C to 1000°C [13]. The selections of precursors includes polyfurfuryl alcohol, phenolics, polyimide, polyacrylonitrile, cellulose, and polyvinylidene chloride (PVDC), etc [10]. The microstructure of vitreous carbon consists of an extensive and tangled network of graphite-like ribbons or microfibrils (as shown in Figure 1.4), about 100 Å long and 30 Å in cross section, and resembles the precursor's chain configuration.

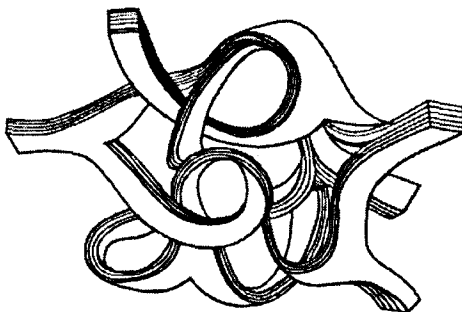


Figure 1.4: Proposed model of the tangled structure of vitreous carbon [10].

Saran carbon falls into this category. It is the name applied to carbonaceous products derived from the pyrolysis of PVDC or Saran resins. The structure of this material is an assembly of randomly oriented graphite microcrystals in an amorphous carbon matrix. It contains very small pores, which give them molecular sieve properties. Both porosity and pore size can be selected to some extent by varying the techniques used to make the material. There are two basic techniques described in the literature for carbonizing PVDC thermally [14]. One is a slow solid-state degradation which gives more control over the surface areas and the pore size of the resultant carbon. It produces carbon with a micropore structure and superior adsorptive properties. The other method involves heating at a fairly high rate such that the PVDC melts before any

significant degradation occurs. In the rapid heating method, the melt foams during the dehydrochlorination step, crosslinks and hardens yielding a carbon rich in macropores.

Pyrolytic Graphite or *highly oriented pyrolytic graphite* (HOPG) is the most commonly used high-quality graphitic material. It is prepared by the pyrolysis of hydrocarbons at temperatures above 2000° and subsequently heat treated to higher temperature [15]. When columnar or laminar pyrolytic graphites are annealed above 2700°C , usually under a pressure of several atmospheres, further ordering and stress relieving of the structure occur within each plane and between planes [10].

Carbon Fibers consist of a stack of turbostratic layers with little graphitic character and may in some cases include sp^3 bonds. Examples are polyacrylonitrile (PAN) and Rayon. The process involves several steps: stabilization, carbonization and high temperature heat treatment. Activated carbon fibers are highly porous carbon fibers with specific surface areas of 700 to 3000 m^2/g and pore volumes of 0.35 to 0.80 cm^3/g or more [16]. Fiber diameters are typically 10 μm , while the structure consists almost entirely of micropores with half widths on the order of 1 nm.

Carbon Black represents many types of finely-divided carbon particles that are produced by hydrocarbon dehydrogenation. The microcrystalline structures of the carbon blacks are found to be small graphite-like layers. In each individual particle, these graphene layers are concentric organized.

Porous Carbons are a number of carbon materials with very high surface areas and pores of nanometer dimensions similar to the dimensions of fullerenes, including activated carbons, exfoliated graphite, and carbon aerogels. Exfoliated graphite is prepared by heating a graphite intercalation compound above some critical temperature, thus a gigantic irreversible c -axis expansion occurs, with sample elongations of as much as a factor of 300 [17]. This elongation is called

exfoliation, which gives rise to spongy, foamy, low density, high surface area material. Carbon aerogels are a disordered form of sp^2 -bonded carbon with an especially low bulk density and are made by a supercooling process. They consist of interconnected carbon particles with diameters typically near 12 nm.

1.3.2 Activated Carbon

Due to their porous structure, activated carbon has been used in purification and gas adsorption for centuries. Active carbons have been commercially produced from a tremendous variety of carbonaceous starting materials, including coconut shells, peach pits, sawdust wood char, fish, lignin, petroleum coke, bone char, anthracite coal, coffee grounds, molasses, rice hulls, carbon black, peat, kelp, and sugar [18]. After carbonizing the source material under appropriate conditions, the resulting char is often subjected to oxidation in a controlled environment. Carbonization is usually conducted in the absence of air at temperature of 600°C to 900°C. In activation by oxidation, the oxidant selectively erodes the surface so as to increase the surface area, develop greater porosity, and leave the remaining atoms arranged in configurations that have specific affinities [19]. These characteristics contribute to the remarkable adsorption properties of activated carbons. Activated carbons have surface areas that range from 400 to over 2000 m²/g.

1.3.3 Fullerenes

Fullerenes were first discovered in 1985 by Kroto and Smalley [20] by time-of-flight mass spectroscopy in the hot carbon plasma generated during laser ablation of graphite. Fullerenes are a major extension of the scope of carbon molecules known to exist, and open an entirely new chapter on the physics and chemistry of carbon. The announcement by Krätschmer and Huffman [21, 22] in 1990 of a synthesis method capable of producing gram quantities of fullerenes makes it possible for hundreds of researchers to study these fascinating new materials.

Structures of Fullerenes

In C_{60} , the sixty carbon atoms are located at the vertices of a truncated icosahedron where all carbon sites are equivalent. This is consistent with the observation of a single sharp line in the nuclear magnetic resonance (NMR) spectrum [23]. As defined by IUPAC, fullerenes are polyhedral closed cages made up entirely of n three-coordinate carbon atoms and containing only hexagonal and pentagonal faces. There must be exactly 12 pentagonal faces and an arbitrary number h of hexagonal faces, which follows Euler's theorem for polyhedra

$$f + v = e + 2 \quad (1.1)$$

where f , v , and e are the numbers of faces, vertices, and edges of the polyhedra, respectively.

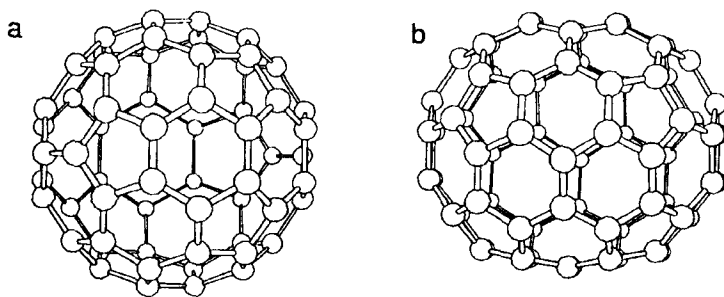


Figure 1.5: (a) The icosahedral C_{60} molecule. (b) The rugby ball-shaped C_{70} molecule.

The smallest possible fullerene is C_{20} with 12 pentagonal faces and no hexagonal faces. However, it is thermodynamically unstable since it is energetically unfavorable for two pentagons to be adjacent to each other, owing to high local curvature of the fullerene ball, and hence more strain energy. The resulting tendency for pentagons not to be adjacent to one another is called the isolated pentagon rule [24, 25]. The smallest fullerene to satisfy the isolated pentagon rule is C_{60} , as shown in Figure 1.5 (a). The next possible molecules are C_{70} with a rugby ball shape, as shown in Figure 1.5 (b). Since the addition of a single hexagon adds two carbon atoms, all fullerenes must have an even number of carbon atoms.

The structure of C_{70} can be envisioned as adding a ring of 10 carbon atoms to the C_{60} molecule. In contrast to C_{60} , which has only one unique carbon site and two unique bond lengths, the C_{70} molecule has five inequivalent sites and eight distinct bond lengths.

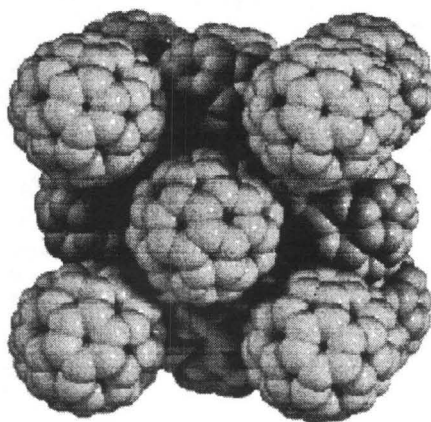


Figure 1.6: The fcc crystal structure of C_{60} .

In the solid state, the C_{60} structure is face-centered-cubic (fcc), as shown in Figure 1.6, with a lattice constant of 14.17 Å. The crystal structure of C_{70} is much more complex than that of C_{60} . The general agreement is that there are three regimes where the structure is isotropic above transition temperature T_{01} and becomes more anisotropic as T is decreased. This will be discussed in detail in Chapter 5.

Some physical properties of C_{60} and C_{70} molecules and crystals are summarized in Table 1.2 and 1.3.

Synthesis, Extraction, and Purification of Fullerenes

In 1990, Krätschmer et al. discovered a method to synthesize fullerenes in macroscopic quantities. There are many more processes which have been reported, including:

Quantity	Value	Reference
average C-C distance	1.44 Å	[26]
C-C bond length on a pentagon	1.46 Å	[27]
C ₆₀ mean ball diameter	7.1 Å	[28]
C ₆₀ ball outer diameter	10.34 Å	-
binding energy per atom	7.4 eV	[29]
heat of formation (per g C atom)	10.16 kcal	[30]
cohesive energy per C atom	1.4 eV/atom	[31]
fcc lattice constant	14.17 Å	[32]
C ₆₀ -C ₆₀ distance	10.02 Å	[33]
C ₆₀ -C ₆₀ cohesive energy	1.6 eV/molecule	[34]
tetrahedral interstitial site radius	1.12 Å	[33]
octahedral interstitial site radius	2.07 Å	[33]
mass density	1.72	[33]
transition temp	261 K	[35]
melting temperature	1180°C	[36]
sublimation temperature	434°C	[37]
heat of sublimation	40.1 Kcal/mol	[37]

Table 1.2: Physical properties of C₆₀ molecules and crystals.

Quantity	Value	Reference
average C-C distance	1.43 Å	[26]
C ₇₀ c-axis diameter	7.96 Å	[28]
C ₇₀ <i>a</i> – <i>b</i> axis diameter	7.12 Å	-
number of distinct C sites	5	[29]
number of distinct C sites	8	[29]
heat of formation (per g C atom)	9.65 kcal	[30]
fcc lattice constant	15.01 Å	[32]
C ₇₀ -C ₇₀ distance	10.61 Å	[33]
hcp lattice constant	a=b=10.56Å, c=17.18Å	[32, 33]
C ₇₀ -C ₇₀ cohesive energy	1.6 eV/molecule	[34]
Transition temperature T ₀₁ , T ₀₂	361 K, 282 K	[35]
sublimation temperature	466°C	[37]
heat of sublimation	43.0 Kcal/mol	[37]

Table 1.3: Physical properties of C₇₀ molecules and crystals.

- ac or dc plasma discharge between carbon electrodes in He gas
- inductive heating of carbon rods in vacuum
- laser ablation of carbon electrodes in He gas
- sputtering or electron beam evaporation of graphite in an inert atmosphere
- oxidative combustion of benzene/argon gas mixtures

Among these methods, the carbon arcing process and the flame process are the only processes which have been commercialized due to simplicity, low start up investment, relatively low operational complexity and readily available raw materials.

In the process of producing fullerenes, most methods simultaneously generate a mixture of stable fullerenes (C_{60} , C_{70} , ...), impurity molecules such as polycyclic aromatic hydrocarbons, and carbon-rich soot. Therefore, the synthesis of fullerenes must be followed by procedures to extract and separate fullerenes from impurities according to mass.

The Krätschmer-Huffman method is the most efficient way to produce large quantities of fullerenes and is thus widely in use. The process is quite straightforward. Graphite rods are evaporated by AC or DC arcing in a quenching atmosphere of inert gas (typically 100-200 torr of helium). The vaporized carbon condenses and deposits on the reactor walls as a light, fluffy condensate, or *soot*. A substantial fraction of this material is composed of fullerenes. The fullerene soot is then collected and the fullerenes are extracted, either by sublimation from the soot via heating in a vacuum or in an inert gas, or more commonly by solvent extraction. Several parameters are known to affect the conversion of the electrodes to fullerenes. High-purity helium is usually used instead of other inert gas such as argon and nitrogen. Most soot-generating chambers use a quenching gas pressure in the 100-200 torr range. It is reported the optimum pressure is highly sensitive to design specifications.

Two distinct methods are employed to extract the fullerenes from the soot produced. The solvent method uses toluene to dissolve the fullerenes, while the soot and

other insolubles are easily separated from the solution by filtration. Soxhlet extraction technique combined with chromatographic methods produces fullerenes of high purity. In the sublimation method, the raw soot is heated in a quartz tube in He gas, or in vacuum, to sublime the fullerenes, which then condense in a cooler section of the tube. The sublimation temperatures of crystalline C_{60} and C_{70} are relatively low ($T_{s,C_{60}} = 350^{\circ}C$, $T_{s,C_{70}} = 460^{\circ}C$).

1.3.4 Nanotubes

Discovered by Iijima of the NEC Laboratories in Japan in 1991 [38], carbon nanotubes are usually considered as tubular fullerenes. Carbon nanotubes were first synthesized as a by-product in arc-discharge method in synthesis of fullerenes. Currently, many different methods have been developed to prepare nanotubes, including arc-discharge, laser ablation and catalytic decomposition of hydrocarbon. Carbon nanotubes can be classified into two types: Multi-Walled Carbon Nanotubes (MWNT) and Single-Walled Nanotubes (SWNTs). The MWNT is composed of 2 to 30 concentric graphitic layers, diameters ranging from 10 to 50 nm and length of more than $10 \mu m$. SWNT is much thinner with the diameters from 1.0 to 1.8 nm.

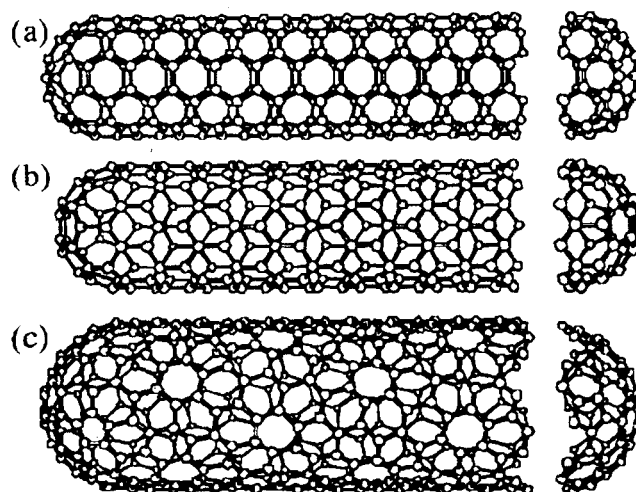


Figure 1.7: Classification of carbon nanotubes: (a) armchair, (b) zigzag, and (c) chiral nanotubes.

Structures of Nanotubes

The important and essential fact about the structure of a carbon nanotube is the orientation of the carbon hexagonal ring in the honeycomb lattice relative to the axis of the nanotube. Three examples of single-walled carbon nanotubes (SWNT) are shown in Figure 1.7. The ‘zig-zag’ and ‘armchair’ nanotubes are two possible high symmetry structures for nanotubes. The armchair tubules are obtained by bisecting a C_{60} molecule at the equator normal to a fivefold axis, and joining the two resulting hemispheres with a cylindric tube one monolayer thick, as shown in Figure 1.7 (a). If the C_{60} molecule is bisected normal to a threefold axis, the zigzag tubule shown in Figure 1.7 (a) is formed. However, it is believed that most nanotubes do not have these highly symmetric forms but have structures in which the hexagons are arranged helically around the the tube axis, as in Figure 1.7 (c). These structures are generally know as chiral, since they can exist in two mirror-related forms.

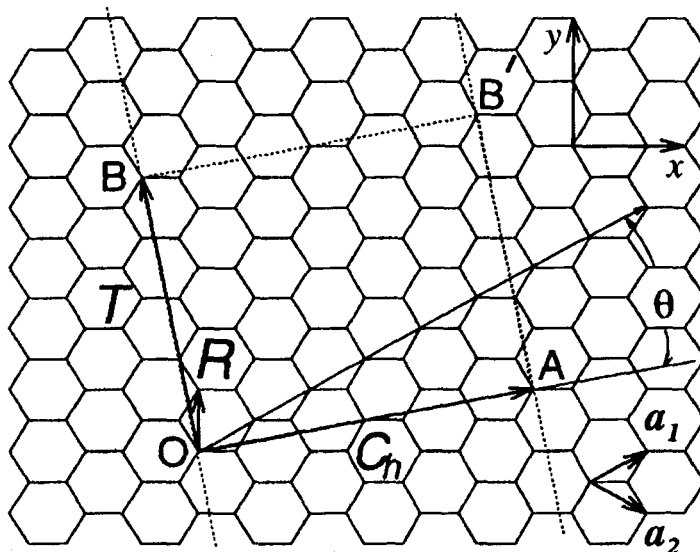


Figure 1.8: The unrolled honeycomb lattice of a nanotube (from [40]). When we connect sites O and A , and B and B' , a nanotube can be constructed. Here, $C_n = (4, 2)$.

An indexing method was developed by Hamada et al. [41]. The nanotube cylinder is produced by rolling up a sheet of graphene lattice. The structure of an individual

nanotube is specified by the vector \mathbf{C}_h , joining two equivalent points on the original graphene lattice. \mathbf{C}_h is called chiral vector, and can be expressed as

$$\mathbf{C}_h = n\mathbf{a}_1 + m\mathbf{a}_2 \equiv (n, m) \quad (1.2)$$

n, m are integers, $0 \leq |m| \leq n$.

An armchair nanotube corresponds to the case of $n = m$, and a zigzag nanotube corresponds to the case of $m = 0$. All other (n, m) chiral vectors correspond to chiral nanotubes. Because of the hexagonal symmetry of the honeycomb lattice, we need to consider only $0 \leq |m| \leq n$.

The diameter of the carbon nanotube, d_t , is given by $|\mathbf{C}_h|/\pi$, as

$$d_t = |\mathbf{C}_h|/\pi = \sqrt{3}a_{C-C} \sqrt{m^2 + mn + n^2}/\pi \quad (1.3)$$

The chiral angle θ is defined as the angle between the vectors \mathbf{C}_h and \mathbf{a}_1 , as shown in Figure 1.8. Due to the hexagonal symmetry of the honeycomb lattice, the values of θ is in the range $0 \leq |\theta| \leq 30$. θ is given by

$$\cos \theta = \frac{2n + m}{2\sqrt{n^2 + m^2 + nm}} \quad (1.4)$$

Synthesis of Nanotubes

There are currently four main methods used to synthesize carbon nanotubes: carbon arc synthesis, chemical vapor deposition, ion bombardment, and laser vaporisation. Among these, the most successful has been the laser vaporisation method for the synthesis of single-walled nanotubes which was introduced by Smalley's group in 1996 [42].

Production of multi-walled nanotubes (MWNT)

The original method used by Iijima to prepare nanotubes differed slightly from the Krätschmer-Huffman technique for C_{60} production in that the graphite electrodes

were held a short distance apart during arcing, rather than being kept in contact. In this electric arc discharge method, the quantity of MWNT obtained depends on the pressure of He atmosphere in the reactor, which is the most important parameter. The highest quantity of MWNTs is obtained when the pressure of He is around 500 torr, while the best condition for fullerene production is about 100 torr[43]. The MWNTs produced by laser ablation are much shorter than those by arc-discharge method [45]. Catalytic decomposition of hydrocarbon is suitable for mass production of MWNTs because the MWNTs synthesized by this method do not contain nanoparticle or amorphous carbon [43].

Production of single-walled nanotubes (SWNT)

Whereas multi-walled nanotubes require no catalyst for their growth, catalysts are necessary for the growth of the single-walled nanotubes (SWNTs), and more than one catalytic species seem to be necessary to grow ropes of SWNTs.

In the early reports of the laser synthesis technique, high yields with about 70%-90% conversion of graphite to SWNT were reported in the condensing vapor of the heated flow tube, operating at 1200°C. A Co-Ni/graphite composite laser vaporisation target was used, consisting of 1.2 atom% Co-Ni alloy with equal amounts of Co and Ni added to the graphite (98.8 atom%)[42]. Two sequenced laser pulses were used to evaporate a target containing carbon mixed with a small amount of transition metal from the target. Flowing argon gas sweeps the entrained nanotubes from the high temperature zone to the water-cooled Cu collector downstream, just outside the furnace.

The material thus produced appears in a scanning electron microscope image as a mat of “ropes” 10-20 nm in diameter, and up to 100 μm or more in length. By transmission electron microscopy (TEM), each rope is found to consist primarily of a bundle of SWNT aligned along a common axis. The diameters of the SWNTs have a strongly peaked distribution at 1.38 ± 0.02 nm, very close to the diameter of an ideal (10,10) nanotube. The SWNTs are held together by weak van der Waals inter-nanotube bonds to form a two-dimensional triangular lattice with a lattice constant

of 1.7 nm, and an inter-tube separation of 0.315 nm at closest approach within a rope. By varying the growth temperature, the catalyst composition and other growth parameters, the average nanotube diameter and diameter distribution can be varied [44].

Other methods of nanotube synthesis include carbon arc electrode, vapor growth, and carbon ion bombardment.

Purification of nanotubes

In most synthesis procedures, carbon nanotubes are produced along with other materials, such as amorphous carbon and carbon nanoparticles. Therefore, purification is necessary to isolate the carbon nanotubes from other entities. Three basic methods have been used: gas phase, liquid phase, and intercalation methods.

1.3.5 Graphite Nanofibers

Carbon nanofibers (also known as carbon filaments) can be grown from the catalytic decomposition of certain hydrocarbons over small metal particles, such as iron, cobalt, nickel, and some of their alloys. The diameter of the nanostructure is controlled by the size of the catalyst particle and can vary between 2 and 100 nm, and lengths ranging from 5 to 100 μm .

A model of the mechanism of carbon nanofiber formation has been proposed by Baker and coworkers using controlled atmosphere electron microscopy [46]. In their proposed mechanism, the key steps are the adsorption and decomposition of a hydrocarbon on a metal surface to produce carbon species which dissolve and diffuse through the bulk and ultimately precipitate at the rear of the particle to form the nanofiber. As a result of this process the catalyst particle is detached from its original support and remains at the growing end of the carbon structure.

It has been suggested that there is subtle relationship between the crystalline quality of the graphene layers in the deposited carbon nanofibers and the ability of the metal catalyst particle to undergo a strong interaction with graphite in the presence of hydrogen. It is observed that cobalt forms highly graphitic carbon nanostructures,

whereas other metals in the same group, iron and nickel, exhibit a somewhat weaker interaction with graphite and produce nanofiber structures with a large fraction of amorphous carbon. On the other hand, when either copper or iron is mixed with nickel, there is a significant increase in the wetting characteristics with respect to graphite and such catalyst particles tend to generate highly ordered carbon nanostructures. Therefore, it is possible to control the morphology of the nanofibers by merely altering the ratio of the alloy constituents. Particles rich in nickel were found to produce much better crystallinity in the filament structures than those grown from either pure nickel or copper-rich particles [46].

In general, the structure of nanofibers consist of an inner core of amorphous carbon surrounded by a skin of graphitic platelets. It is also found that the internal structural arrangement can be significantly different from that described above, and is extremely sensitive to a number of factors, particularly the chemical nature of the catalyst and the composition of the gaseous reactant.

1.4 Physisorption and Chemisorption

Gas adsorption¹ on solid surfaces and in pore spaces is a complex phenomenon involving mass and energy interaction and phase changes. In general, two types of adsorption are distinguished, physical adsorption (abbreviated as *physisorption*) and chemical adsorption (abbreviated as *chemisorption*).

Adsorption at a surface or interface is largely the result of binding forces between the individual atoms, ions, or molecules of an adsorbate and the surface, all of these forces having their origin in electromagnetic interactions.

In physisorption, there is a van der Waals interaction (sometimes considered as an

¹The term *adsorption* was introduced by Kayser [47] in 1881 to connote the condensation of gases on free surfaces, in contradiction to gaseous *absorption* where the molecules of gas penetrate into the mass of the absorbing solid. Adsorption (strictly, physisorption) has now been internationally defined as the enrichment of one or more components in an interfacial layer. Another term *sorption*, which was proposed by McBain [48] in 1909 to embrace *adsorption* on the surface, *absorption* by penetration into the lattice of the solid, and capillary condensation within the pores, has never enjoyed really wide usage. Thus the designation *adsorption* is frequently employed to denote uptake whether by capillary condensation or by surface adsorption.

induced dipole-dipole interaction) between the adsorbate and the substrate. Van der Waals interactions are weak, and are responsible for the energy release when a particle is physisorbed. Such small amounts of energy can be transferred into vibrations of the lattice and dissipated by thermal transport, and a molecule bouncing across the surface will gradually lose its energy and finally adsorb to it in the process called accommodation. The enthalpy of physisorption can be measured by monitoring the rise in temperature of a sample of known heat capacity, and typical values are in the range of 20 kJ/mol or less [51]. This small enthalpy change is insufficient to cause bond breaking, so a physisorbed molecule retains its identity, although it might be distorted by the presence of the surface. In chemisorption, the particles stick to the surface by forming a chemical (usually covalent) bond, and tend to find sites that maximize their coordination number with the substrate. The enthalpy of chemisorption is very much greater than that for physisorption, and typical values are in the region of 200 kJ/mol [51]. A chemisorbed molecule may be torn apart at the demand of the unsatisfied valences of the surface atoms.

The free gas and the adsorbed gas are in dynamic equilibrium. The fractional coverage of the surface, θ , increases with decreasing temperature and increasing pressure. The variation of θ with pressure at a chosen temperature is called the *adsorption isotherm* (or desorption isotherm). This is a measure of the molar quantity of gas n taken up, or released, at a constant temperature T by an initially clean solid surface as a function of gas pressure P ,

$$n = f(P) \tag{1.5}$$

If the temperature is below the critical temperature of the gas, it is conventionally expressed as

$$n = f(P/P^\circ) = f(P_{rel}) \tag{1.6}$$

where P° is the saturation vapor pressure of the adsorptive². P/P° is called relative pressure, P_{rel} , ranging from 0 to 1.

Adsorption isotherms generally follow one of six forms as shown in Figure 1.9. It is based on an earlier classification by Brunauer, Deming, Deming and Teller [52] (BDDT), while the sixth is a recent addition.

Type I is characteristic of adsorption on microporous adsorbents (solid with pores less than 20 Å).

Type II describes adsorption on nonporous solids or adsorbents with macropores (pores with width larger than 500 Å).

Type III and V isotherms are characteristic of weak gas-solid interactions [53]. The Type III is given by a nonporous or macroporous solid and the Type V isotherm by a mesoporous solid.

Type IV represents the adsorption isotherm on adsorbents with mesopores (pores with width between 20 Å and 500 Å).

Type VI, which was not included in the Brunauer classification, illustrates the relatively rare adsorption isotherms with multiple steps.

1.4.1 Langmuir Isotherm

This simplest isotherm model is based on three assumptions [54]:

1. Gases form only one molecular layer on a solid.
2. The surface of a solid is composed of a two-dimensional array of energetically homogeneous sites.
3. There is no interaction among the adsorbent molecules, either through repulsive or attractive forces.

²General terminology

Adsorbent the solid material

Adsorbate the material actually adsorbed by the solid

Adsorptive the general term for the material in the gas phase which is capable of being adsorbed.

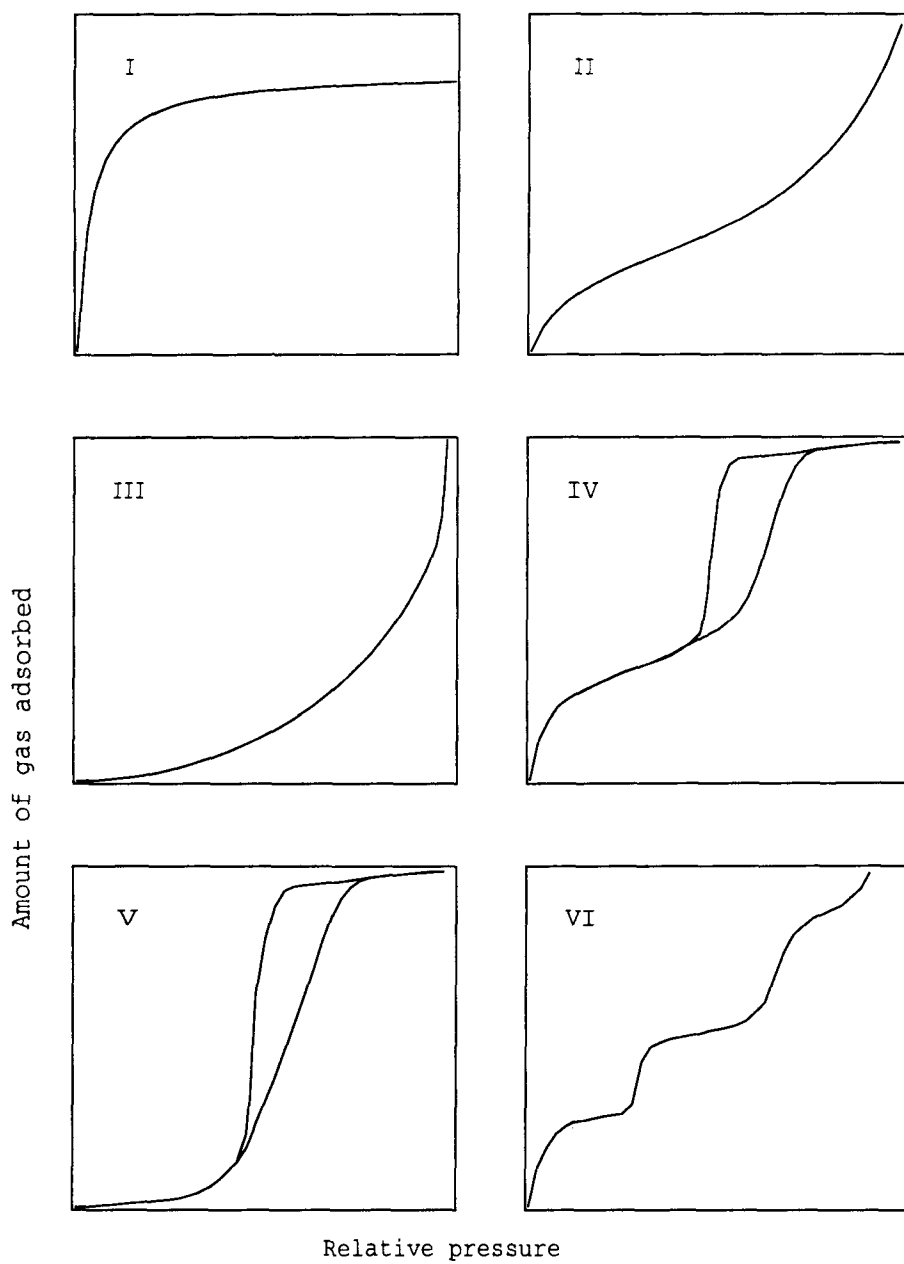


Figure 1.9: The IUPAC classification of adsorption isotherms.

The Langmuir isotherm can be derived by considering the kinetics of condensation and evaporation of gas molecules at a unit solid surface. If θ represents the fraction of the adsorbent surface covered by a monolayer of adsorbate, the rate of condensation of gas molecules onto the surface is proportional to the fraction of vacant sites $(1 - \theta)$, and the absolute pressure of the gas, P , with rate constant k_a :

$$\frac{d\theta}{dt} = k_a P(1 - \theta)$$

The rate of evaporation from the surface is proportional to θ , with rate constants k_d :

$$\frac{d\theta}{dt} = -k_d \theta$$

The enthalpy of the adsorbed molecule is lower by ΔH than the desorbed molecule, so the desorption rate is given as

$$k_d = k_a \exp\left(-\frac{\Delta H}{kT}\right)$$

At equilibrium, the net rate of adsorption is zero, and solving for θ gives the Langmuir isotherm:

$$\theta = \frac{KP}{1 + KP} \quad (1.7)$$

where $K = k_a/k_d$.

Equation 1.7 can be rearranged to the linear form

$$KP\theta + \theta = KP$$

With $\theta = V/V_\infty$, where V is the volume of gas adsorbed at pressure P , and V_∞ is the volume corresponding to complete coverage, we have

$$\frac{P}{V} = \frac{P}{V_\infty} + \frac{1}{KV_\infty} \quad (1.8)$$

Thus, if the equation applies and values of P/V are plotted against P , a straight line should result, with the slope $1/V_\infty$ and intercept $1/KV_\infty$.

1.4.2 BET Isotherm

Brunauer, Emmett, and Teller [56] extended the Langmuir model to include multi-layer adsorption phenomena. The essential assumptions of the BET model are that the forces active in the condensation of gases also are responsible for the binding energy in multi-molecular adsorption, and any given layer need not be complete before subsequent layers can form. By equating the rate of condensation of gas molecules onto an already adsorbed layer to the rate of evaporation from that layer and summing for an infinite number of layers, they obtained the expression

$$\frac{a}{a_{mon}} = \frac{cP_r}{(1 - P_r)[1 - (1 - c)P_r]} \quad (1.9)$$

where $P_r = P/P^\circ$, P° is the saturation pressure of the gas, a_{mon} is the number of moles of gas adsorbed corresponding to monolayer coverage, a is the amount of gas adsorbed at pressure P , and c is a constant which is large when the enthalpy of desorption from a monolayer is large compared to the enthalpy of vaporisation of the liquid adsorbate:

$$c \propto \exp\left(\frac{\Delta H_{des} - \Delta H_{vap}}{RT}\right)$$

where ΔH_{des} is the enthalpy of desorption from the first layer, and ΔH_{vap} is the enthalpy of liquefaction of the adsorptive.

BET isotherm corresponds to practice of surface area measurement, as will be described later in section 2.2.3.

Bibliography

- [1] R. D. McCarty, J. Hord, and H. M. Roder, Selected Properties of Hydrogen, National Bureau of Standards Monograph 168, Washington, DC:NBS (1981).
- [2] C. Borusbay and T. Nejat Veziroglu Hydrogen as a Fuel for Spark Ignition Engines, Alternative Energy Sources VIII, Volume 2, Research and Development, Hemisphere Publishing Corp., New York (1989).
- [3] W. Novis Smith and J. G. Santangelo, Hydrogen: Production and Marketing, ACS Symposium, Washington (1980).
- [4] B. D. James, G.N. Baum, F. D. Lomax, Jr., C. E. Thomas, and I. F. Kuhn, Jr., "Comparison of Onboard Hydrogen Storage for Fuel Cell Vehicles," Task 4.2 Final Report under Subcontract 47-2-R31148, prepared for Ford Motor Co. under DOE Prime Contract DE-AC02-94CE50389, Directed Technologies, Inc., 1996.
- [5] R. K. Kunz and R. P. Golde, "High-pressure conformable hydrogen storage for fuel cell vehicles," *Proceedings of the 1999 U.S. DOE Hydrogen Program Review*.
- [6] K. L. Yan, B. G. Sellars, J. Lo, S. Johar, and M. K. Murthy, *Int. J. Hydrogen Energy*, **10**, 517 (1985).
- [7] D. Linden Handbook of Batteries and Fuel Cells, McGraw-Hill, Inc., New York (1984).
- [8] Fuel Choice for Fuel Cell Vehicles: An Overview by the DOE Hydrogen Technical Advisory Panel, May 1999.
- [9] S. Yoshimura and R. P. H. Chang, Supercarbon—Synthesis, Properties and Applications, Springer-Verlag Berlin Heidelberg, New York (1998).

- [10] H. O. Pierson, Handbook of Carbon, Graphite, Diamond and Fullerenes, Noyes Publications, Park Ridge, New Jersey (1993).
- [11] M. S. Dresselhaus, G. Dresselhaus, and P. C. Eklund, Science of Fullerenes and Carbon Nanotubes, Academic Press, San Diego (1996).
- [12] N. B. Brandt, S. M. Chudinov, and Ya. G. Ponomarev, Semimetals I. Graphite and its Compounds, Elsevier Science Publishers, New York (1988).
- [13] G. M. Jenkins and K. Kawamura, Polymeric Carbons, Cambridge University Press, Cambridge, UK (1976).
- [14] R. A. Wessling, Polyvinylidene Chloride, Gordon & Breach, New York (1977).
- [15] A. W. Moore, P. L. Walker, Jr., and P. A. Throver (eds), Chemistry and Physics of Carbon, Marcel Dekker, Inc., New York (1981).
- [16] L. H. Peebles, Carbon Fibers: Formation, Structure, and Properties, CRC Press, Boca Raton (1995).
- [17] M. Inagaki, K. Muramatsu, Y. Maeda, and K. Maekawa, *Synth. Met.*, **8**, 335 (1983).
- [18] J. S. Mattson and H. B. Mark, Jr., Activated Carbon – Surface Chemistry and Adsorption from Solution, Marcel Dekker, Inc., New York (1971).
- [19] J. W. Hassler, Purification with Activated Carbon, Chemical Publishing Co., Inc., New York (1974).
- [20] H. W. Kroto, J. R. Heath, S. C. O'Brien, R. F. Curl, and R. E. Smalley, *Nature (London)* **318**, 162-163 (1985).
- [21] W. Krätschmer, K. Fostiropoulos, and D. R. Huffman, in *Dusty Objects in the Universe*, Proceedings of the 4th Intern. Workshop of the Astronomical Observatory of Capodimonte, Capri, Italy (1989).

- [22] W. Krätschmer, L. D. Lamb, K. Fostiropoulos, and D. R. Huffman, *Nature (London)*, **347**, 354 (1990).
- [23] R. Taylor, J. O. Hare, A. K. Abdul-Sada, and H. W. Kroto, *J. Chem. Soc. Chem. Commun.*, **20**, 1423 (1990).
- [24] H. W. Kroto, *Nature (London)*, **329**, 529 (1987).
- [25] T. G. Schmalz, W. A. Seitz, D. J. Klein, and G. E. Hite, *J. Am. Chem. Soc.*, **110**, 1113 (1988).
- [26] W. I. F. David, R. M. Ibberson, J. C. Matthewman, K. Prassides, T. J. S. Dennis, J. P. Hare, H. W. Kroto, R. Taylor, and R. M. Walton, *Nature (London)*, **353**, 147 (1991).
- [27] R. D. Johnson, G. Meijer, and D. S. Bethune, *J. Am. Chem. Soc.*, **112**, 8983 (1990).
- [28] R. D. Johnson, D. S. Bethune, and C. S. Yannoni, *Accounts of Chem. Res.*, **25**, 169 (1992).
- [29] S. Saito and A. Oshiyama, *Phys. Rev. B*, **44**, 11532 (1991).
- [30] H. D. Beckhaus, C. Ruchart, M. Kas, F. Diederich, and C. S. Toote, *Angew. Chem. int. Edn. engl*, **31**, 63 (1992).
- [31] A. Tokmakoff, D. R. Haynes, and S. M. George, *Chem. Phys. Lett.*, **186**, 450 (1991).
- [32] A. R. Kortan, N. Kopylov, S. H. Clarum, R. M. Fleming, F. A. Thiel, and R. C. Haddon, *Nature (London)*, **355**, 529 (1992).
- [33] P. W. Stephens, L. Mihaly, P. L. Lee, R. L. Whetten, S. M. Huang, R. Kaner, F. Diederich, and K. Holczer, *Nature (London)*, **351**, 632 (1991).
- [34] M. B. Jost, N. Troullier, D. M. Poirier, J. L. Martins, J. H. Weaver, L. P. F. Chibante, and R. E. Smalley, *Phys. Rev. B*, **44**, 1966 (1991).

- [35] J. E. Fischer, *Materials Science and Engineering*, **B19**, 90 (1993).
- [36] J. E. Fischer and P. A. Heiney, *J. Phys. Chem. Solids*, **54**, 1752, (1993).
- [37] C. Pan, M. P. Sampson, Y. Chai, R. H. Hauge, and J. L. Margrave, *J. Phys. Chem.*, **95**, 2944 (1991).
- [38] S. Iijima, *Nature* **354**, 56 (1991).
- [39] L. D. Lamb and D. R. Huffman, *J. Phys. Chem. Solids*, **54**, 1635 (1993).
- [40] R. Saito, G. Dresselhaus, and M. S. Dresselhaus, Physical Properties of Carbon Nanotubes, Imperial College Press, London (1998).
- [41] N. Hamada, S. Sawada, and A. Oshiyama, *Phys. Rev. Lett.*, **68** 1579-1581 (1992).
- [42] A. Thess, R. Lee, P. Nikolaev, H. Dai, P. Petit, J. Robert, C. Xu, Y. H. Lee, S. G. Kim, A. G. Rinzler, D. T. Colbert, G. E. Scuseria, D. Tomanek, J. E. Fischer and R. E. Smalley, 'Crystalline ropes of metallic carbon nanotubes', *Science*, **273**, 483 (1996).
- [43] T. Kazuyoshi, Y. Tokio, and F. Kenichi, Science and Technology of Carbon Nanotubes, Elsevier Science Ltd., New York (1999).
- [44] M. Yudasaka, T. Komatsu, T. Ichihashi, Y. Achiba, and S. Iijima, *J. Phys. Chem. B*, **102**, 4892 (1998).
- [45] T. Guo, P. Nikolaev, A. G. Rinzler, D. Tomanek, D. T. Colbert, and R. E. Smalley, *J. Phys. Chem.*, **99**, 10694 (1995).
- [46] M. S. Kim, N. M. Rodriguez, and R. T. K. Baker, *J. Catal.*, **134**, 253 (1991).
- [47] H. Kayser, *Wied. Ann.*, **14**, 451 (1881).
- [48] J. W. McBain, *Z. Phys. Chem.*, **38**, 471 (1909).

- [49] S. J. Gregg and K. S. W. Sing, Adsorption, Surface Area and Porosity, 2nd Ed., New York (1982).
- [50] P. A. Webb and C. Orr, Analytical Methods in Fine Particle Technology, Micromeritics Instrument Corp., Norcross, GA (1997).
- [51] P. W. Atkins, Physical Chemistry, 4th Ed., New York, Freeman (1990).
- [52] S. Brunauer, The Adsorption of Gases and Vapors. Vol. I. Physical Adsorption, Princeton University Press, Princeton, N.J. (1943).
- [53] A. V. Kiselev, *J. Colloid Interface Sci.* **28**, 430 (1968).
- [54] I. Langmuir, *J. Amer. Chem. Soc.* **40**, 1631 (1918).
- [55] I. Langmuir, *J. Amer. Chem. Soc.* **38**, 2221 (1916).
- [56] S. Brunauer, P. H. Emmett, and E. Teller, *J. Amer. Chem. Soc.* **60**, 309 (1938).
- [57] S. Ono and S. Kondo, Molecular Theory of Surface Tension in Liquids, Springer, Berlin (1960).

Chapter 2 Experimental Techniques, Equipment, and Data Analysis

2.1 Sample Preparation and Modification

2.1.1 Nanofiber Synthesis

Carbon nanofiber samples for this investigation were prepared by the catalytic decomposition of hydrocarbons, as introduced in 1.3.5. In order to generate a range of fiber sizes and morphologies, we used Fe - Cu catalysts of different compositions, produced by either mechanical alloying, gas condensation or wet chemical methods.

Mechanically alloyed catalysts were prepared by high energy ball milling in a SPEX¹ 8000 shaker mill, using Fe and Cu powders in appropriate proportions [1]. The grain size of the catalyst powder is essentially related to the duration of ball milling. It can be monitored by the broadening of X-ray diffraction peaks.

The chemical method consisted of reduction of Fe and Cu nitrate precursors using the generic conditions of Rodriguez and Baker for the synthesis of catalysts that produce high yields of graphite nanofibers [2, 3, 4]. Fe and Cu was introduced onto the support by impregnation from an aqueous solution of the mixed metal nitrates. Calcination in oxygen at about 300°C resulted in the conversion of the metal salts to mixed oxides, an essential step if one is to prevent volatilization of the catalyst precursor. Following this relatively mild oxidation treatment, the metal oxide particles were reduced to the alloy state by reduction in hydrogen at about 400°C.

A variation of the gas condensation method was also used to produce catalyst, where nanosize particles were produced by evaporation into an inert gas [5]. Mixed Fe and Cu metal samples were evaporated by electrical resistance heating into a gas

¹SPEX is a trademark of SPEX Industries, Edison, NJ.

of N₂ or He at a pressure of about 3.5 Torr.

Catalysts were placed in a tube furnace, and their surface oxide was reduced using a 7 vol% H₂ in Ar mixture at either 250 or 550°C for 1 hr. The fibers were then grown by passing a mixture of ethylene (C₂H₄) and H₂ gases over the catalysts at a temperature of 600°C.

2.1.2 Krättschmer-Huffman Method – Synthesis of Fullerenes

Several different commercially available fullerene samples were obtained from Alfa Aesar and MER Corp., including pure C₆₀, pure C₇₀, and mixtures of these two referred as *fullerite*.

The fullerene sample from MER Corp. was originally prepared about five years ago. It was made by a carbon arc discharge in helium (Krättschmer-Huffman method) [6]. The carbon soot was treated in toluene. The fullerite was soluble in toluene at the limit of 2 gm/liter and the solution was then spread onto a Teflon tray and quickly evaporated at temperatures from 480 to 520°C.

The fullerite sample from Alfa Aesar was also produced with the classic Krättschmer-Huffman method. The raw material obtained from the carbon arc discharge was also purified with toluene. However, the precipitate from the toluene solution was obtained after slow evaporation of the toluene. The precipitate was subsequently washed with petroleum ether. The material then underwent drying to remove the rest of the solvent [7].

Both fullerite samples mentioned above contained about 72-75% C₆₀, 22% C₇₀ and 1-3% higher fullerene molecules.

The pure C₆₀ (or C₇₀) fullerenes were obtained by chromatographic methods, and the purity was 99.9% for C₆₀ and ~98% for C₇₀.

2.1.3 Single-Walled Nanotubes Production

Samples of single-walled nanotubes (SWNT) materials were prepared and purified by the Smalley group at Rice University [8].

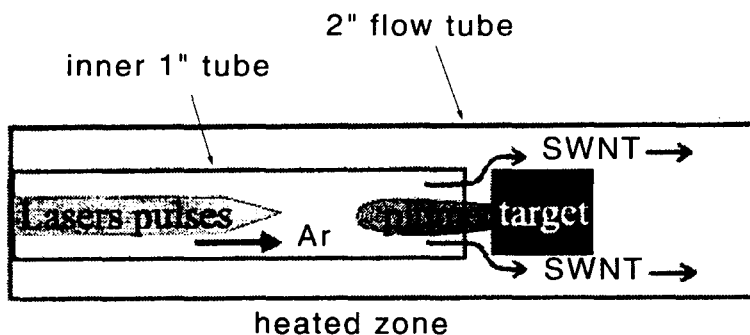


Figure 2.1: The configuration in the 2" system with about 1 g/day production rate (from [8]).

A dual pulsed laser vaporization (PLV) technique was employed for the generation of SWNT.

As shown in Figure 2.1, a 2"-diameter horizontal flow tube within a tube furnace was held at elevated temperature and arranged to maintain an argon atmosphere flow at a controlled pressure. Laser pulses from two Spectra Physics GCR-250 lasers, each running at 30 Hz, entered the flow tube through a Brewster angle window on the front flange and propagated coaxially down the tube in the same direction as the Ar flow. The target sitting coaxially in the flow tube was a 1"-diameter, 1"-long balance carbon cylinder with Co and Ni of 1 at.% each. The ablation occurred from the target's circular end face, and laser pulses were rastered across the entire face. SWNTs condensing from the laser vaporization plume were entrained in the Ar flow to be swept downstream and deposit on the quartz tube walls outside the heated zone. In order to increase the yield of SWNTs, a 1"-diameter quartz tube was added coaxially with the 2" tube extending from the front flange to within 4 mm of the target face. This 2" apparatus was capable of generating about 1g/day of material containing 60-90 vol.% SWNTs. The production conditions were: 1200°C, 100 sccm flowing argon, 500 Torr, first laser pulse 532 nm, 490 mJ/P, 6-mm-diameter spot, second laser pulse 1064 nm, 550 mJ/P, over-lapping 6-mm spot with 42 nS delay between pulses.

The raw material was first purified by a reflux in 2-3 M nitric acid for 45 hours.

Typically 1 liter of acid was used for every 10 g of sample. Weight loss is about 70% after 24 hours with little further weight loss after this time. The resulting black solution was centrifuged, leaving a black sediment at the bottom of the centrifuge bottle and a clear, brownish-yellow supernatant acid, which is decanted off. The remaining acidic sediment is washed with deionized water to re-suspend it, and centrifuged repeatedly until the solution is nearly neutral. The post-acid solids are then filter washed with mildly basic solution, usually a pH 11 NaOH solution with a standard method of hollow-fiber, cross-flow filtration (CFF). Filter washing with deionized water followed. The SWNT solution was vacuum filtered off the liquid through a PTFE membrane. When a sufficiently thick SWNT layer was formed, it might readily be peeled off the membrane to produce a freestanding mat called 'bucky paper'. The yield was typically 10-20%, depending upon the quality of the initial raw material.

Despite the dramatic improvement in the SWNT purity, high-resolution TEM images showed that the material still contained a significant quantity of impurities. In order to remove these, further oxidizing acid treatments were employed. A (3:1) mixture of sulfuric (98%) and nitric (70%) acids was stirred and maintained at 70°C in an oil bath for 20-30 min. This is followed by another CFF cycle as described above. The final purification is done with a (4:1) mixture of sulfuric acid and hydrogen peroxide following the same procedure as with the sulfuric/nitric mixture. A vacuum bake at 1200°C was used for final purification of the bucky paper.

2.1.4 Sonication and Filtration

To modify the morphology of the SWNTs and cut the SWNT's, the samples were sonicated in dimethyl formamide [9]. The as-received SWNT sample from Rice's group was in the shape of a piece of black paper. Then it was cut into much smaller pieces of about a fraction of cm². A N,N-Dimethyl-Formamide (HCON(CH₃)₂) with purity of 99.8% was used as the media in a ultra-sonic bath. The ratio of the sample to the solvent was about (0.1 mg) : (1 ml). It took more than ten hours before the sample was completely detached and suspended in the solvent. A vacuum filtration

system was set up to separate the black, cloudy suspension from the solvent, as shown schematically in Figure 2.2. A Büchner funnel with 10 micron filter was used. A water trap is necessary to prevent any solvent from being accidentally sucked into the vacuum line. After it was completely dried, the modified SWNT sample was carefully peeled off from the filter of the Büchner funnel. The yield of this process was about 80%.

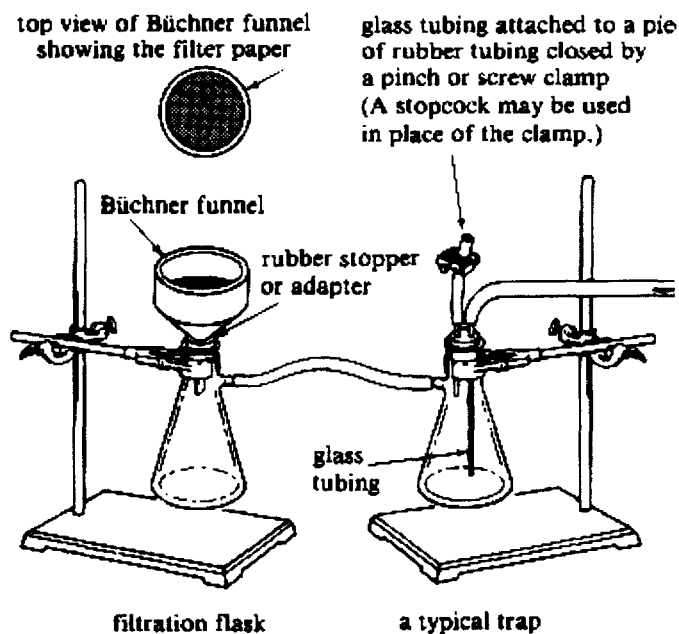


Figure 2.2: Vacuum trap for filtration (from [10]).

2.1.5 Catalyst Impregnation

Background

Supported catalysts have been widely used in chemical engineering. There are a number of advantages in depositing catalytically active metals on a porous support. The metal can be highly dispersed in the form of small crystallites, thus a large active metal surface is produced relative to the weight of metal used.

Catalysts can be prepared by different techniques including impregnation, adsorption from solution, deposition and precipitation/co-precipitation. The preparation of

impregnated catalysts commonly involves several steps:

impregnation step: contacting a dry or wet support with an impregnating solution which consists of a compound of the desired catalytic constituent dissolved in a liquid

drying step: drying the resulting mixture from impregnation step

activation step: calcining and/or reducing if necessary

The catalytic activity may be very sensitive to the details of the procedures, such as solution concentration, contact time, washing, method and condition of calcination and reduction, which may influence the degree of metal dispersion and uniformity of distribution over the support. Changing a preparative variable may vary the catalyst structure and its characteristics (metal area, crystallite size, distribution and dispersion), which are directly related to the performance of the catalyst.

Some commonly used catalysts and their compounds used to prepare the catalysts are listed in Table 2.1.

Metal	Metal compounds
Pt	H_2PtCl_6 , $[\text{Pt}(\text{NH}_3)_4]\text{Cl}_2$, $[\text{Pt}(\text{NH}_3)_4](\text{OH})_2$
Pd	PdCl_2 , $[\text{Pd}(\text{NH}_3)_4]\text{Cl}_2$
Ni	$\text{Ni}(\text{NO}_3)_2 \cdot 6\text{H}_2\text{O}$
Co	$\text{Co}(\text{NO}_3)_2 \cdot 6\text{H}_2\text{O}$
Cu	$\text{Cu}(\text{NO}_3)_2 \cdot 6\text{H}_2\text{O}$
Rh	RhCl_3 , $(\text{NH}_4)_3\text{RhCl}_6$
Ru	RuCl_3
Ag	AgNO_3 , $\text{Ag}(\text{NH}_3)_2\text{NO}_3$
Au	HAuCl_4

Table 2.1: Selection of metals and metal compounds.

Factors Influencing Impregnation Profiles

Each step of preparation process has its impact on the impregnation profile. During impregnation of the solution, the concentration of the solution, the metal com-

pounds' readiness to be absorbed onto the substrate and capillarity will all contribute to the impregnation profile. The take-up of the solution is governed by the porous structure of the support. During the subsequent drying step, the segregation and evaporation speed should be taken into consideration. For the activation step, conditions of calcination and reduction, such as temperature and gas composition, need to be controlled properly.

Preparative Techniques

Catalysts are commonly produced by liquid-phase impregnation in which a dry or wet pellet of the porous support is impregnated with a solution of a compound of the desired catalytic constituent.

Nickelous nitrate, 6-Hydrate ($\text{Ni}(\text{NO}_3)_2 \cdot 6\text{H}_2\text{O}$) solutions with different concentrations were prepared. Designated amounts of solution were added into the support sample. The mixture was stirred continuously until a smooth paste was obtained. Super sonic bath was employed if necessary, to mix the solution and the support particles thoroughly. It is believed that sonication treatment is beneficial to the reactivity of solid catalysis by the creation of surface defects, the reduction of particle size, and the dispersion of the catalyst particles on the support [15].

Let the wet paste sit inside the hood for at least several hours until the carbon powder was completely dry. This was to ensure that the impregnated component remained in the pore system instead of migrating to the exterior surface of the support.

A quartz chamber was set up for the reduction process. The size of the chamber was specially designed to fit to a Lindberg furnace, and it was good for a small amount of powder sample, up to 3 grams. The powder was put into the middle of chamber with quartz wool plugged onto both ends to prevent the sample from migrating around. Before raising the temperature, the chamber was purged with N_2 gas for about ten minutes to drive away the oxidative atmosphere. H_2 was used as the reducing gas, flowing through the carbon powder to reduce nickelous nitrate into nickel at elevated temperatures ($\sim 400 - 500^\circ$). The flow rate of hydrogen was monitored using a water trap of the outlet gas by about one bubble per second. The reduction process took

one to two hours. Then the flowing gas was switched back to N_2 and the furnace was turned off. The sample was cooled down to ambient temperature slowly inside the furnace.

The nickel crystallites were characterized by X-ray diffractometry and transmission electron microscopy.

2.2 Sample Characterization

2.2.1 X-ray Diffraction

X-ray diffractometry (XRD) was used to obtain information about sample compositions, crystal structure and lattice parameters, phase transformation, and catalyst particle size. Diffraction patterns were collected by an Inel CPS-120 diffractometer system using $Co\ K\alpha$ radiation ($\lambda = 1.788965\text{\AA}$) and a curved position sensitive detector (PSD) spanning 127° in 2θ .

Basic Physics

When a monochromatic, unpolarized electric field is incident onto a crystalline lattice, the scattered wave $\Psi(\Delta\mathbf{k})$ can be calculated as [11]

$$\Psi(\Delta\mathbf{k}) = \mathcal{S}(\Delta\mathbf{k}) \mathcal{F}(\Delta\mathbf{k}) \quad (2.1)$$

where $\mathcal{S}(\Delta\mathbf{k})$ is called shape factor, which is a sum over all the lattice sites of the crystal (all unit cells):

$$\mathcal{S}(\Delta\mathbf{k}) = \sum_{\mathbf{r}_g}^{lattice} \exp(-2\pi i \Delta\mathbf{k} \cdot (\mathbf{r}_g - \mathbf{s})) \quad (2.2)$$

and $\mathcal{F}(\Delta\mathbf{k})$ is known as the structure factor, which is a sum over the atoms in the basis (all atoms in the unit cell):

$$\mathcal{F}(\Delta\mathbf{k}) = \sum_{\mathbf{r}_k}^{basis} f_{atom}(\mathbf{r}_k) \exp(-2\pi i \Delta\mathbf{k} \cdot \mathbf{r}_k) \quad (2.3)$$

- $\Delta\mathbf{k}$: diffraction vector (hkl)
- \mathbf{s} : deviation vector
- \mathbf{r}_g : unit cell positions in the defect-free crystal
- \mathbf{r}_k : unit cell basis vector
- f_{atom} : atomic scattering factor of atom at \mathbf{r}_k

When the diffraction conditions are satisfied, the relation between the incident wavelength and crystalline lattice spacing meets the Bragg law as

$$\lambda = 2d_{hkl} \sin \theta \quad (2.4)$$

where d_{hkl} is the crystalline lattice spacing. For cubic crystals with lattice parameter a_0 , the interplanar spacing d_{hkl} can be calculated as

$$d_{hkl} = \frac{a_0}{\sqrt{h^2 + k^2 + l^2}} \quad (2.5)$$

Sometimes, $Q(\text{\AA}^{-1})$ is used as abscissa unit in XRD pattern. It may easily be converted from 2θ .

$$Q = \frac{2\pi}{d} = \frac{4\pi}{\lambda} \sin \theta \quad (2.6)$$

X-ray Line Broadening

The Scherrer equation relates the mean dimension D of the powder crystallites and the X-ray diffraction broadening β as

$$D = K\lambda/\beta \cos \theta \quad (2.7)$$

where λ is the radiation wavelength, θ is the Bragg angle, and K is the Scherrer constant approximately equal to unity and related both to crystallite size and the way β and D are defined. In order to evaluate β , it is necessary to correct the observed broadening B for instrumental effects. B is the full-width-at-maximum (FWHM) in radius. Stokes showed that the instrumental correction was best done by a deconvolution analysis using Fourier methods and the instrumental profile observed from a sample in which intrinsic sources of broadening (size and strain) are absent [12]. A practical method to derive the true diffraction breadth uses a simple correction, valid for Gaussian functions:

$$B^2 = \beta^2 + b^2 \quad (2.8)$$

where b is the instrumental broadening and B is the observed broadening of the X-ray peak. Wagner and Aqua's correction [13]

$$\beta = B - b^2/B \quad (2.9)$$

provides an improvement for typical X-ray lineshapes.

For a given crystal dimension D , the peak breadth increases as $\cos \theta$ decreases. Hence the particle size broadening becomes more pronounced at large values of θ .

2.2.2 Transmission Electron Microscopy

The morphologies of the samples were studied by transmission electron microscopy (TEM) with either a Philips EM 420 or a Philips EM 430 microscope. The Philips EM 420 was operated at 120 kV, while EM 430 was operated at 130 kV.

The technique of preparing the TEM samples was quite simple. Most of the samples examined were in the form of a black powder. The procedure of preparation includes the following steps: Mix a few drops of iso-propanol into the powder and stir for half a minute. Dip the copper TEM grid into the suspension and take it out quickly. Let it dry in the air. Before loading the sample into the vacuum chamber of microscope, blow off the large particles, which are loosely attached to the grid, to

avoid contamination of the microscope.

2.2.3 BET

The surface area is determined by measuring the amount of gas adsorbed in a monolayer. The total surface area S is obtained from the product of two quantities: the number of molecules needed to cover the sample with a monolayer of adsorbate $a_m N_A$ and the amount of surface occupied by a molecule of a particular adsorbed species s_0 :

$$S = a_m N_A s_0 \quad (2.10)$$

where a_m is the number of moles of gas adsorbed in the monolayer and N_A is the Avogadro number. The values of a_m can be found from the measurement of the amount of adsorbed gas and an adsorption isotherm, as discussed in Chapter 1.4. For monolayer adsorption, the simple Langmuir isotherm is given as

$$\frac{a}{a_m} = \frac{K P_r}{1 + K P_r} \quad (2.11)$$

where $P_r = P/P^o$ and a is the amount of gas adsorbed at Pressure P .

In practical work, the semi-empirical equation of Brunauer, Emmet and Teller (1.9) is used:

$$\frac{a}{a_m} = \frac{c P_r}{(1 - P_r)[1 - (1 - c)P_r]} \quad (2.12)$$

The BET equation contains two unknown constants a_m and c . Hence measurements of a at two pressures are enough to find a_m and, consequently, S . Sometimes, for adsorbed gases $c \gg 1$, the BET equation simplifies to

$$a = \frac{a_m}{1 - P_r}$$

provided $P_r \gg 1/c$. Thus it requires measurement only at one point. Usually $c \approx 1$, since the heat of adsorption and evaporation are usually almost equal. In this case, the more general BET equation must be used [14].

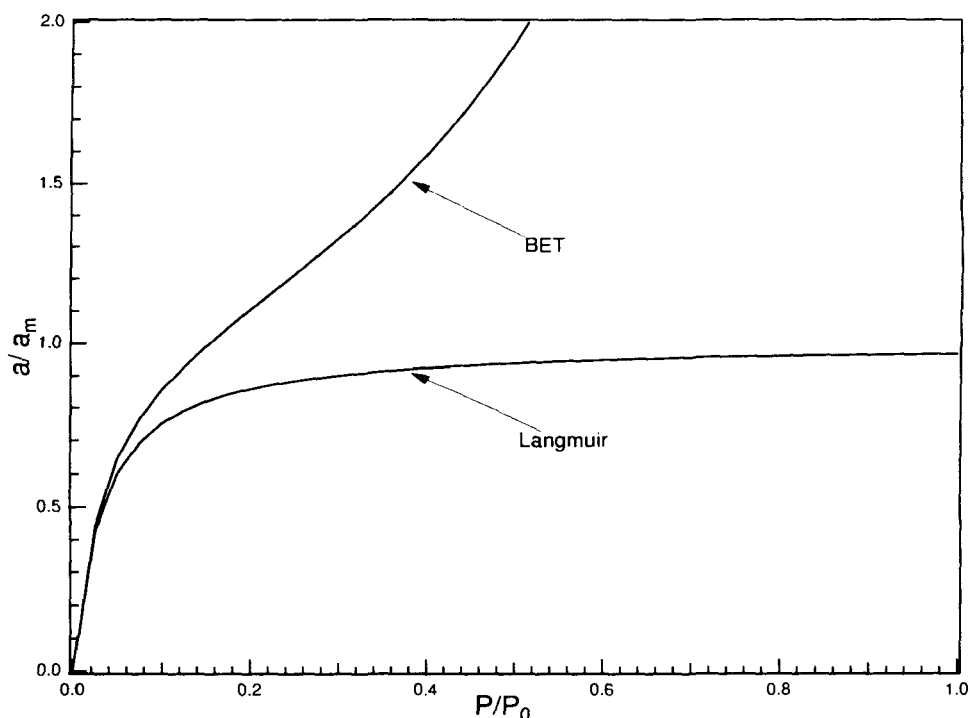


Figure 2.3: Physical adsorption isotherms: Langmuir ($K=30$) and BET ($c=30$) isotherm.

For many systems, the BET equation holds in the range $P_r = P/P_0 \sim 0.05 - 0.3$. Any condensable inert vapor can be used in the BET method. However, for reliable measurements, the molecules should be small and approximately spherical. P_r values of 0.05-0.30 are conveniently attainable. The choice is usually nitrogen, in which case measurements are executed at cryogenic temperatures, using liquid nitrogen as coolant. The boiling point of nitrogen at atmospheric pressure is -195.8°C . The effective cross-sectional area of an adsorbed molecule of nitrogen is usually taken to be 0.162 nm^2 .

A Micromeritics ASAP 2010 BET surface analysis apparatus was employed, using N_2 gas. The ASAP 2010 system consists of an analyzer, a control module for entering analysis and report options, and an interface controller, which controls analyses. As shown in Figure 2.4, the analyzer contains two sample preparation ports and one analysis port. In-line cold traps are located between the vacuum pump and the manifold in both the analysis and the degas system.

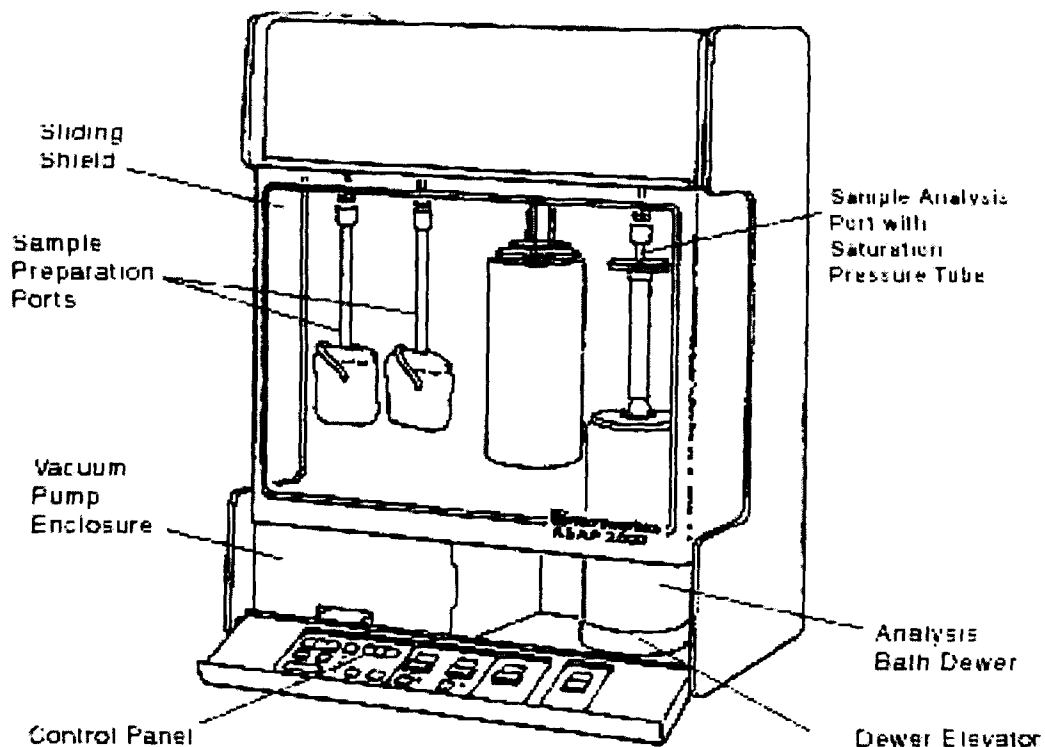


Figure 2.4: Micromeritics ASAP 2010 BET surface analysis apparatus.

In general, a sample with a total surface area of 40 to 120 square meters provides best results for nitrogen analysis. Smaller areas may cause variability of results; considerably more than this unnecessarily extends the time required for analysis.

The sample was degassed at about 150 to 200°C in the sample tube with a heating mantle for more than 10 hours before the measurement was performed.

The BET method is unlikely to yield a value of the true surface area if the isotherm is of either Type I or Type III (1.4.2); on the other hand, both Type II and Type IV isotherms are, in general, amenable to the BET analysis.

2.2.4 Fourier Transform Infrared Spectroscopy

Infrared spectroscopy is the study of the interaction of infrared light with matter. When infrared radiation interacts with matter it can be absorbed, causing the chemical bonds in the material to vibrate. Chemical structural fragments within molecules, known as *functional groups*, tend to absorb infrared radiation in the same wavenumber range regardless of the structure of the rest of the molecule. The correlation between the wavenumbers and molecule structure makes it possible to identify the structure of unknown molecules. For instance, the peaks around 3000 cm^{-1} are due to CH bond stretching. Infrared spectroscopy is a useful chemical analysis tool.

Pure vibrational spectra are observed in the range between 10^2 cm^{-1} ($10^2\mu\text{m}$) and 10^4 cm^{-1} ($1\mu\text{m}$). Although vibrational spectra are observed experimentally as infrared or Raman spectra, the physical origins of these two types of spectra are different. Infrared spectra originate in transitions between two vibrational levels of the molecule in the electronic ground state and are usually observed as absorption spectra in the infrared region. On the other hand, Raman spectra originate in the electronic polarization caused by ultraviolet or visible light. If a molecule is irradiated by monochromatic light of frequency ν , then, because of electronic polarization induced in the molecule by this incident light, light of frequency ν (Rayleigh scattering) as well as of $\nu \pm \nu_i$ is emitted (ν_i represents a vibrational frequency) [18].

The *wavenumber* of a light wave is defined as the reciprocal of the wavelength

$$W = 1/\lambda \quad (2.13)$$

where λ is the wavelength. W is usually reported as cm^{-1} .

To obtain the transmission spectrum, samples were prepared into potassium bromide pellets, which is a suitable sampling technique for powder samples. KBr is an inert, infrared transparent material. It acts as a support and a diluent for the sample. Approximately 1 mg sample and 200 mg KBr were ground and mixed in the mortar. The sample/KBr mixture was then placed in a press and pressed into a transparent pellet. The pellet was then placed in a pellet holder to obtain the spectrum. Also,

functional groups or molecules	absorbance wavenumber (cm^{-1})		references
H ₂ O	3900-3400	1850-1350	[17]
CO ₂	2350	667	[17, 18]
CH	3000-2900		[17]
HH	4395		[18]
NiH	2200	1927	[18]
C ₆₀	1428	1183	
C ₇₀	1585	1483	

Table 2.2: Absorbance wavenumbers of some functional groups and molecules.

background spectrum was obtained on the empty pellet holder.

KBr is a hygroscopic material, which means it will absorb water directly from the atmosphere. Thus it is difficult to study the OH bond stretching absorbance peak, around 3400 cm^{-1} .

2.3 Sample Measurement and Data Analysis

2.3.1 Sievert's Apparatus

An automated Sievert's apparatus was used to perform all the isotherm measurements with hydrogen.

Our Sieverts' apparatus (i.e., a volumetric system for quantitative measurement of gas absorption and desorption by solids) used metal seals, an oil-free vacuum pumping system and research purity hydrogen gas [19]. Pneumatic valve operation and pressure and temperature data monitoring were computer controlled, permitting automatic isotherm data collection. The system was thoroughly leak checked at 200 bar and calibrated to ensure reliable determination of the hydrogen storage properties. A schematic drawing of Sievert's apparatus is shown in Figure 2.5.

All tubing and fittings used were 1/4" 316 stainless steel with Swagelok VCR fittings. Manual valves were Nupro bellows valves, VS51C. Pneumatic valves were

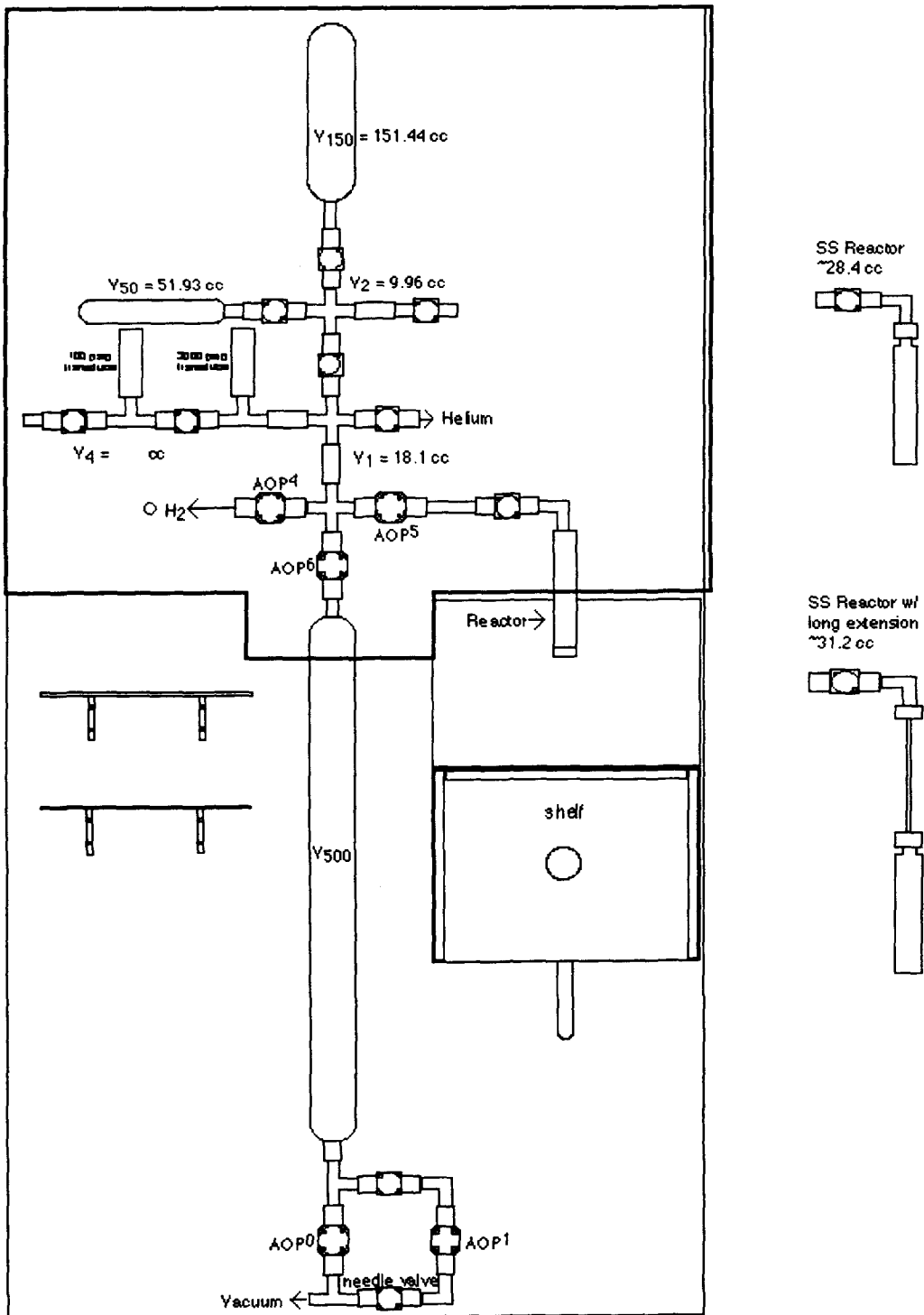


Figure 2.5: Schematic drawing of Sievert's apparatus.

actuated by small solenoid valves. Pressure measurements were made with SETRA pressure gauges. Isotherms could be measured at high pressures (up to 2000 psia) at 0.1 psi accuracy or at low pressures (100 psig) at 0.01 psi accuracy. These gauges were calibrated by mounting a 600 psig manual Heise gauge on the system. Zero pressure was read by a Granville-Philips convectron gauge, giving a zero reading of $< 1 \times 10^{-4}$ torr. Reactor and room temperatures were measured with K-type thermocouples from Omega.

The manifold and reactor volumes were calibrated with high-purity helium gas. A 150 ml volume, V_{150} , was initially calibrated at Aerojet Aerospace Corp. and used as the reference volume in gas-expansion volume measurements. It was possible to vary the manifold volume by opening manual valves isolation calibrated volumes. The hydrogen used for measurements was Matheson ULSI 6.0 hydrogen (99.9999%). It was connected to the Sieverts' apparatus with electropolished SS tubing to a brass regulator. A tribodyn oil-free shaft driven mechanical pump manufactured by Danielson was used to evacuate gas from the system. A hot air gun was used to heat the sample reactor to a maximum of 300°C for sample bake-out. When extended hours of degassing was necessary, a heating tape was employed to obtain the elevated temperature by wrapping it around the reactor. It is possible to maintain the temperature at designated range, accurate to $\pm 1.0^\circ\text{C}$. Isotherms at low temperatures were measured with the reactor immersed into liquid nitrogen in a dewer with volume of about 5 litres. To minimize the fluctuation of pressure due to the evaporation of liquid nitrogen, a special connection part designed and prepared by Hughes Research Laboratory was adopted, as shown in Figure 2.5. It connected the reactor and manifold with a thin and long tubing, which part was around the interface of liquid nitrogen and atmosphere during the isotherm measurements. Thus, even though the level of liquid nitrogen changed due to evaporation, the volume of gas being affected was relatively small since the inner diameter of the connecting tubing is very small. With a soft plastic lid, one dewer of liquid nitrogen could last for at least 8 hours and the fluctuation of pressure was less than 1 psi at the pressure of 1500 psia.

The analog readings from the pressure and temperature gauges were converted

by a Strawberry Tree PCI board interfaced to a Macintosh SE computer. The SE read and recorded the pressure data and operated the relay-solenoid-pneumatic-valve chain used to control the pressure of the hydrogen gas in the apparatus. The program used to operate the equipment and acquire data was written in the C programming language.

The sample reactor was a double walled tube made of 1/16" copper pipe electron-beam welded to a 3/4" 316 stainless steel male Swagelok VCR flange. Several VCR porous metal filter gaskets with pore size 0.5 μm were used to prevent the sample from migrating into the system and contaminating the valves.

2.3.2 Hydrogen Compressibility and Ideal Gas Correction

The ideal gas equation of state gives:

$$n = \frac{PV}{RT} \quad (2.14)$$

where n is the number of moles in a known volume at a known temperature.

At very low density, hydrogen approaches ideal gas behavior. At higher densities, the behavior may deviate substantially from the above equation. Thus, the observed pressure of H_2 is too high to give correct results when used in ideal gas equation to find n .

To obtain correct n , the observed pressure P_0 must be divided by the compression factor Z to yield a corrected pressure P_c ,

$$P_c = \frac{P_0}{Z} \quad (2.15)$$

Z is given by

$$Z = A_0 + A_1P + A_2P^2 + \dots + A_nP^n \quad (2.16)$$

The coefficients A_i depend on the gas and temperature and decrease rapidly with n . I use only the first three A 's and they are given as functions of temperature (P must be in atmosphere),

$$A_0 = 1.000547 - 6.07 \times 10^{-7} \times T$$

$$A_1 = 0.000912 - 1.0653 \times 10^{-6} \times T$$

$$A_2 = (7.373407 - 0.01901T) \times 10^{-7}, \quad \text{for } T < 100^\circ\text{C}$$

$$A_2 = 0, \quad \text{for } T > 100^\circ\text{C}$$

Figure 2.6 shows a detailed compressibility chart for hydrogen. Note that at temperatures of 300 K and above, the compressibility factor is near unity up to pressure of 10 MPa.

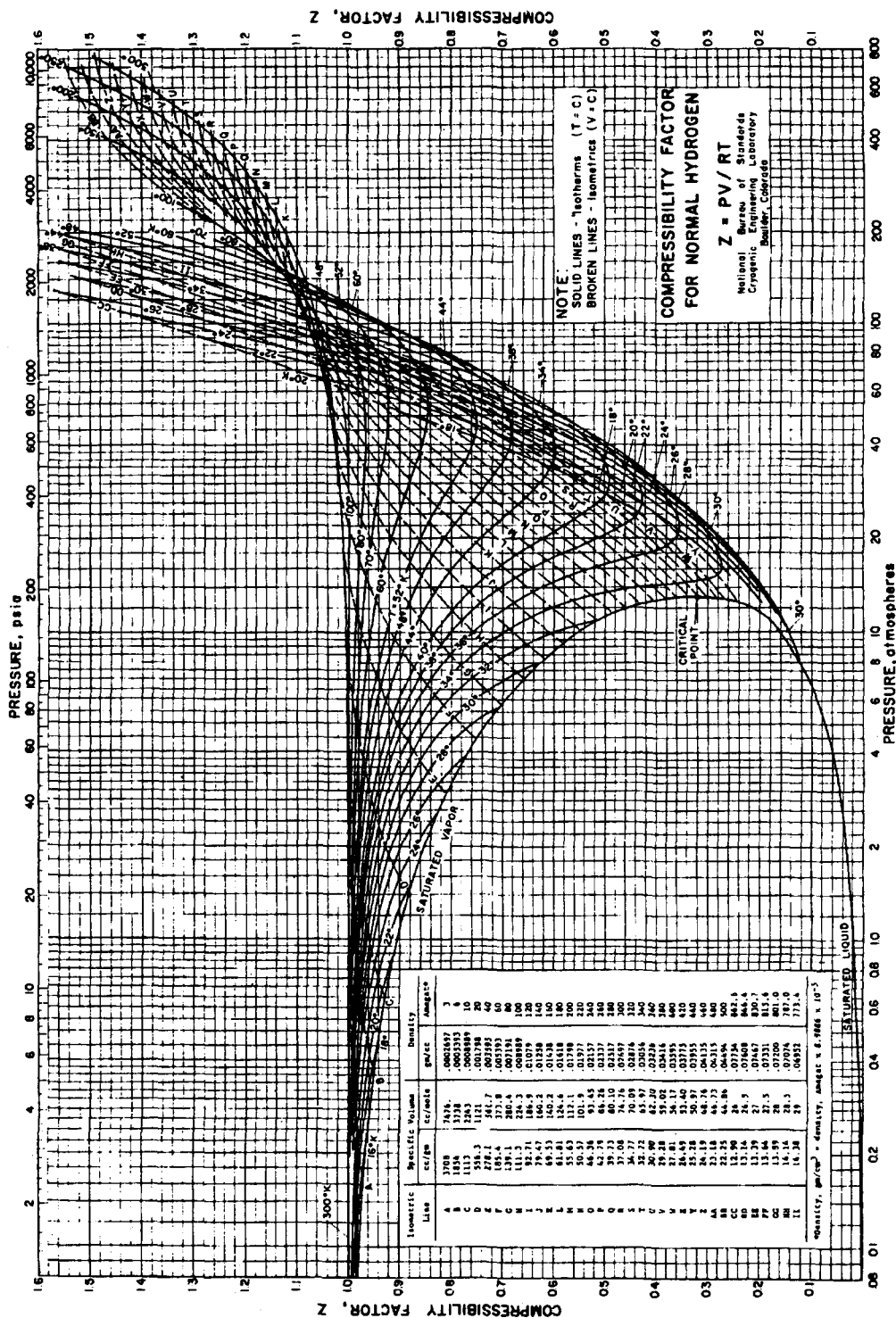


Figure 2.6: Compressibility factor for hydrogen.

Bibliography

- [1] B. Fultz, C. C. Ahn, S. Spooner, L. B. Hong, J. Eckert, and W. L. Johnson, *Metall. Trans.* **27A**, 2934 (1996).
- [2] N. M. Rodriguez and R. T. K. Baker, "Storage of Hydrogen in Layered Nanostructures," U. S. Patent #5,653,951. Issued Aug. 5, 1997.
- [3] N. M. Rodriguez, *J. Mater. Res.*, **8**, 3233 (1993).
- [4] N. M. Rodriguez, A. Chambers, and R. T. K. Baker, *J. Phys. Chem. B*, **102**, 4253 (1998).
- [5] B. Fultz, C. C. Ahn, E. E. Alp, W. Sturhahn, and T. S. Toellner, *Phys. Rev. Lett.* **79**, 937 (1997).
- [6] W. Krätschmer, L. D. Lamb, K. Fostiropoulos, and D. R. Huffman, *Nature (London)*, **347**, 354 (1990).
- [7] Information was obtained from Alfa Aesar Co.
- [8] A. G. Rinzler, J. Liu, H. Dai, P. Nikolaev, C. B. Huffman, F. J. Rodriguez-Macias, P. J. Boul, A. H. Lu, D. Heymann, D. T. Colbert, R. S. Lee, J. E. Fischer, A. M. Rao, P. C. Eklund, and R. E. Smalley, *Appl. Phys.* **A 67**, 29 (1998).
- [9] J. Liu, unpublished results.
- [10] R. J. Fessenden and J. S. Fessenden, Organic Laboratory Techniques, Brooks/Cole Publishing Company, Pacific Grove (1993).
- [11] B. Fultz and J. Howe, Transmission Electron Microscopy and Diffractometry of Materials, (in preparation).

- [12] A. R. Stokes, *Proc. Phys. Soc. London*, **61**, 382 (1948).
- [13] C. N. J. Wagner and E. N. Aqua, *Advan. X-ray Anal.*, **7**, 46 (1964).
- [14] R. J. Wijngaarden, A. Kronberg, and K. R. Westerterp, Industrial Catalysis, WILEY-VCH Verlag GmbH, Weinheim, 1998.
- [15] S. Ley and C. Low, Ultrasonics in Synthesis, Springer-Verlag, Berlin Heidelberg (1989).
- [16] A. Chambers, C. Park, R. T. K. Baker, and N. M. Rodriguez, *J. Phys. Chem. B*, **102**, 4253 (1998). *Langmuir*, **11**, 3862 (1995).
- [17] B. C. Smith, Fundamentals of Fourier Transform Infrared Spectroscopy, CRC Press, Inc., New York (1996).
- [18] K. Nakamoto, Infrared and Raman Spectra of Inorganic and Coordination Compounds, 4th edition, John Wiley & Sons Inc. Canada (1986).
- [19] R. C. Bowman, Jr., C. H. Luo, C. C. Ahn, C. K. Witham, and B. Fultz, *J. Alloys Comp.*, **217**, 185 (1995).
- [20] R. A. Wessling, Polyvinylidene Chloride, Gordon & Breach, New York, 1977.
- [21] Y. Zhou and L. Zhou, *Sci. in China B* **39**, 598 (1996).
- [22] M. Nielsen, J. P. McTague, and W. Ellenson, *J. Phys.* **38** C4/10-C4/18 (1977).
- [23] R. Chahine and T. K. Bose, *Int. J. Hydrogen Energy* **19**, 161 (1994).
- [24] S. D. M. Brown, G. Dresselhaus, and M. S. Dresselhaus, *Mat. Res. Soc. Proc.* **497**, 157 (1998).

Chapter 3 Hydrogen Desorption and Adsorption Measurements on Graphite Nanofibers

3.1 History and Commercial Interests

Diminishing worldwide reserves of fossil fuels, and the recognition of the global environmental impact of combustion byproducts, motivates the search for practical alternative fuels. While hydrogen has a low energy density on a per volume basis, and while there is as of yet no infrastructure for its distribution, it remains the most attractive source for use in either direct internal combustion, or for fuel cell applications, as water is the primary byproduct. The most serious impediment to the use of hydrogen as a transportation fuel, however, is the lack of a suitable means of on-board storage. Compressed gas storage is bulky and requires the use of high strength containers. Liquid storage of hydrogen requires temperatures of 20K and efficient insulation. Solid state storage offers the advantage of safer and more efficient handling of hydrogen, but promises at most 7% hydrogen by weight and more typically 2%. There has therefore been considerable interest in recent reports by Nelly Rodriguez's group at Northeastern University [1] that certain carbon graphite nanofibers [2] can absorb and retain 67 wt% of hydrogen gas at ambient temperature and moderate pressures (i.e., up to 23 standard liters or 2 grams of hydrogen per gram of carbon at 50 to 120 bar).

The nanofibers produced were described as "the graphite platelets are arranged parallel, perpendicular, or at an angle with respect to the fiber axis." Results on several morphologies of graphite nanofibers, including tubular, herringbone, and platelet, were reported [1]. None of them showed less than 11 wt% storage capacity. The high-

est levels reported would mean that a practically-sized fuel container could give a vehicle an 8000 km range.

When purified graphite nanofiber samples were allowed to interact with hydrogen at 25°C and an initial pressure of 112 atm, a drop in the pressure was reported to be observed over a period of 24 hours. Upon equilibrium, hydrogen was desorbed by opening a regulating valve. It was reported that there was a difference in the amount of hydrogen adsorbed and desorbed at room temperature, and heating was required for complete releasing of hydrogen.

Such claims are especially noteworthy, given that, until recently, the typical best value of hydrogen adsorption in carbon materials has been on the order of 4 wt%, or 0.5 H/C atom (although there is also a recent claim that up to 10 wt% was achieved for H storage in single wall nanotubes[3]). Owing to the potential importance of new materials with high hydrogen storage capacity for the world-wide energy economy, transportation systems and interplanetary propulsion systems, we have synthesized graphitic structures of appropriate morphology in order to make our own measurements of hydrogen absorption and desorption.

3.2 Catalysts and Sample Preparation

Several graphite nanostructured materials were prepared using Fe-Cu catalysts of different compositions, in order to generate a range of fiber sizes and morphologies. As described in Chapter 2.1.1, mechanical alloying, gas condensation or chemical methods were employed to produce the catalysts. We prepared a total of ten different materials and they are outlined in Table 3.1.

3.3 Sample Morphology

There were a wide variety of morphologies shown in the graphite nanofiber samples. There was some residual of Na impurities in catalyst for GNF sample #1 and fibrous morphology for carbon. TEM images started to show herringbone mi-

Sample	Catalyst composition	Catalyst Prep. Method	Reduction Temp. (°C)	Composition of Reactant Gas (H ₂ :C ₂ H ₄)	Nanofiber Growth Time (hrs)
GNF#1	Fe ₇₅ Cu ₂₅	chemical method	550	(80:20)	1
GNF#2	Fe ₇₀ Cu ₃₀	chemical method	550	(80:20)	1
GNF#3	Fe ₇₀ Cu ₃₀	chemical method	550	(20:80)	1
GNF#4	Fe ₈₀ Cu ₂₀	chemical method	550	(20:80)	1
GNF#5	Fe ₉₀ Cu ₁₀	mechanical alloying	550	(20:80)	1
GNF#6	Fe ₈₅ Cu ₁₅	mechanical alloying	550	(20:80)	1
GNF#7	Fe ₉₀ Cu ₁₀	gas condensation	550	(20:80)	3
GNF#8	Fe ₉₀ Cu ₁₀	gas condensation	250	(20:80)	3
GNF#9	Fe ₈₀ Ni ₂₀	mechanical alloying	250	(20:80)	3
GNF#10	Fe ₈₀ Ni ₂₀	gas condensation	250	(20:80)	3

Table 3.1: Range of catalyst compositions and reactant gases used to produce graphite nanofibers.

crostructure in some carbon fibers from sample #2 (Figure 3.1) and #3. Sample #5 was more uniform and had smaller diameter of carbon fibers. It showed a range of microstructures including corkscrews, tubes and a significant fraction of fibers with the “herringbone” morphology as shown in Figure 3.2 and Figure 3.3. Figure 3.4 shows a high resolution micrograph of a single fiber, revealing a cavity at the top of the fiber where the FeCu catalyst originally was, and from which the graphitic platelets grew. In some samples, there were carbon nanotubes as well as fibers evident in TEM, as shown in Figure 3.5.

3.4 Isotherm Measurement and Data Analysis

Before measurements of hydrogen adsorption and desorption, the samples were vacuum annealed at 900 °C in order to “activate” the nanofibers.

The Sieverts’ apparatus was thoroughly leak checked at 200 bar and calibrated to ensure reliable determination of the hydrogen storage properties.

Desorption measurements were performed at 77 and 300 K by first placing about 0.3 gram to 0.6 gram of sample in the reactor. H₂ gas was admitted into the evacuated reactor to achieve a typical pressure of 4.5 or 80 bar for the 77 K runs or 180 bar for the 300 K runs. This pressure was maintained for 15 hr to allow the sample to

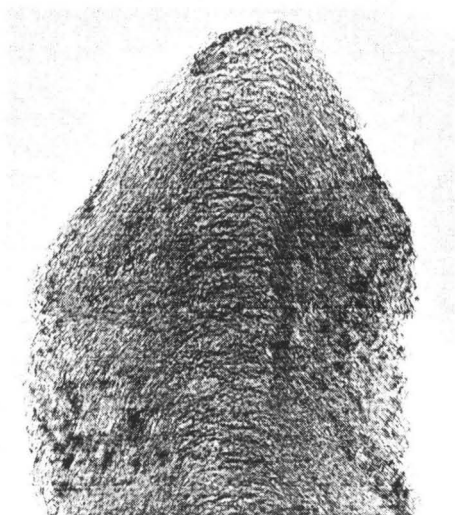


Figure 3.1: High magnification TEM shot of graphite nanofiber sample #2 showing herringbone structure.

reach equilibrium and to check for leaks in the system. The reactor was valved off from the rest of the system and the system was evacuated again. The desorbed H_2 was then measured by a pressure transducer. The raw data (as shown in Figure 3.6) were acquired by a Macintosh SE computer.

For comparison, we also performed measurements on a “saran” carbon, a pure, dense, porous material with high surface area, formed by the pyrolysis of polyvinylidene chloride as described in Chapter 1.3.1. The microstructure of this material consists of graphite microcrystals in an amorphous carbon matrix [9].

A macro program for the software package Igor by Wavemetrics was used to calculate the quantitative mole number of hydrogen before and after each desorption step based on the pressure and the volume of the system. The cumulative difference (Δx) was assumed to be the hydrogen released by the sample inside the reactor. Identical measurements and calculations were also performed on an empty reactor so that the data could be properly corrected for instrument effects. A set of typical measurements for both the sample and the empty reactor are shown in Figure 3.7. Figure 3.8 shows the actual hydrogen desorption capacity of saran carbon after the correction.

In addition to H_2 desorption measurements, sample surface areas were measured

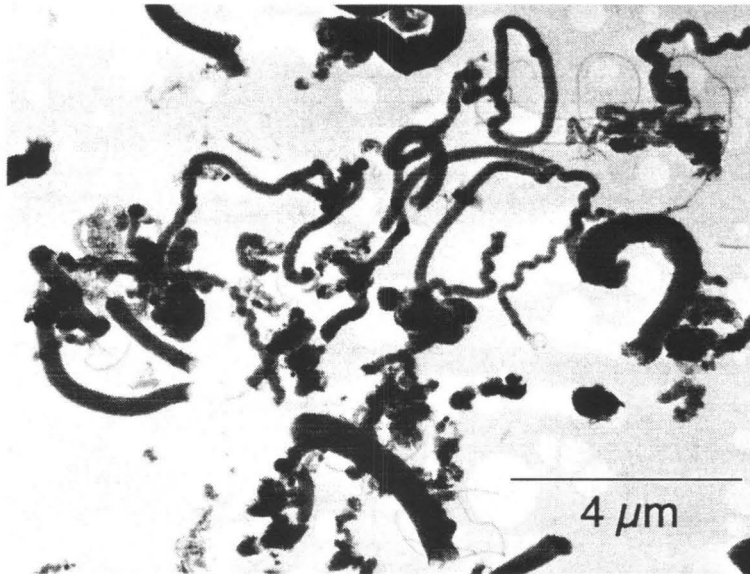


Figure 3.2: Low magnification TEM shot of graphite nanofiber sample #5.

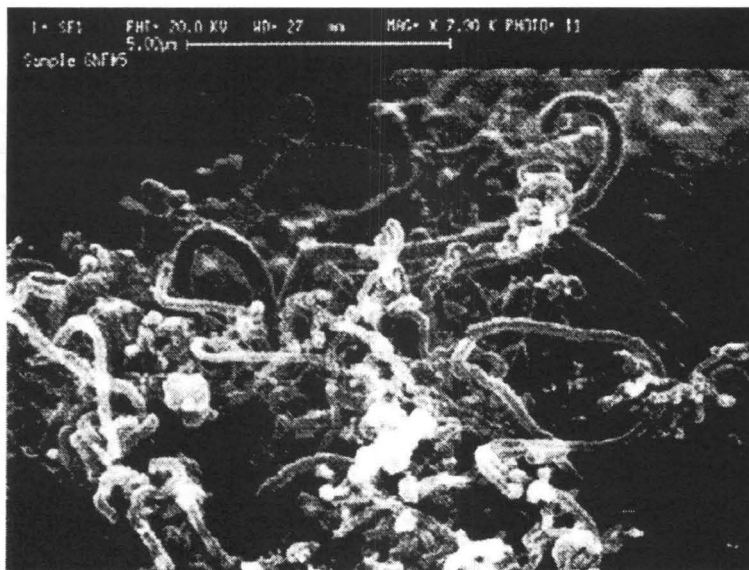


Figure 3.3: SEM micrograph of graphite nanofibers in sample #5.

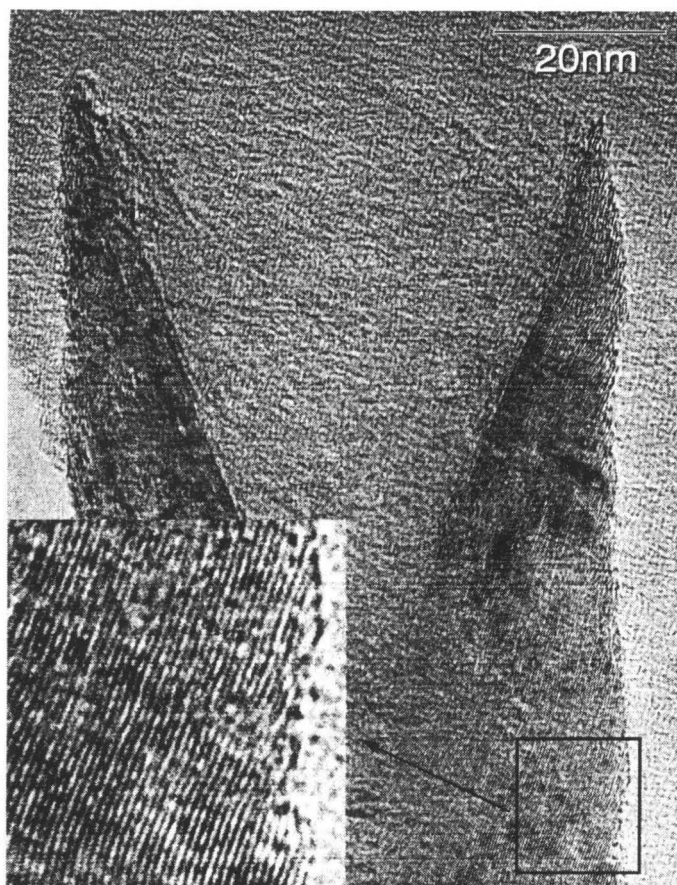


Figure 3.4: High resolution image from end of graphite nanofiber showing herringbone morphology. Inset at lower left shows lattice planes from boxed region.

using a Micromeritics ASAP 2000 BET surface analysis apparatus with N_2 gas.

3.5 Results

Table 3.2 summarizes the results of BET surface area measurements and hydrogen desorption data. For most samples, we did multiple runs on each data point to check the reproducibility of the results. Some isotherms are highly reproducible, as shown in Figure 3.9, since the hydrogen adsorption capacity is relatively high due to the high specific surface area of saran carbon and the low temperature. At the maximum pressure of 3 bar at 77 K, the hydrogen adsorption capacity of the saran carbon is 2.4 wt%. The desorption of H_2 in the graphite nanofiber samples is small but measurable.

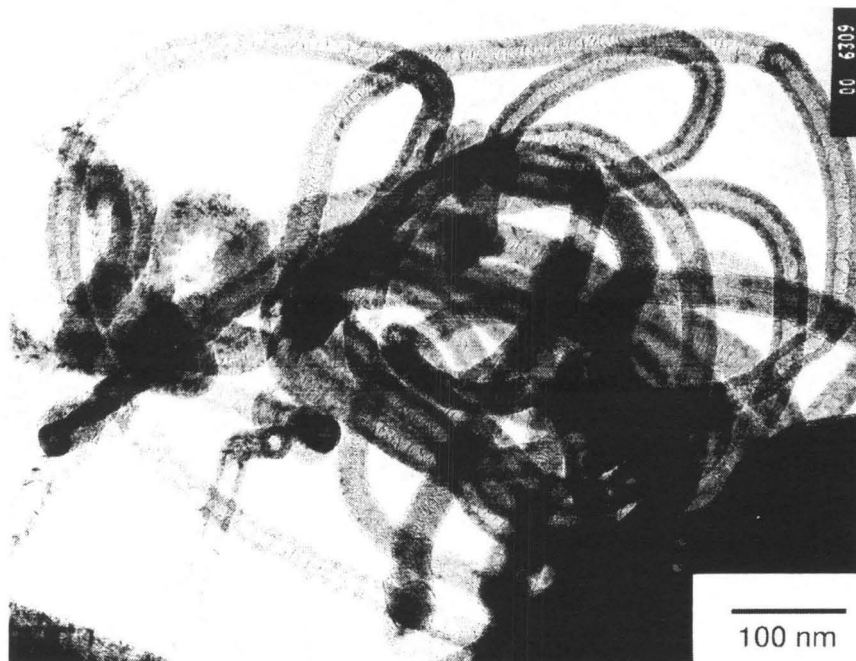


Figure 3.5: TEM micrograph of carbon nanotubes in GNF sample #5.

Figure 3.10 shows a set of runs of desorption isotherm for GNF sample #4 at room temperature. For the size of our samples, the sensitivity was better than 1% accuracy on a per atom basis. Results from five sets of runs from the saran carbon and sample #5 and #8 are shown in Figure 3.12.

Data of a high performance activated carbon denoted as AX-21 were obtained from the literature [10] and are included in Table 3.2 for comparison. AX-21 was commercially available and has a specific surface area of $3000 \text{ m}^2/\text{g}$ and pore volume of 1.5 mL/g .

3.6 Discussion

As measured on a per atom basis, our graphite nanofibers may seem to show adsorption beyond what one might expect from normal surface adsorption. When comparison is made to the saran carbon, the ratio of hydrogen coverage to surface area seems high for the graphite nanofibers. We would expect a change in slope of such an isotherm, but this was not observed. We believe this results from the presence

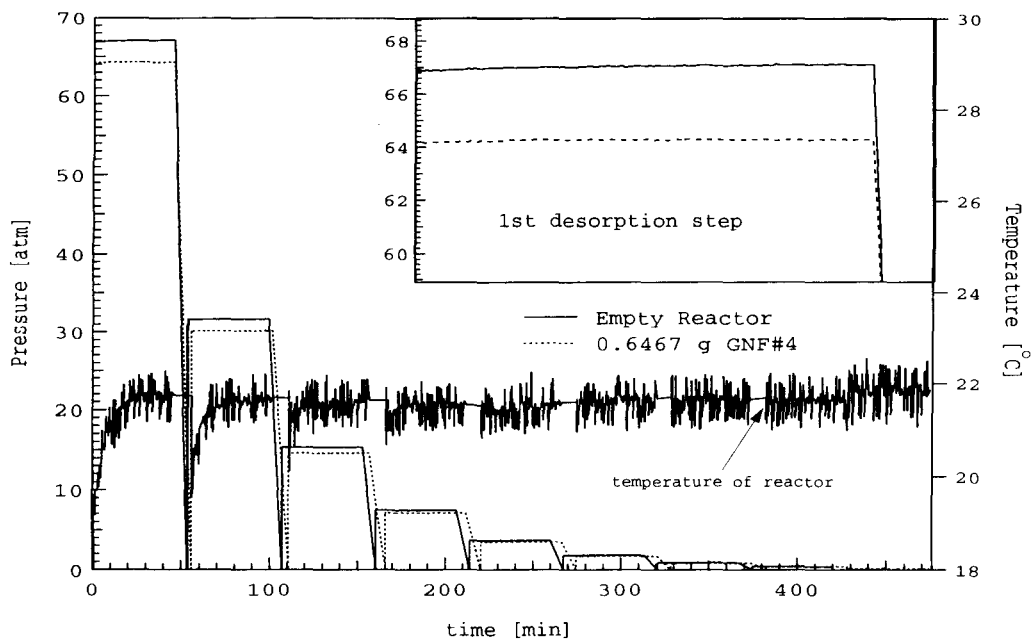


Figure 3.6: Raw data of desorption steps at room temperature.

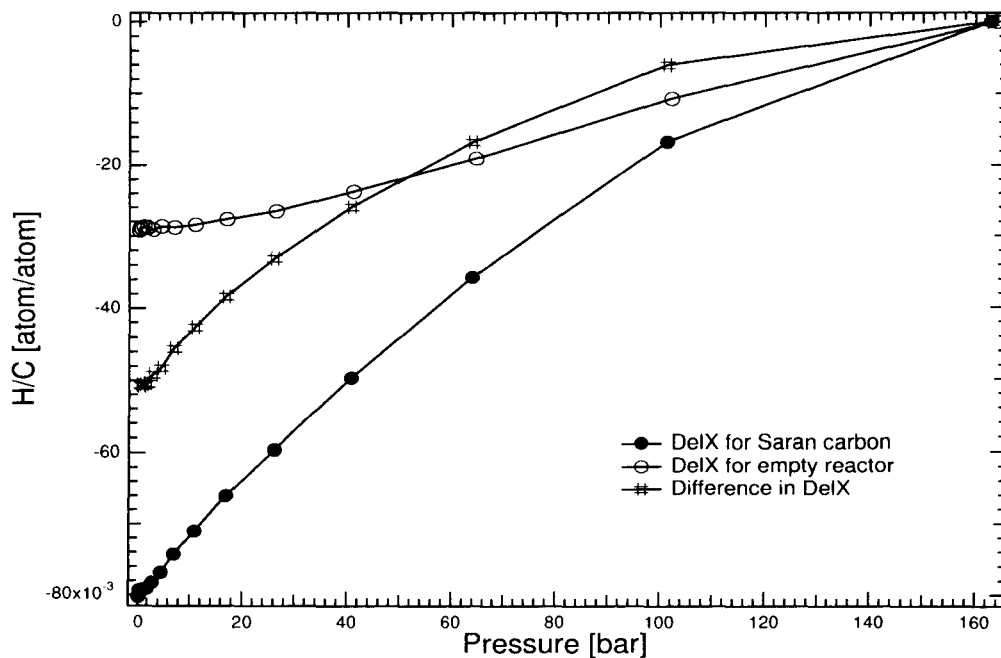


Figure 3.7: Calculated Δx (room temperature) for saran carbon sample and the empty reactor.

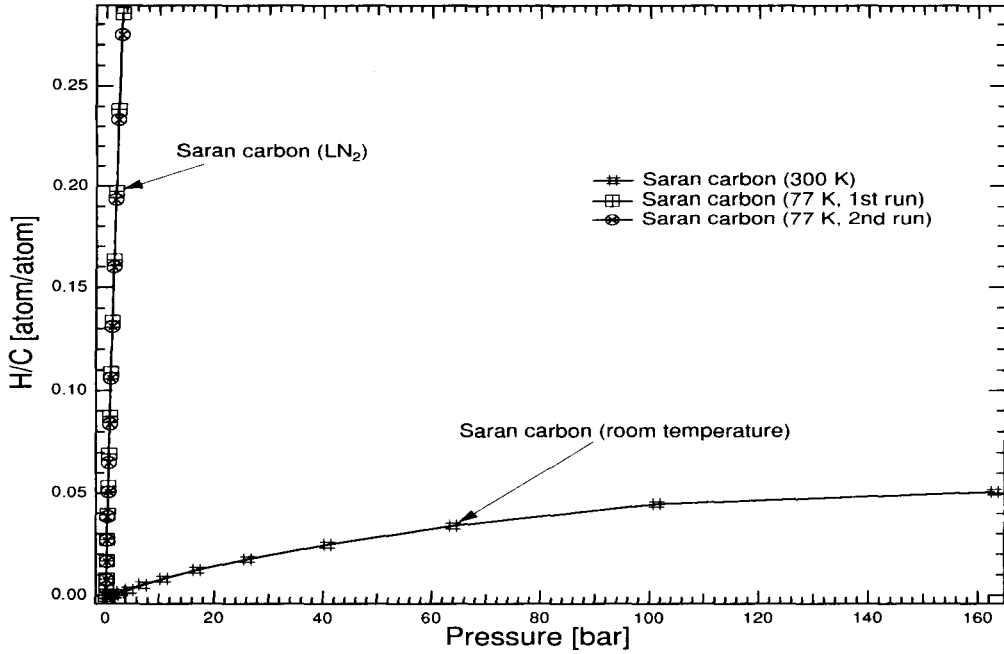


Figure 3.8: Desorption isotherms for saran carbon at room temperature and liquid nitrogen temperature (77 K).

Carbon Sample	Specific Area (m ² /g)	H/C (desorbed) @ 77 K, 4.5 bar	H/C (desorbed) @ 300 K, 160 bar	Hydrogen Coverage (m ² /g)
AX-21 data from [10]	3000	0.24	0.06 (70 bar)	150
Saran Carbon	1600	0.29 (3 bar)	0.05	130
GNF #4			0.023±0.003	55
GNF #5	25	0.02	0.03±0.003	80
GNF #7			0.029±0.003	75
GNF #8	23	—	0.025±0.005	70

Table 3.2: Comparison of surface area as measured by BET, desorbed atomic ratio of H to carbon, and total H₂ coverage assuming diameter of solid molecular H₂ of 0.351 nm[11].

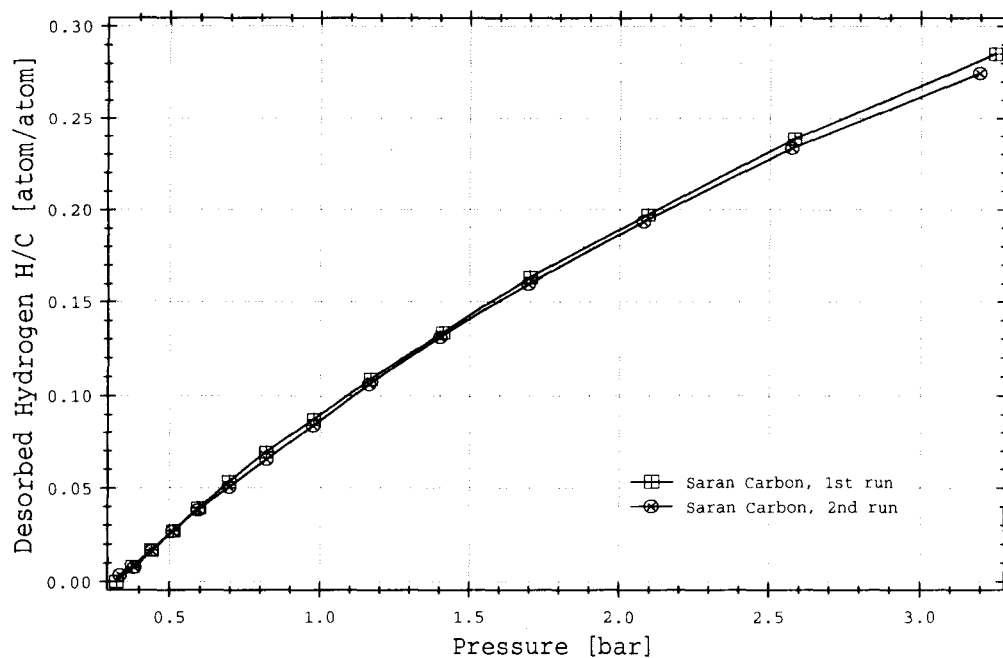


Figure 3.9: A set of runs of desorption isotherm for saran carbon sample at liquid nitrogen temperature.

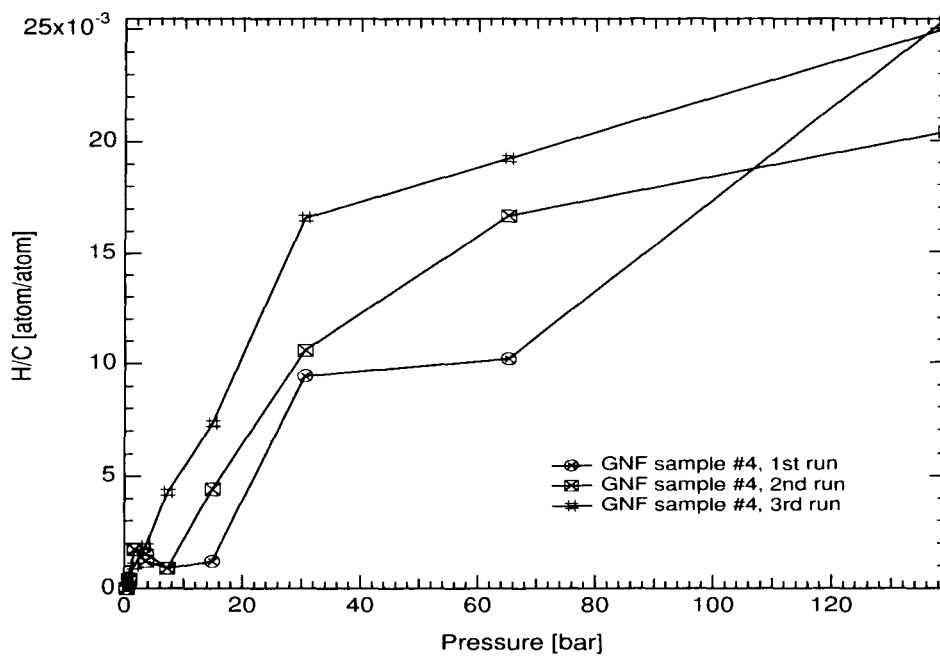


Figure 3.10: A set of runs of desorption isotherm for GNF sample #4 at room temperature.

of surface irregularities in the graphite nanofibers that are not detected by the larger N_2 molecules in our BET measurements. Support for this viewpoint is found in the shapes of the isotherms in Figure 3.12. At a given temperature the isotherms for the graphite nanofibers and the saran carbon have a similar shape, but a vertical offset. This difference by a scaling factor implies the same isosteric heat of adsorption for both types of carbons, but there are more available sites for the saran carbon.

None of the present hydrogen adsorption or desorption measurements performed on any of the carbon nanofiber materials has indicated a hydrogen storage capacity that exceed the values previously reported for various activated carbons [10, 12]. In light of our results, the results of Chambers, et al. [1] are especially surprising. Their claim of 2 gms of H_2 per gm of C storage imply that 16 H_2 molecules are stored in this material per C atom. If we assume that these H molecules are all stored within the graphite structure, then 48 monolayers of incommensurately packed H_2 must be accommodated between each pair of graphene planes (using a hard sphere model and a value of 0.289 nm kinetic diameter for H_2) in order to account for the reported adsorption. This amounts to each graphitic plane, with an a-b spacing of normally 0.34 nm, being separated to over 14 nm. Their data for H_2 adsorption in graphite of 4.5 wt% implies that even this material accommodates H_2 beyond the 2.7 wt% value that one would achieve with the commensurate $\sqrt{3}$ structure. Furthermore, their reported hydrogen capacity for graphite at room temperature is over an order of magnitude greater than the values determined by others [10, 12] for activated carbons at 298 K. The best of these carbons yielded H_2 adsorption in the range of ~ 5 wt% only when cooled to below 100 K.

3.7 Conclusions

As a result of our analysis, it seems unlikely that carbon in nanofiber form shows H_2 adsorption/desorption properties that would have the spectacular impact as a solid state storage medium claimed by Chambers, et al [1]. A more realistic analysis of the limits of physisorption of hydrogen in graphite is considered by Brown, et al

[13], who forward arguments on the basis of geometry to show the likely upper limits of adsorption in various forms of carbon. They note that under conditions where H_2 molecules are able to form two closed packed layers within each graphite plane, the atomic ratio of H:C approaches 1:1 (~ 8 wt%).

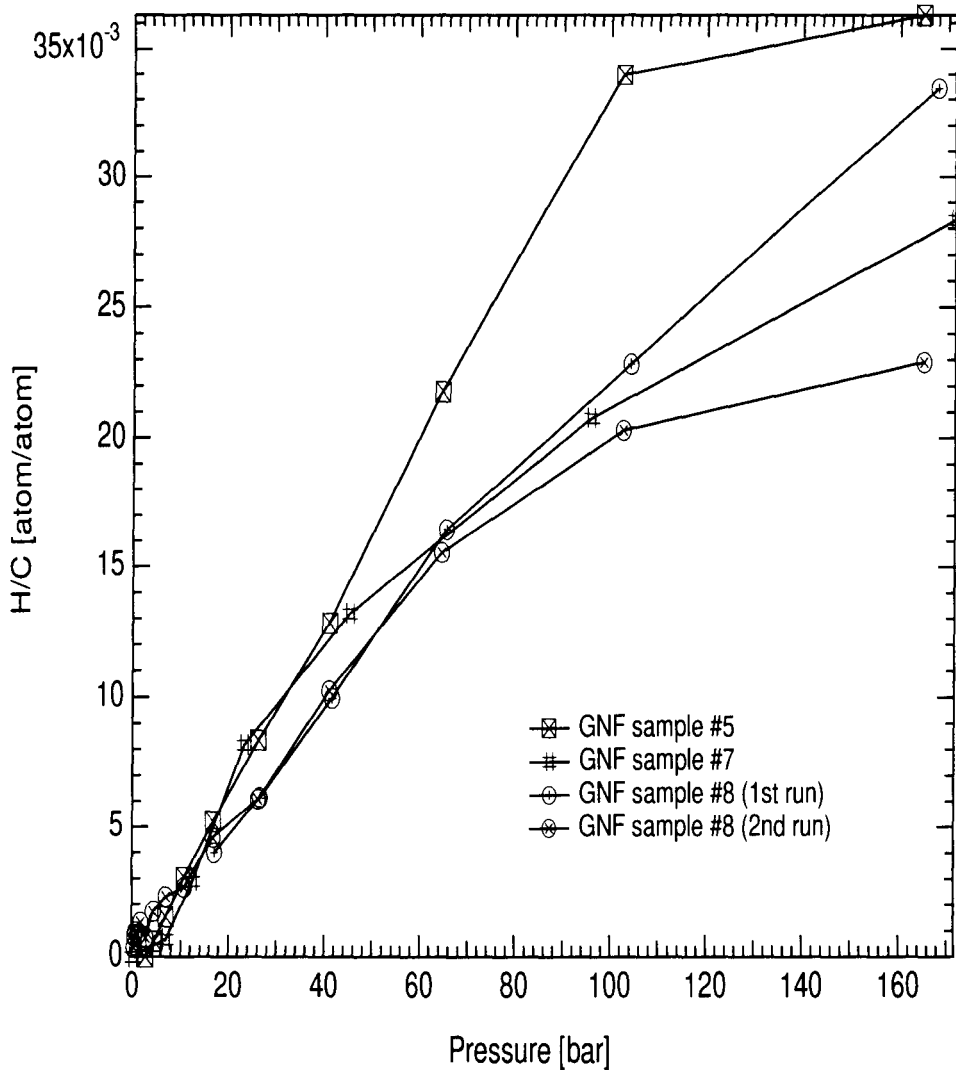


Figure 3.11: Desorption isotherms for GNF sample #5, #7, and #8 at room temperature.

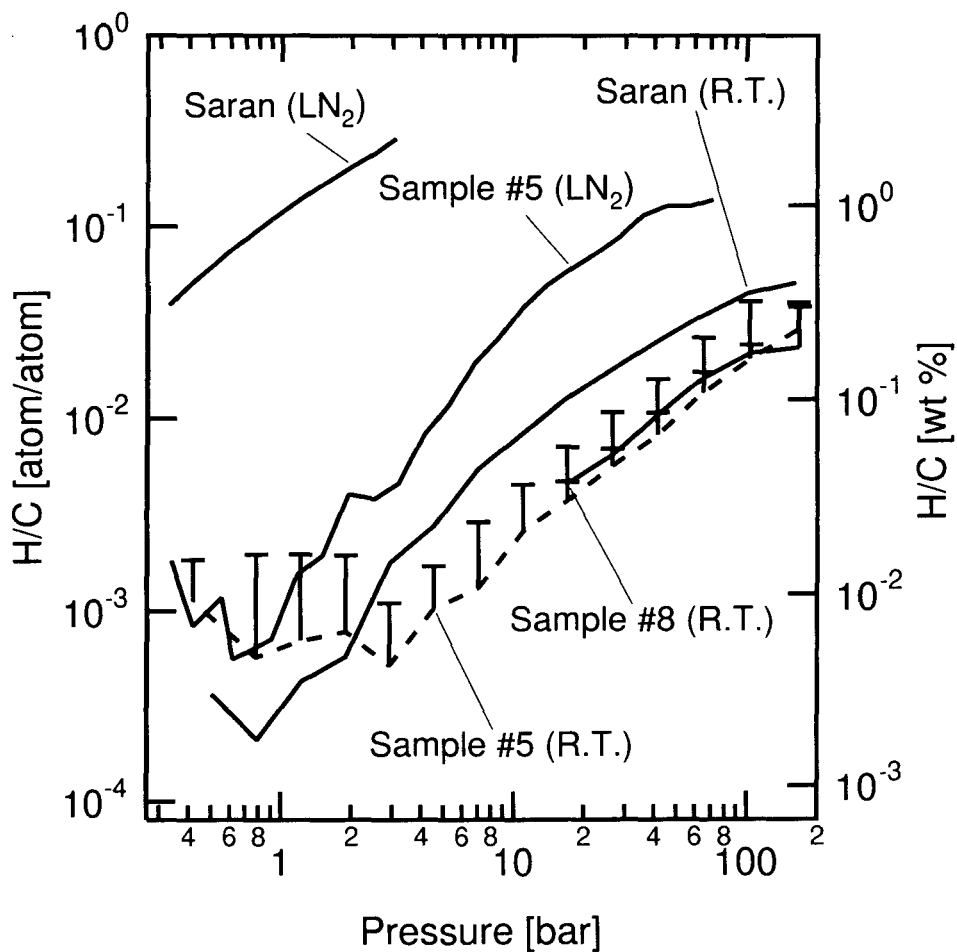


Figure 3.12: Log-log plot of 77 and 300 K isotherm data showing amount of adsorbed hydrogen/carbon for GNF sample #5 and #8, as a function of pressure. When multiple runs were taken, error bars are shown, with only the top half of the error bars drawn for clarity. Traces from saran carbon are also shown for comparison.

Bibliography

- [1] A. Chambers, C. Park, R. T. K. Baker, and N. M. Rodriguez, *J. Phys. Chem. B*, **102**, 4253 (1998).
- [2] N. M. Rodriguez and R. T. K. Baker, "Storage of Hydrogen in Layered Nanostructures," U. S. Patent #5,653,951, Issued Aug. 5, 1997.
- [3] A. C. Dillon, K. M. Jones, T. A. Bekkedahl, C. H. Kiang, D. S. Bethune, and M. J. Heben, *Nature (London)*, **386**, 377 (1997).
- [4] N. M. Rodriguez, *J. Mater. Res.*, **8**, 3233 (1993).
- [5] N. M. Rodriguez, A. Chambers, and R. T. K. Baker, *Langmuir*, **11**, 3862 (1995).
- [6] B. Fultz, C. C. Ahn, S. Spooner, L. B. Hong, J. Eckert, and W. L. Johnson, *Metall. Trans.*, **27A**, 2934 (1996).
- [7] B. Fultz, C. C. Ahn, E. E. Alp, W. Sturhahn, and T. S. Toellner, *Phys. Rev. Lett.*, **79**, 937 (1997).
- [8] R. C. Bowman, Jr., C. H. Luo, C. C. Ahn, C. K. Witham, and B. Fultz, *J. Alloys Comp.*, **217**, 185 (1995).
- [9] R. A. Wessling, Polyvinylidene Chloride, Gordon & Breach, New York, 1977.
- [10] Y. Zhou and L. Zhou, *Sci. in China* **B39**, 598 (1996).
- [11] M. Nielsen, J. P. McTague, and W. Ellenson, *J. Phys.*, **38** C4/10-C4/18 (1977).
- [12] R. Chahine and T. K. Bose, *Int. J. Hydrogen Energy*, **19**, 161 (1994).
- [13] S. D. M. Brown, G. Dresselhaus, and M. S. Dresselhaus, *Mat. Res. Soc. Proc.*, **497**, 157 (1998).

Chapter 4 Hydrogen Adsorption and Cohesive Energy of Single-Walled Carbon Nanotubes

4.1 Background

A few years after the report of the C_{60} molecule by Kroto, et al. [1], Iijima discovered the tubular form of carbon [2]. Single-walled nanotubes (SWNT's) are the simplest of these structures, being but a single graphite plane rolled into a thin tube [3, 4]. Methods for the synthesis of SWNT's do not produce a monodisperse product, and the large scale purification of SWNT's has been achieved only recently [5]. The cohesion of these molecular crystals occurs through van der Waals interactions and perhaps other effects of electron correlation [6, 7, 8, 9], and it is widely observed that the individual SWNT's coalesce into rope-like strands [10]. Many properties of condensed SWNT's are now topics of intensive study; however, the strength of the cohesive energy of crystalline SWNT's remains poorly understood.

There is a recent report that crystalline SWNT's have a capacity for hydrogen sorption of 5-10 wt.% at pressures less than 1 bar near room temperature [11]. Such a hydrogen storage capacity would be a significant advance for the use of hydrogen as a fuel when a high gravimetric density of hydrogen is a figure of merit. Until recently, the best value of hydrogen adsorption in carbon materials has been 5.3 wt.%, or 0.64 H/C, at a temperature of 77 K [12, 13]. (A recent claim that graphite nanofibers have a capacity of 24 H/C at 300 K [14] has not been corroborated [15].) We were motivated to perform measurements SWNT material of high purity because the previous measurements were made on dilute SWNT's, so the analysis required a large correction for more than 99% of material that was assumed inert [11].

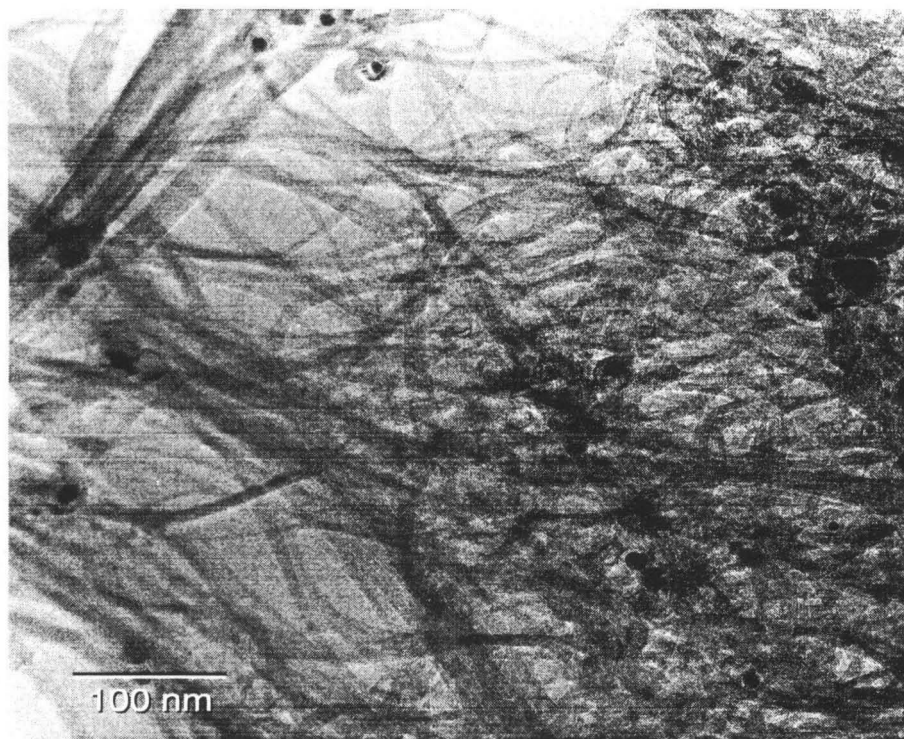


Figure 4.1: A low resolution transmission electron micrograph of the SWNT materials, showing the rope structure.

4.2 Experiments

Three batches of nanotube material were prepared [16] and purified [5, 10]. To cut the SWNT's, about 0.2 g of material was sonicated for 10 h in dimethyl formamide at a concentration of 0.1 mg/ml until the sample was completely suspended in the solvent [17]. The modified SWNT material was then extracted by vacuum filtration using a ceramic filter.

Desorption and some adsorption isotherms were measured on samples of approximately 200 mg with a computer controlled Sieverts' apparatus. After vacuum degassing at 220°C for 10 h, the measurement temperature was attained and hydrogen gas of 99.9999% purity was admitted into the reactor to a desired maximum pressure (160 bar at 300 K, and 130, 70, 4.5 or 0.5 bar at 80 K). This pressure was maintained for 15 h to allow the adsorption to equilibrate and to check for leaks in the system. The amount of hydrogen desorbed from the sample was determined in steps by mea-

suring the pressure on the sample before and after the sample reactor was opened to an evacuated reference volume. To correct for instrumental effects, we performed identical measurements on an empty reactor after each sample measurement. Surface area was measured with a Micromeritics ASAP 2000 BET surface analysis instrument using nitrogen gas. The surface areas of the as-prepared SWNT material, the material after isotherm measurement, and the material after sonication, were found to be 285 ± 5 m²/g. Phase contrast transmission electron microscopy was performed with a Philips EM430 transmission electron microscope operated at 200 kV. X-ray powder diffractometry was performed using Co K α radiation with an Inel CPS-120 position sensitive detector.

4.3 Isotherm Results and Cohesive Energy Calculation

Transmission electron microscopy of the as-prepared material showed dense bundles, or “ropes” of crystallized SWNT’s. The rope diameters varied from 6-12 nm. The high resolution image (Figure 4.2) shows circular rings of approximately 1.3 nm in diameter, consistent with the dominant (10,10) SWNT structure. With hexagonal tube coordination, a rope of 10 nm diameter would contain about 50 tubes, and would be 8 times the diameter of a single tube. The specific surface area of a rope would be about 6 times less than the outer surface area of a single tube (1300 m²/g). The surface area measured by BET (285 m²/g) is evidently a measure of the outer surface area of the ropes, not the total surface area of the individual tubes. The ropes perpendicular to the electron beam showed a number of sets of internal fringe spacings of 0.34 nm. Fringe terminations were observed within the ropes, indicative of misalignments or terminations of individual tubes. The rope diameters of the sonicated material were comparable, but with a broader size distribution. The sonicated material showed a more irregular patchwork of fringes, presumably because of more terminations of individual SWNT’s in the ropes. On the other hand, it can

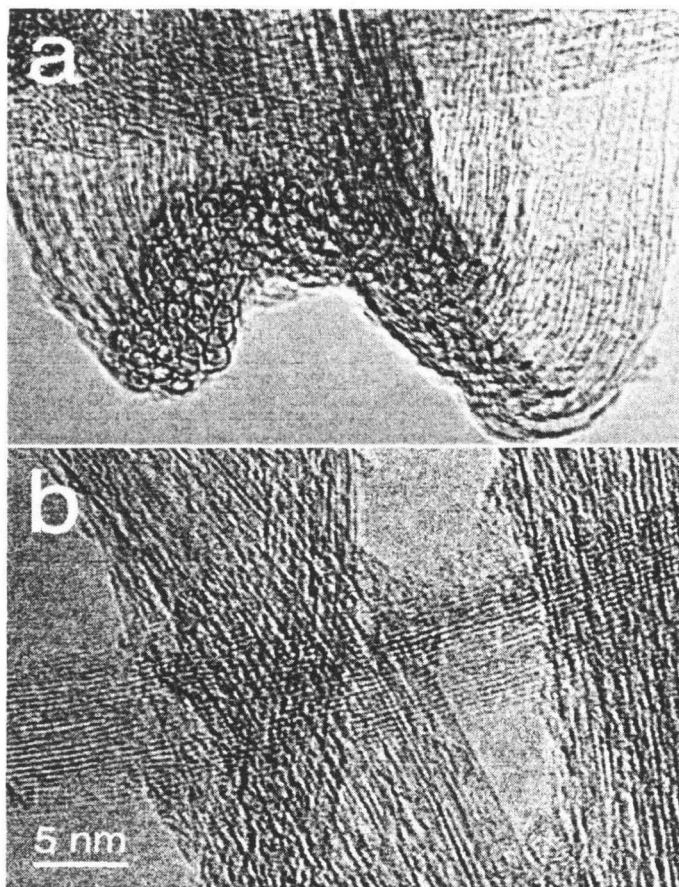


Figure 4.2: High resolution transmission electron micrographs of the SWNT materials. (a) as-prepared, showing cross sections of tubes towards lower center, and (b) after sonication in dimethyl formamide.

be seen from Figure 4.3, X-ray diffractometry showed no significant differences after sonication.

For SWNT's ($285 \text{ m}^2/\text{g}$), and high surface area saran carbon ($1600 \text{ m}^2/\text{g}$) [18], the hydrogen adsorptions (ratio of H atoms/C atoms) obtained at 3.2 bar at 80 K were 0.040, and 0.28, respectively. These results show the expected proportionality between surface area as measured by BET and the hydrogen adsorption, as did the hydrogen adsorptions at 160 bar at 300 K. The low pressure composition-pressure isotherms at 80 K and the high pressure isotherms at 300 K had similar shapes for all carbons. They were described adequately with the Langmuir adsorption isotherm,

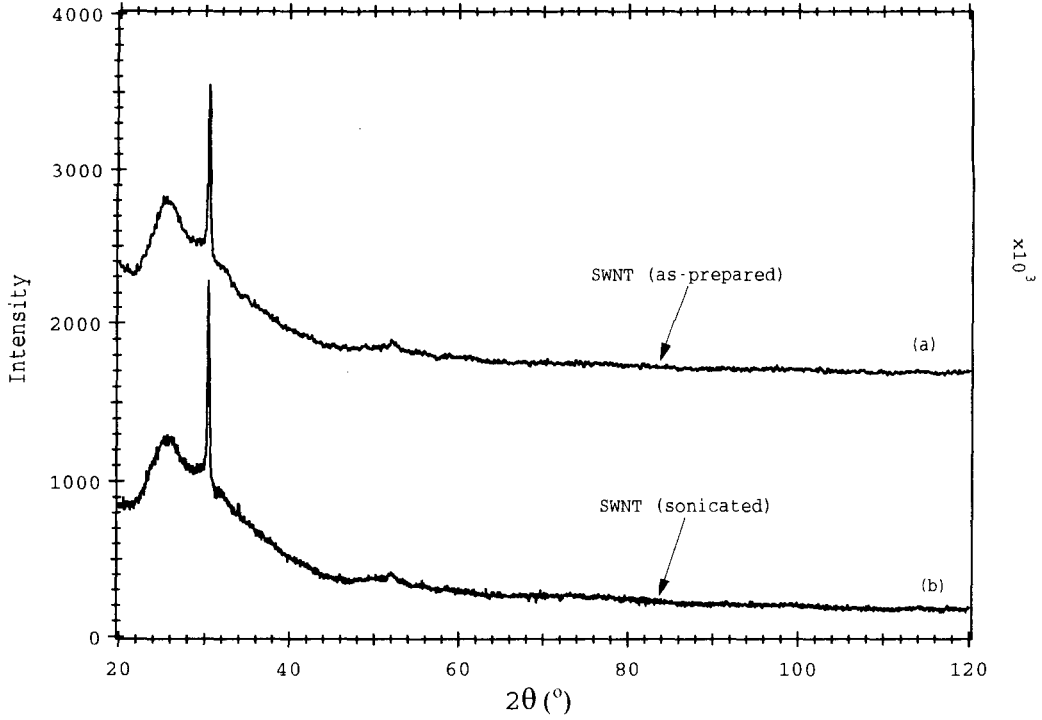


Figure 4.3: X-ray diffraction pattern of single-walled materials (a) as-prepared and (b) after sonication in dimethyl formamide.

for which the fractional coverage, f , is:

$$f = \frac{1}{e^{(\varepsilon - \mu)/kT} + 1} \quad (4.1)$$

The chemical potential of a hydrogen molecule in the gas is μ , and its energy of adsorption is ε ($\varepsilon < 0$). Using a tabulated function for chemical potential versus pressure [19] (Figure 4.4), we fit the saran carbon isotherm with f . At low coverage we found $\varepsilon = 38$ meV, in excellent agreement with the results of Pace and Siebert [21]. The isotherm of the saran carbon material in Figure 4.5 is similar in shape to isotherms from other carbons of high surface area at 80 K [12, 13, 22].

Equation 4.1 can be written conveniently in terms of the gas pressure [20]

$$f = \frac{P}{P_0 + P} \quad (4.2)$$

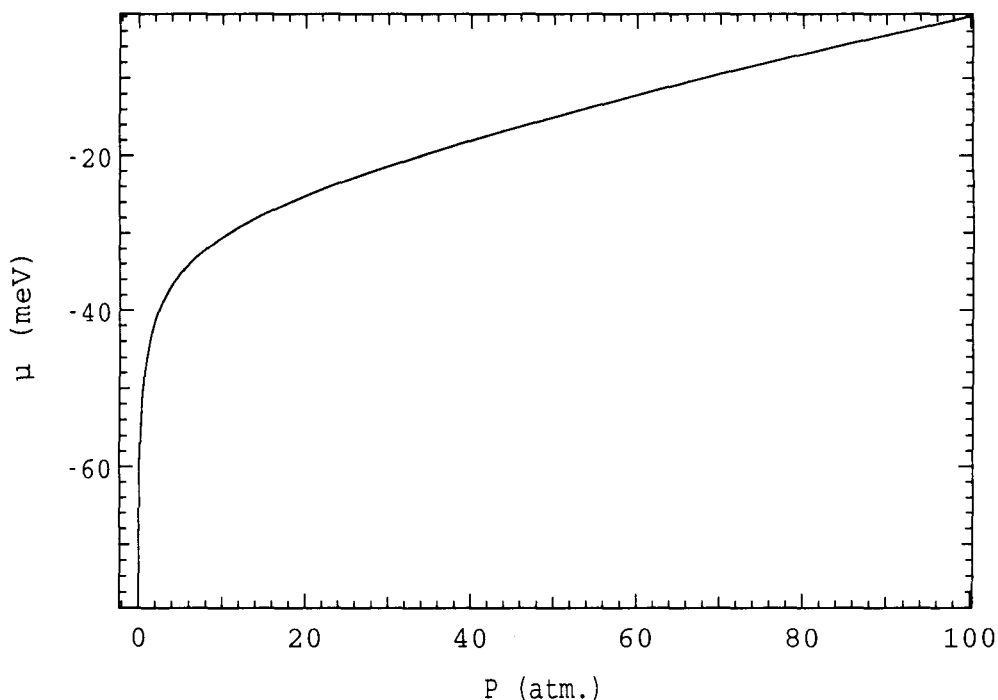


Figure 4.4: Chemical potential of hydrogen gas at 77 K.

For hydrogen on graphite at 300 K, $P_o \sim 4$ bar. Equation 4.2 shows that a smaller P_o is expected at lower temperatures. At 80 K, $P_o \sim 1$ bar, and adsorption occurs at lower pressures of hydrogen. This is evident for the isotherm of the saran carbon material in Figure 4.5, and this is described well by Equation 4.1.

Also shown in Figure 4.5 is an adsorption curve calculated from the saran carbon data by reducing it in proportion to the lower surface area of the SWNT material as measured by BET. This curve, scaled by the factor 285/1600, accounts approximately for the adsorption of the SWNT material (labeled “SWNT” in Figure 4.5) at low pressures, but fails at pressures greater than about 20 bar.

At high hydrogen pressures at 80 K, the curves labeled “SWNT” in Figure 4.5 show a ratio of hydrogen to carbon atoms of about 1.0 (8.25 wt.%), and suggest that higher concentrations may occur at pressures beyond our experimental capabilities. To our knowledge, this is the highest hydrogen storage capacity yet measured on an activated carbon material. (A coke material processed with KOH, denoted “AX-21,”

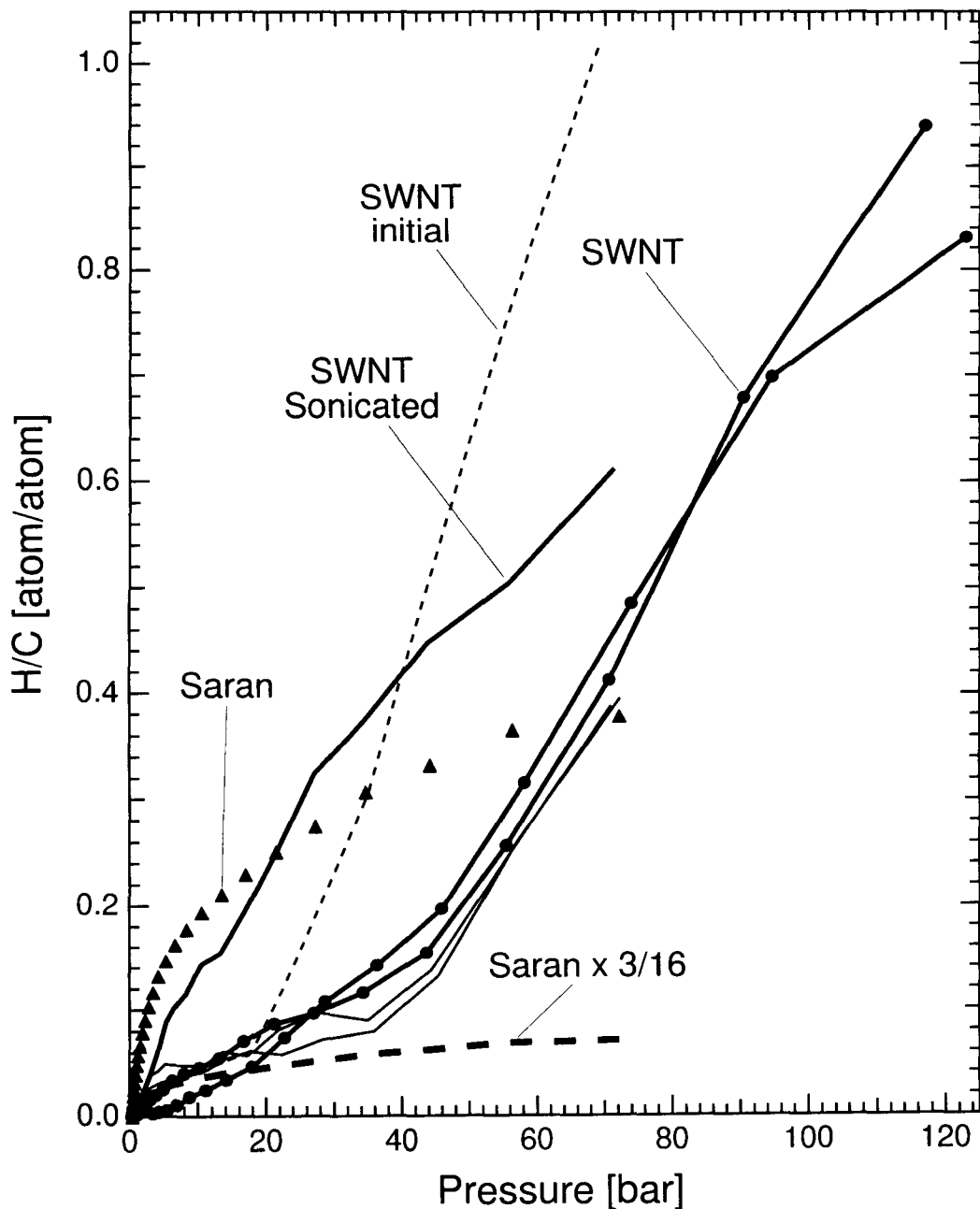


Figure 4.5: Isotherms of composition versus pressure at 80 K for samples of as-prepared SWNT material, the SWNT material after sonication in dimethyl formamide, and a high surface area saran carbon. Adjacent pairs of curves (labeled "SWNT") were sequential runs on the same sample. Also shown is the curve of the saran carbon scaled to lower H/C ratio by the surface area ratio of 285/1600.

reaches a peak 0.64 H/C at 77 K at an optimal pressure of 30 bar [12, 13].) Our results are inconsistent with the report of Dillon, et al., that such capacities are attained at 300 K and pressures well below 1 bar [11]. The kink at 40 bar and the steep slope of the hydrogen adsorption isotherm of the SWNT material at pressures from 40 to 100 bar is unique for hydrogen adsorption on a carbon material. This shape can not be obtained from a sum of concave-downwards isotherms such as f , even with a distribution of adsorption energies, ε . The shape of the SWNT isotherm is similar to isotherms of metal-hydrogen systems which form a hydride phase by a first-order phase transition [23], although the mechanism of hydrogen absorption is certainly different.

The low pressure adsorption of hydrogen on SWNT material saturates like that of the saran carbon, scaled by the surface area of the ropes. At pressures above 40 bar, however, the isotherms indicate that the SWNT material undergoes a transition to a new state of hydrogen coverage. From the large H/C ratio at high pressures, we deduce that the surface area increases by about an order of magnitude. This is consistent with the hydrogen permeating into the ropes, separating them into individual SWNT's with full exposure of their outer and possibly inner surfaces, and physisorbing onto the carbon surfaces. This high density phase must involve tube decohesion, since the hydrogen coverage is high and the attractive van der Waals and exchange forces are attenuated when the tubes are separated by short distances. The thermodynamic driving force for this tube decohesion is the high chemical potential of the hydrogen gas at high pressure. The hydrogen molecules that adsorb on the surface of the SWNT's undergo a decrease in chemical potential. The equality of chemical potential in two-phase equilibrium requires the reduction of chemical potential of hydrogen gas in the high capacity phase to be equal to the loss of van der Waals cohesive energy [24].

The data of Figure 4.5 indicate an average pressure of 70 bar for the phase transition, which corresponds to a chemical potential of -11 meV per hydrogen molecule [19]. This should be compared to the characteristic chemical potential for hydrogen physisorption of -38 meV, corresponding to a decrease in chemical potential upon

adsorption, $\Delta\mu$, of 27 meV per hydrogen molecule. This $\Delta\mu$ can be used to determine the cohesive energy of the SWNT's in a rope. When the adsorbed hydrogen molecules are commensurate with the carbon atoms on a graphene plane, the composition would be C_3H on one surface of the plane [25, 26]. For the measured surface area of the saran carbon of 1600 m²/g, this structure would provide H/C=0.40, in good agreement with the saran carbon isotherm at about 70 bar. Using this same hydrogen coverage for the SWNT material at 70 bar, the $\Delta\mu$ of 27 meV/H₂ or (13.5 meV/H) provides a cohesive energy for the SWNT's in a rope of 4.5 meV/C atom. An alternative estimate can be made by noting that the characteristic midpoint of the phase transition corresponds to a composition of H/C=0.43 at 70 bar, which provides a cohesive energy of 6 meV/C atom.

The slope of the SWNT isotherm in Figure 4.5 is not infinite, probably because there is a distribution of cohesive energies in the material. To obtain an upper limit on cohesive energy, we note that some of the tubes separate at pressures of 100 bar at a macroscopic H/C=0.8. This corresponds to a cohesive energy of 14 meV/C atom for a minority of the material. Some of the change in H/C at higher pressures could be caused by additional coverage on tubes that had separated at lower pressures, however. Allowing for such a change in coverage in the majority of the material will reduce this upper limit, perhaps considerably.

4.4 Discussion

Our experimental value for the cohesive energy, 5 meV for much of the material, is smaller than the 17 meV/C atom calculated by Tersoff [7], the 35 meV/C atom calculated by Benedict, et al., for large tubes with flat area of contact [9], or the 22 meV/C atom calculated by Cagin and Goddard [27].

We are not surprised to see this reduction in cohesive energy. The van der Waals interaction and other electron-electron correlation effects are especially sensitive to distance. We can account for small reductions in cohesive energy with features of the rope morphology observed by TEM.

Surface energy is one contribution. We assume the number of neighbors will be reduced from 6 to 3 for the tubes at the surface of the ropes. Within a rope with a radius of 6 tubes, the average number of first-nearest neighbors of tube will be reduced from 6 to 5, so the cohesive energy will be $5/6$ of its value for a large crystal. This means that the reduced coordination at the rope surfaces will reduce the cohesive energy by only about 15%.

The elastic energy of tube curvature will be another contribution. Figure 4.2 shows significant curvature of the ropes, which provide for typical maximum strains in the tube walls of 0.5% or so. However, with a calculated elastic modulus [28], we obtained a typical maximum elastic energy of less than 0.5 meV per atom in the tubes. Thus the elastic energy of the observed tube curvature is small and does not dominate the cohesive energy.

Since there is a rapid reduction with distance of the van der Waals interaction and other electron-electron correlation effects responsible for SWNT cohesion, defects in the close-packed triangular lattice of SWNT's should cause a large reduction in the cohesive energy. The cohesive energy of SWNT crystals is expected to be reduced when the inter-tube distances are disrupted by tube terminations, misalignments, and dislocations within the crystalline rope.

The following experimental evidence indicates that these defects cause a large change in cohesive energy. The curve labeled "SWNT initial" in Figure 4.5 was a first run on a fresh sample, and first runs on two other samples exhibited such high reversible adsorption at lower pressures. All second and subsequent desorptions occurred at higher pressures, as shown in Figure 4.5 for the group of four curves labeled "SWNT." We believe that the first adsorption/desorption cycle caused the SWNT's to reorganize in structure, perhaps into a more perfect triangular lattice, causing subsequent desorptions at higher pressures. More convincing are the data on the sonicated material. The pressures of desorption for this material show a considerable breadth, indicating a distribution of cohesive energies of the tubes. Furthermore, for all hydrogen concentrations, the pressures for the sonicated material are suppressed with respect to the as-prepared samples. A reduction in pressure is consistent with

additional defects in the crystalline ropes of sonicated material causing a reduction in the cohesive energy of the rope structure.

Finally, we note that the first order phase transition causes the SWNT's to adsorb and desorb over a narrower range of pressures, overcoming an engineering challenge for hydrogen storage systems [22].

4.5 Conclusion

A phase transition between crystal SWNT and a new hydride phase was found at high pressures at 80K. The phase transition was of first order, and involved the separation of the individual tubes within a rope, exposing a high surface area for hydrogen adsorption. From the change in chemical potential of the hydrogen gas upon adsorption, we were able to calculate the cohesive van der Waals energy between the tubes as 5 meV/C atom. This is much smaller than expected from previous theoretical work, and shows that defects in the crystal structure cause large suppressions of the cohesive energy. We were able to alter this cohesive energy by changing the state of the material.

Bibliography

- [1] H. W. Kroto, J. R. Heath, S. C. O'Brien, R. F. Curl, and R. E. Smalley, *Nature*, **318**, 162 (1985).
- [2] S. Iijima, *Nature (London)*, **354**, 603 (1991).
- [3] S. Iijima and T. Ichihashi, *Nature*, **363**, 603 (1993).
- [4] D. S. Bethune, C. H. Kiang, M. S. Devries, G. Gorman, R. Savoy, J. Vazquez, and R. Beyers, *Nature (London)*, **363**, 605 (1993).
- [5] A. G. Rinzler, J. Liu, H. Dai, P. Nikolaev, C. B. Huffman, F. J. Rodriguez-Macias, P. J. Boul, A. H. Lu, D. Heymann, D. T. Colbert, R. S. Lee, J. E. Fischer, A. M. Rao, P. C. Eklund, and R. E. Smalley, *Appl. Phys.*, **A67**, 29 (1998).
- [6] R. S. Ruoff, J. Tersoff, D. C. Lorents, S. Subramoney, and B. Chan, *Nature (London)*, **364**, 514 (1993).
- [7] J. Tersoff and R. S. Ruoff, *Phys. Rev. Lett.*, **73**, 676 (1994).
- [8] S. N. Song, X. K. Wang, R. P. H. Chang, and J. B. Ketterson, et al., *Phys. Rev. Lett.*, **72**, 697 (1994).
- [9] L. X. Benedict, N. G. Chopra, M. L. Cohen, A. Zettl, S. G. Louie and V. H. Crespi, *Chem. Phys. Lett.*, **286**, 490 (1998).
- [10] J. Liu, A. G. Rinzler, H. Dai, J. H. Hafner, R. K. Bradley, P. J. Boul, A. Lu, T. Iverson, K. Shelimov, C. B. Huffman, F. Rodriguez-Macias, Y-S. Shon, T. R. Lee, D. T. Colbert, and R. E. Smalley, *Science*, **280**, 1253 (1998).
- [11] A. C. Dillon, K. M. Jones, T. A. Bekkedahl, C. H. Kiang, D. S. Bethune, and M. J. Heben, *Nature (London)*, **386**, 377 (1997).

- [12] R. Chahine and T. K. Bose, *Int. J. Hydrogen Energy*, **19**, 161 (1994).
- [13] Z. Yaping and A. Li, *Science in China*, **B 39**, 598 (1996).
- [14] A. Chambers, C. Park, R. T. K. Baker, and N. M. Rodriguez, *J. Phys. Chem.***B** **102**, 4253 (1998).
- [15] C. C. Ahn, Y. Ye, B. V. Ratnakumar, C. Witham, R. C. Bowman, Jr., and B. Fultz, *Appl. Phys. Lett.*, **73**, 3378 (1998).
- [16] A. Thess, R. Lee, P. Nikolaev, H. Hai, P. Petit, J. Robert, C. Xu, Y. H. Lee, S. G. Kim, A. G. Rinzler, D. T. Colbert, G. E. Scuseria, D. Tomanek, J. E. Fischer, and R. E. Smalley, *Science*, **273**, 483 (1996).
- [17] J. Liu, unpublished results.
- [18] Saran carbon is a pure, dense, porous material with high surface area, formed by the pyrolysis of polyvinylidene chloride.
- [19] R. D. McCarty, J. Hord, and H. M. Roder, "Selected Properties of Hydrogen" NBS Monograph 168 (US Government Printing Office, Washington, D.C., 1981) pp. 6-130 - 6-269. W. E. Forsythe, editor, *Smithsonian Physical Tables* 9th ed. (Smithsonian Institute, Washington, 1964).
- [20] C. Kittel, Introduction to Solid State Physics, 7th edition, John Wiley & Sons, Inc. New York (1996).
- [21] E. L. Pace and A. R. Siebert, *J. Phys. Chem.*, **63**, 1398 (1959).
- [22] S. Hynek, W. Fuller, and J. Bentley, *Int. J. Hydrogen Energy*, **22**, 601 (1997).
- [23] L. Schlapbach, in Hydrogen in Intermetallic Compounds I, L. Schlapbach, ed., Springer-Verlag, Heidelberg, 1988, p 1.
- [24] We assume that the enthalpy of adsorption for a hydrogen molecule on a curved SWNT is the same as on flat graphite. The shape of the SWNT isotherm at low

pressures is nearly the same as that of high surface area carbons, supporting this assumption. We also ignore the entropy gained during the separation of the tubes because this will be small on a per atom basis.

- [25] M. Nielsen, J. P. McTague, and W. Ellenson, *J. de Physique*, **38**, C4-10 (1977).
- [26] H. Freimuth, H. Wiechert, H. P. Schindberg, and J. J. Lauter, *Phys. Rev.*, **B 42**, 587 (1990).
- [27] T. Cagin and W. A. Goddard, III, unpublished material.
- [28] G. Gao, T. Cagin, and W. A. Goddard, III, *Nanotechnology*, **9**, 183 (1998).

Chapter 5 Hydrogen Adsorption and Phase Transitions in Fullerites

Hydrogen desorption and adsorption properties of fullerene materials C_{60} , and C_{70} and fullerite (a mixture of C_{60} and C_{70}) were measured volumetrically using a Sievert's apparatus. Over several cycles of isotherm measurements at 77 K, the hydrogen storage capacities of one of the fullerite samples increased from an initial value of 0.4 wt% for the first cycle to a capacity of 4.2 wt% for the fourth cycle. Correspondingly, the surface area increased from 0.9 m²/gm to 11 m²/gm, and showed a phase transformation, characterized by X-ray powder diffraction. In comparison, two other fullerite samples, prepared by a different procedure, showed no such behavior. Pure C_{60} and pure C_{70} were cycled and exhibited small and constant capacities of 0.7 wt% and 0.33 wt%, respectively, as a function of number of cycles. The enhanced storage capacity of fullerite material is tentatively attributed to the presence of C_{60} oxide.

5.1 Background

Crystalline fcc C_{60} has been observed to absorb H_2 in octahedral interstices, providing a storage capacity of only 0.28 wt% at 50°C [1].

In this chapter, I present the results of studies on physisorption of H_2 into fullerenes. In the fullerene family, the closed cage nearly spherical C_{60} and the ellipsoidal rugby-ball-shaped C_{70} are the most stable molecules [2, 3], and thus show high relative abundance. We performed measurements on pure C_{60} , pure C_{70} and two sets of a mixture of these two commonly referred to as "fullerite." We report a surprising increase in the amount of H_2 that fullerite adsorbs and desorbs after a few cycles.

5.2 Experiments

Several different commercially available fullerene samples were obtained from Alfa Aesar and MER Corp. All these fullerenes were made by a carbon arc discharge in helium (Krätshmer-Huffman method). The carbon soot was then treated in toluene. The fullerite is soluble in toluene at the limit of 2 gm/liter and for the first fullerite sample (denoted fullerite #1) from MER Corp., and obtained in 1992. The solution was then spread onto a Teflon tray and evaporated at room temperatures. For the second fullerite sample from Alfa Aesar (denoted fullerite #2) and obtained in 1999, the precipitate from the toluene solution was obtained after slow evaporation of the toluene. The precipitate was then washed with petroleum ether and underwent drying to remove the rest of the solvent. A third sample of fullerite was obtained from MER in 1999 (denoted as fullerite #3) and was processed similarly to fullerite #2. All fullerite samples typically contained about 72-75% C₆₀, 22% C₇₀ and 1-3% higher fullerene molecules. The pure C₆₀ (or C₇₀) fullerenes were obtained by chromatographic methods, and the purity was 99.9% for C₆₀ and ~98% for C₇₀.

Desorption and some adsorption isotherms were measured on samples of 600 mg with a computer-controlled Sieverts' apparatus at 300 K and 77 K. After vacuum degassing at 200°C for 10 h, the measurement temperature was attained and hydrogen gas of 99.9999% purity was admitted into the reactor to a maximum pressure of about 120 bar. This pressure was maintained for 15 h to allow the adsorption to equilibrate and to check for leaks in the system. To correct for instrumental effects, we performed identical volumetric measurements on an empty reactor after each sample measurement. This procedure was used for every adsorption/desorption cycle, when multiple cycles were taken on the identical sample.

Surface area was measured with a Micromeritics ASAP 2000 BET surface area analysis instrument using nitrogen gas. Phase contrast transmission electron microscopy was performed with a Philips EM430 transmission electron microscope operated at 200 kV. X-ray powder diffractometry was performed on samples, both as-received and after-cycling, using an Inel CPS-120 powder diffractometer using Co

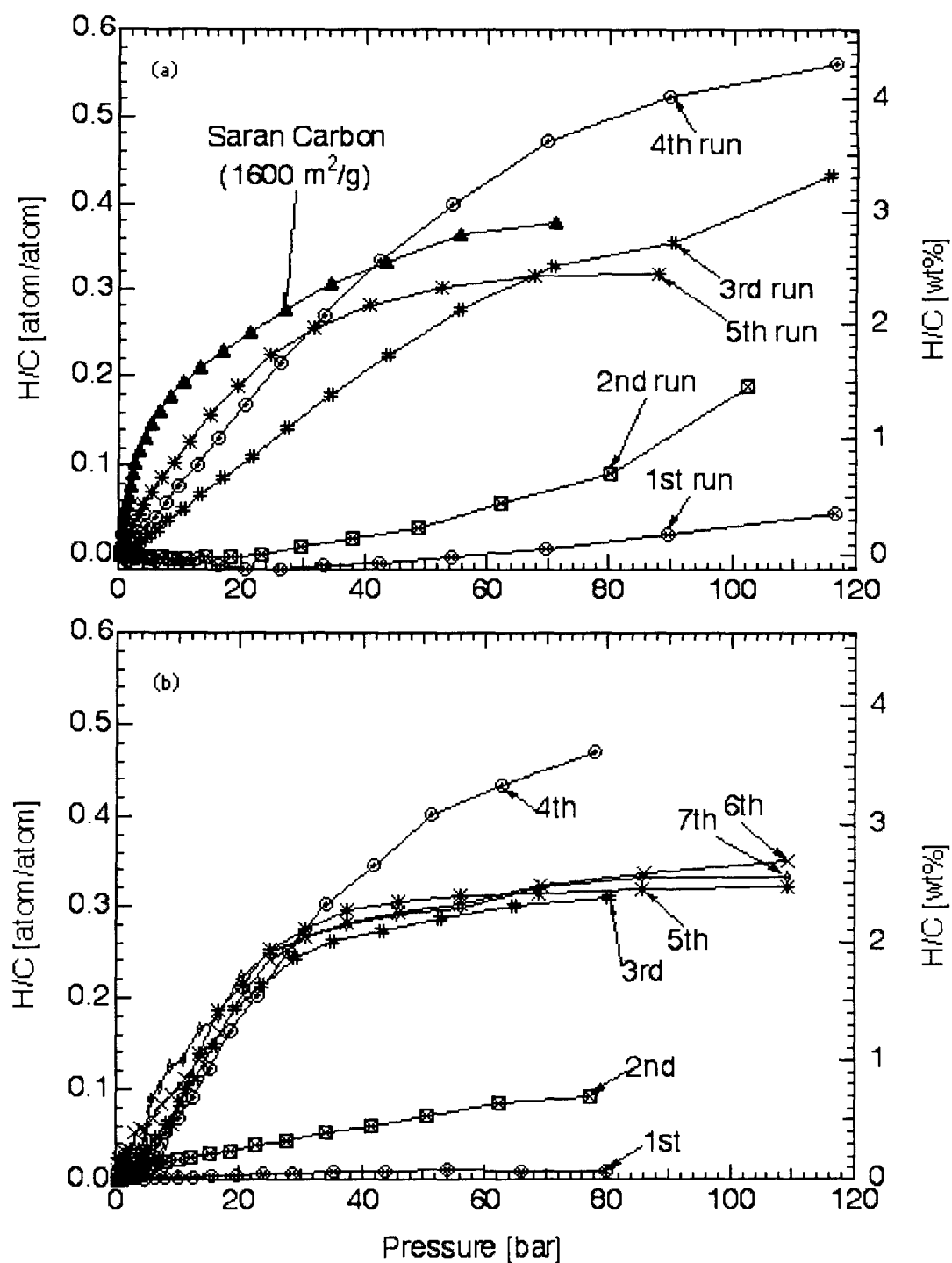


Figure 5.1: Desorption isotherms of composition versus pressure at 77 K for two different batches of fullerite sample #1 of C_{60} - C_{70} fullerite materials. The upper set includes a trace for Saran carbon. The lower set shows identical isotherm behavior as a function of adsorption/desorption cycle number.

K_{α} radiation. High performance liquid chromatography (HPLC) measurements were performed at MER Corp.

Sample	Composition	H ₂ Capacity wt% 300 K		H ₂ Capacity wt% 77 K		Surface area (m ² /g)	
		abs	des	abs	des	as-rec.	cycled
C ₆₀	99.9+%	0.07	0.08	0.83	0.70		
C ₇₀	98+%	0.12	0.12		0.33		
Fullerite #1	75%C ₆₀ 22%C ₇₀ 1.5%C ₆₀ oxides			4.00	0.58–4.38	0.9	11
Fullerite #2	75%C ₆₀ 22%C ₇₀ 0.2%C ₆₀ oxides			0.38–0.60	0.80–0.99	4	3
Fullerite #3	77%C ₆₀ 21%C ₇₀ 0.6%C ₆₀ oxides				0.2–0.3		

Table 5.1: H₂ storage capacities and BET surface areas of fullerenes.

The hydrogen adsorption/desorption and BET measurement results are summarized in Table 5.1. The hydrogen storage capacities of pure C₆₀ and C₇₀ are reproducible and are consistent with results of others [1]. On the other hand, fullerite sample #1 from MER and originally obtained in 1992 exhibited unusual isotherm behavior. As shown in Figure 5.1 (a), the capacity during the first desorption run on the as-received fullerite #1 (labeled 1st run) is small, comparable to the capacity of pure C₆₀ or pure C₇₀. The capacity then increased dramatically with each subsequent isotherm cycle. In the fourth cycle (labeled 4th run), it reached a maximum of 4.4 wt.% at 120 bar at 77 K. This value is consistent with complete H₂ adsorption onto the surfaces of the fullerene molecules, assuming that H₂ molecules of diameter 3.5 Å form a close packed shell around each fullerene molecule. At the fifth cycle, the capacity dropped back to about 2.5 wt.%. Samples of the same material were analysed for their surface area by the BET method. The BET surface area changed from 0.9 m²/g for the as-received fullerite #1 to 11 m²/g after 5 isotherm cycles.

In order to verify these results, we tested a 2nd batch of fullerite #1, and obtained the same isotherm behavior as a function of cycle number. These results are presented in Figure 5.1 (b). A total of seven cycles was performed on the 2nd batch of fullerite #1 and cycles 5 to 7 showed identical isotherm traces. On the other hand,

a similar Sievert's apparatus was used to measure one point of the isotherm at 77 K at about 50 bar, but this measurement showed only 0.05 wt.% hydrogen sorption. Sample handling procedures were similar although not identical, the reason for this discrepancy in these measurements is still unclear. Fullerite #2 behaved similarly to the samples of pure C₆₀ or pure C₇₀, and showed only small differences as a function of cycle number as shown in Table 5.1. Fullerite #3 which was obtained recently from MER and used as a control sample, showed even smaller desorption capacities than fullerite #2 at 77 K. For comparison, we also measured the hydrogen desorption of high surface area saran carbon [4].

HPLC measurements of these materials showed only slight variations in the C₆₀-C₇₀ ratio. Therefore, we believe that the important difference between fullerites #1, #2 and #3 is the amount of oxidized C₆₀ found in as-received fullerite #1. The oxidized C₆₀ accounts for ~2% of the as-received fullerite. The oxidized component was absent in the material after it had been cycled with H₂ gas. The oxidation of fullerite #1 occurred presumably over the 7 year time span from its synthesis to the time the desorption experiments were performed.

A pair of transmission electron microscope (TEM) micrographs shown in Figure 5.2 illustrates the instability of fullerite #1 under electron beam irradiation. The large particle in the left side of the upper bright field image is the residue of a larger fullerite particle. The remnants of this particle recondensed on the holey carbon support grid. The higher magnification dark field (DF) image at the bottom of Figure 5.2 shows a nanocrystalline microstructure of this recondensed fullerite. The typical grain size for the recondensed nanocrystalline fullerite is ~10 nm. Some instability under the electron beam was also observed for fullerite sample #2 and for C₇₀. The pure C₆₀ sample was stable under the electron beam.

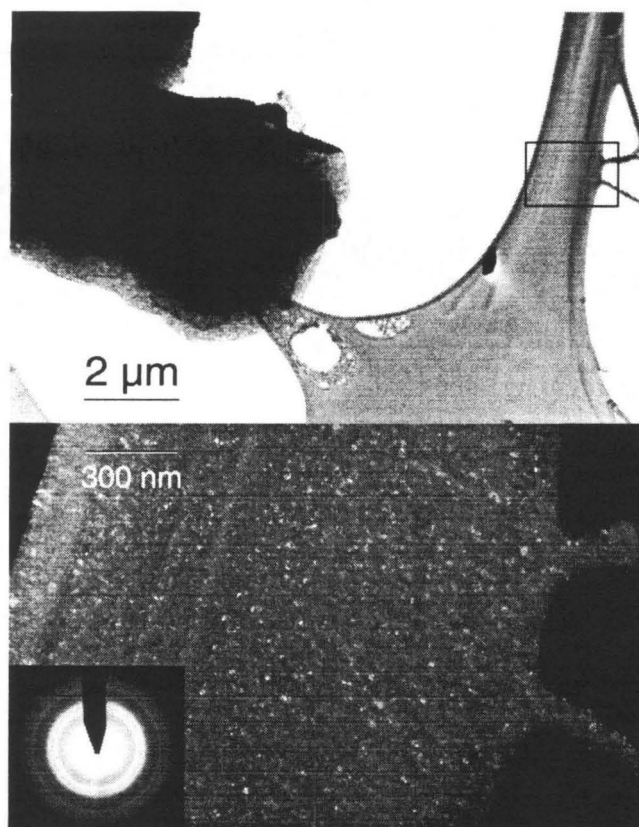


Figure 5.2: Transmission electron micrograph of fullerite #1, C_{60}/C_{70} . (a) low magnification bright field, and (b) higher magnification dark field of inset area showing recondensed fullerite nanocrystals.

5.3 X-Ray Diffraction Pattern and Phase Transformation of Fullerite

As introduced in Chapter 1.3.3, the C_{60} molecules crystallize into a face-centered cubic structure with a lattice constant of 14.17 \AA [5, 6]. At room temperature, the C_{60} molecules have been shown by nuclear magnetic resonance (NMR) [7, 8] to be rotating rapidly with three degrees of rotational freedom.

The crystal structure of C_{70} is more complex than that of C_{60} . The structural phase transitions and orientational ordering in C_{70} at different temperature and pressure have been studied extensively for the past decade [10, 11, 12, 13, 14]. Although there is still no agreement about the details of the structures, there is general agree-

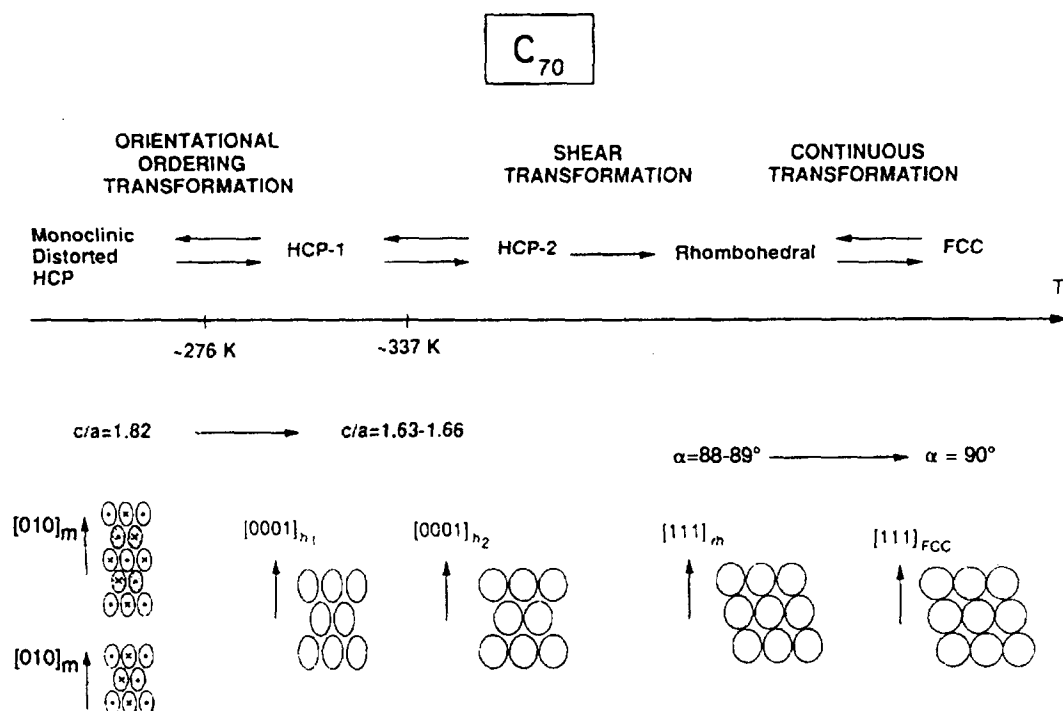


Figure 5.3: Phase diagram showing the various phases of C_{70} , the possible phase transitions, and the stacking of the molecules [14].

ment that there are three regimes, the high temperature regime (above $T_{01} = 340\text{K}$), the intermediate temperature regime ($275\text{ K} < T < 340\text{ K}$), and the low temperature regime (below $T_{02} = 275\text{ K}$), as shown in Figure 5.3. It is generally agreed that the structure is isotropic about T_{01} and becomes more anisotropic as T is decreased [9]. Five phases have been observed, including fcc [12], rhombohedral [10], ideal hcp ($c/a = 1.63$) [12, 10], deformed hcp ($c/a = 1.82$) [16, 15] and a monoclinic phase [10]. Some phase transitions occur over a wide temperature range and exhibit large hysteresis which depends on the thermal history of the sample [10, 17].

The X-ray diffraction patterns of all the samples are presented in Figure 5.5. The diffraction pattern of the pure C_{60} is indexed successfully as an fcc structure with $a = 14.2\text{\AA}$, as expected [5, 6], and it was nicely overlapped with the simulated pattern by Dr. Danut Dragoi with a software package *Crystallographica* by Oxford Cryosystems, as shown in Figure 5.4.

For fullerite samples, the broad peaks between the C_{60} (220) and (311) peaks are

contributed by C_{70} phases. As discussed above, the crystal structure of C_{70} is very complex and some phase transitions may occur over a wide temperature range during isotherm process.

Figure 5.5 shows that the diffraction pattern of C_{70} in fullerite #1 changed after several isotherm cycles. Due to the broadening and the low intensity of the C_{70} peaks, it is not possible for us to identify reliably the phases in the samples. However, the change in the diffraction pattern from $q=1.3$ to 1.4 \AA^{-1} indicates that some parts of the material have undergone a phase change after hydrogen cycling. Furthermore, the diffraction peaks from the C_{60} in fullerite #1 became sharper after cycling. On the other hand, the C_{60} diffraction peaks from fullerite #2 sharpened after cycling, but there was little change in the region of q from 1.3 to 1.4 \AA^{-1} .

We believe the high hydrogen adsorption of fullerite sample #1 is a consequence of a hydrogen-induced structural transition in the fullerite. Carbon single-walled nanotubes (SWNT/s) undergo a hydrogen-induced structural phase transition [18]. Three energies are involved. One energy is the energy of adsorption of the H_2 molecule on the surface of the carbon. For SWNT's this energy for hydrogen physisorption was approximately the -38 meV that is characteristic of adsorption on graphite, and we expect this adsorption energy to be similar for hydrogen adsorption on C_{60} and C_{70} . The second energy is the van der Waals energy of cohesion of the C_{60} and C_{70} crystals. Evidently these van der Waals interactions in pure C_{60} and C_{70} are sufficiently strong so that the crystals remain intact and the hydrogen sorption is limited to absorption in interstitial sites and adsorption on the relatively few surface sites. The third "energy" is the chemical potential of the hydrogen molecules, which increases with the pressure of hydrogen gas. It is possible to reduce this contribution to the total free energy by surface adsorption of some of the hydrogen. The amount of adsorption will increase with pressure as modeled by the Langmuir isotherm, for example. The phase transition in the SWNT material was driven by this reduction in hydrogen chemical potential during physisorption, which was sufficient to overcome the van der Waals attraction between the tubes in a rope, separating them into individual tubes with a large surface area for hydrogen adsorption.

Evidently this phase transition does not occur in the samples of pure C_{60} or C_{70} , and these materials remain intact because their van der Waals attractions are strong. The van der Waals interaction and other electron-electron correlation effects responsible for cohesion decrease rapidly with distance, however. It is likely that crystalline defects in the C_{60}/C_{70} fullerite #1, perhaps induced by the phase transitions in the C_{70} regions, or by oxidation, could reduce the cohesive energy of the fullerite so that the process of hydrogen adsorption became more competitive energetically. The shapes of the isotherms of sample #1 were not reproducible, indicating that its cohesive energy was altered after a hydrogen sorption/desorption cycle. The x-ray diffraction patterns of sample #1 also showed a change in structure, and this sample also showed an unusual increase in surface area. (Although the increase in surface area is itself too small to account for significant physisorption, we note that the surface area measured by BET was not for material in contact with high pressure hydrogen gas.

The isotherms of sample #1 are difficult to interpret because their shape changes, but some of their features are noteworthy. The second isotherm run in Figure 5.1a may show some of the characteristics of the SWNT isotherms, which underwent a steep increase in hydrogen adsorption once a critical pressure was attained. This second run suggests a critical pressure in excess of 100 bar. The third, fourth, and fifth runs have some similarities to conventional adsorption isotherms, although their shapes are irregular and their characteristic adsorption pressure is not well defined. This irregularity could be a consequence of the heterogeneity of the hydrogen-induced structural phase transformation in impure fullerite, and an accompanying change in surface area resulting in a combination of macroporous to microporous adsorbant behavior [19]. It is of interest to note that the maximum value of adsorption attained in the fourth isotherm corresponds to complete surface adsorption by all of the C_{60} and C_{70} molecules. This implies that further improvements in the hydrogen adsorption capacities of mixed fullerite materials may be difficult to achieve.

5.4 Discussion

We suggest two possible origins for lower cohesive energy of fullerite #1 than fullerite #2. The microstructural distribution of C_{60} , C_{70} , and higher fullerene molecules may differ owing to differences in material preparation, causing differences in the structural transformations under temperature and hydrogen pressure. Recall that the chemical potential of hydrogen gas is proportional to the logarithm of its pressure, so modest changes in the cohesive energy could cause large changes in the pressure for the hydrogen-induced phase transition. Differences in the breadth of the fcc C_{60} peaks in the diffraction patterns are evidence for a microstructural difference between the fullerites #1 and #2, and these peaks underwent an observable change after fullerite #1 was cycled.

The cohesive energy could also differ between fullerites #1 and #2 because of the more extensive oxidation of the C_{60} in fullerite #1. The cyclic exposure to hydrogen gas reduced the oxidized C_{60} in fullerite #1, perhaps causing an increase of its cohesive energy and the observed reduction of hydrogen storage capacity after 4 cycles. The C_{60} oxide was absent after five cycles, but the hydrogen adsorption capacity of fullerite #1 remained large, so we do not attribute all of the difference between fullerite samples to oxidation. We do note, however, that oxidation has been observed to influence structural phase transitions in pure C_{60} [20] and seen to affect mechanical properties in C_{60} [21] and electronic properties [22] in carbon nanotubes.

Compared to SWNT materials, mixed fullerites have much lower cost. If the fullerite instabilities could be controlled to provide a large change in hydrogen adsorption over a narrow range of pressure, as is possible for SWNT materials, fullerites may be candidate materials for some hydrogen storage applications. The relationship between the structure and properties of the mixed fullerite samples remains uncertain, however. Further investigation will be required to identify the origin of the structural instability of fullerites like fullerite #1.

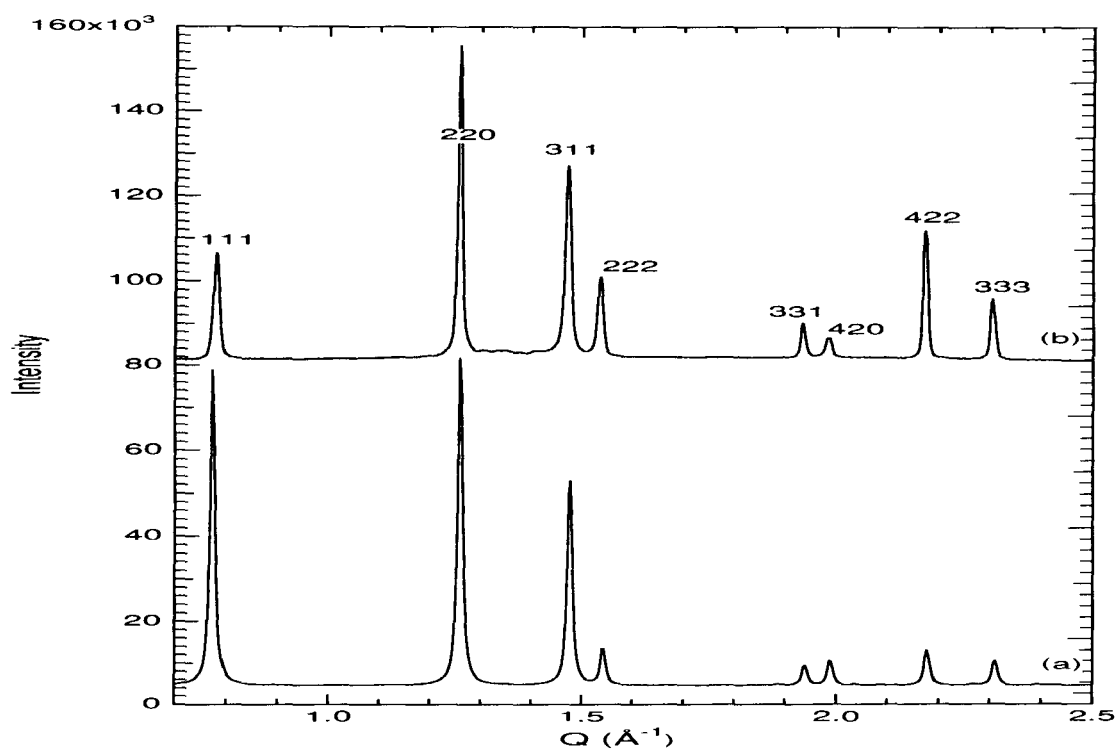


Figure 5.4: X-ray diffraction pattern of (b) pure C_{60} (99.9+%) and (a) simulated with Crystallographica.

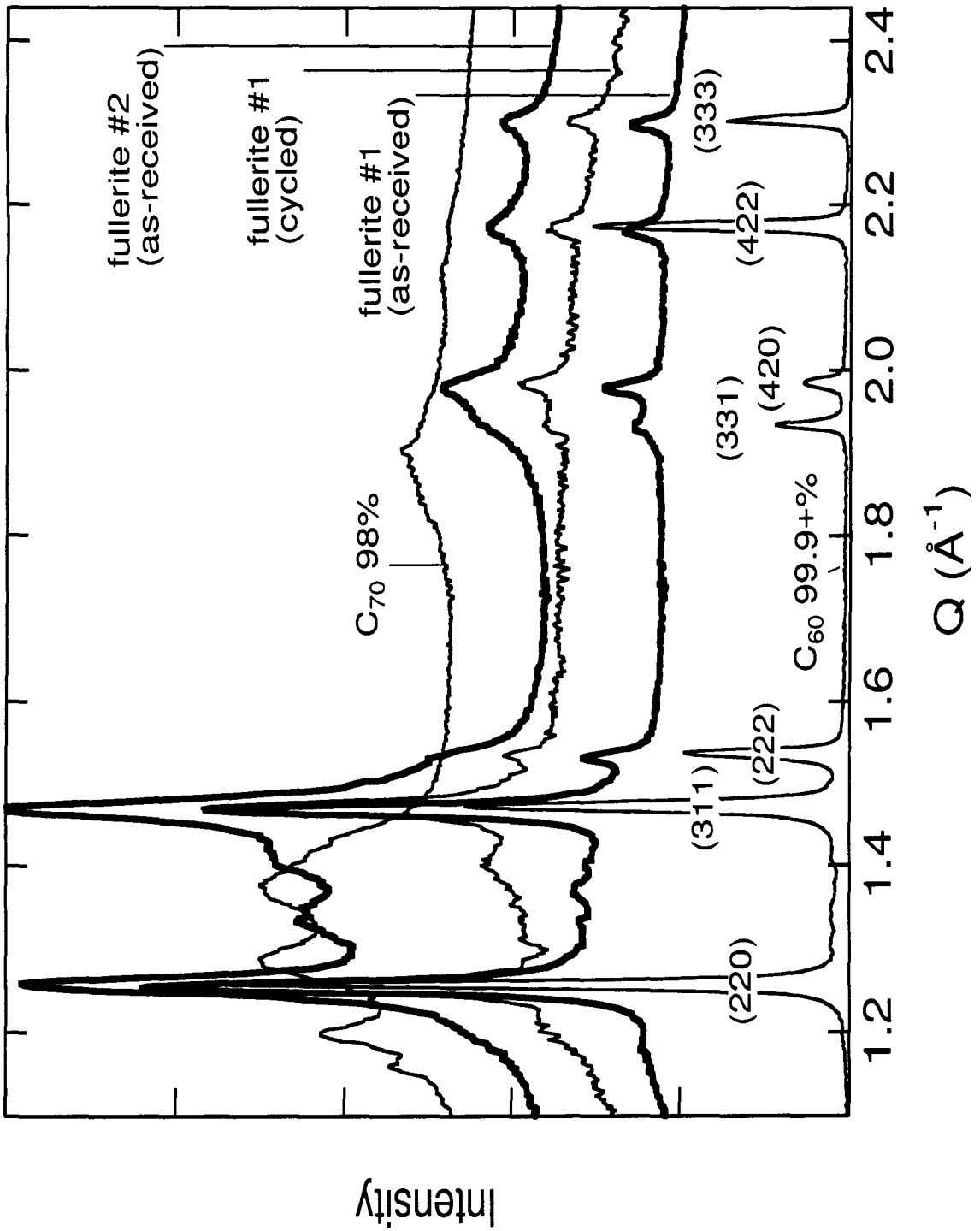


Figure 5.5: X-ray diffraction of all fullerene samples.

Bibliography

- [1] X. Lu, R. O. Loutfy, E. Veksler, and J. C. Wang, *Proc. of Symp. on Recent Adv. in the Chem. and Phys. of Fullerenes and Related Materials*, **823** (1998).
- [2] H. W. Kroto, J. R. Heath, S. C. O'Brien, R. F. Curl, and R. E. Smalley. *Nature (London)*, **318**, 162 (1985).
- [3] S. Saito and A. Oshiyama, *Phys. Rev. B*, **44**, 11532 (1991).
- [4] C. C. Ahn, Y. Ye, B. V. Ratnakumar, C. C. Witham, R. C. Bowman, and B. Fultz. *Appl. Phys. Lett.* **73**, 3378 (1998).
- [5] P. W. Stephens, L. Mihaly, P. Lee, R. Whetten, S. M. Huang, R. Kaner, F. Deiderich, and K. Holczer, *Nature (London)*, **351**, 632 (1991).
- [6] A. R. Kortan, N. Kopylov, S. H. Glarum, E. M. Gyorgy, A. P. Ramirez, R. M. Fleming, F. A. Thiel, and R. C. Haddon. *Nature (London)*, **355**, 529 (1991).
- [7] Q. M. Zhang, J. Y. Yi, and J. Bernholc, *Phys. Rev. Lett.*, **66**, 2633 (1991).
- [8] R. D. Johnson, C. S. Yannoni, H. C. Dorn, J. R. Salem, and D. S. Bethune, *Science*, **255**, 1235 (1992).
- [9] M. S. Dresselhaus, G. Dresselhaus, and P. C. Eklund, *Science of Fullerenes and Carbon Nanotubes*, Academic Press, San Diego (1996).
- [10] A. R. McGhie, J. E. Fischer, P. W. Stephens, R. L. Cappelletti, D. A. Neumann, W. H. Mueller, H. Mohn, and H. U. ter Meer. *Phys. Rev. B*, **49**, 12614 (1994).
- [11] G. van Tendeloo, S. Amelinckx, M. A. Verheijen, P. H. M. van Loosdrecht, and G. Meijer, *Phys. Rev. Lett.*, **69**, 1065 (1992).

- [12] G. B. M. Vaughan, P. A. Heiney, J. E. Fischer, D. E. Luzzi, D. A. Ricketts-Foot, A. R. Mcghie, U. W. Hui, A. L. Smith, D. E. Cox, W. J. Romanow, B. H. Allen, N. Coustel, J. P. Mccauley, Jr., and A. B. Smith III. *Science*, **254**, 1350 (1991).
- [13] G. B. M. Vaughan, P. A. Heiney, D. E. Cox, J. E. Fischer, A. R. McGhie, A. L. Smith, R. M. Strongian, M. A. Cichy, and A. B. Smith III. *Chem. Phys.*, **178**, 599 (1993).
- [14] M. A. Verheijen, H. Meekes, G. Meijer, P. Bennema, J. L. de Boer, S. van Smaalen, G. van Tendeloo, S. Amelinckx, S. Muto and J. van Landuyt. *Chem. Phys.*, **166**, 287 (1992).
- [15] S. van Smaalen, V. Petricek, J. L. de Boer, M. Dusek, M. A. Verheijen, and G. Meijer. *Chem. Phys. Lett.*, **223**, 323 (1994).
- [16] E. Blanc, H. B. Burgi, R. Restori, D. Schwarzenbach, and Ph. Ochsenbein. *Europhys. Lett.*, **33**, 205 (1996).
- [17] J. E. Fischer and P. A. Heiney, *J. Phys. Chem. Solids*, **54**, 1725 (1993).
- [18] Y. Ye, C. C. Ahn, C. Witham, B. Fultz, J. Liu, A. G. Rinzler, D. Colbert, K. A. Smith, and R. E. Smalley. *Appl. Phys. Lett.*, **74**, 2307-2309 (1999)
- [19] M. D. Donohue and G. Al. Aranovich, *Adv. Colloid Interface Sci.* **76-77** 137, (1998).
- [20] F. Yan and Y. Wang, *J. Phys. Chem. Sol.*, **61**, 1003 (2000).
- [21] I. Manika, J. Manika, and J. Kalnacs, *Carbon*, **36**, 641, (1998).
- [22] P. G. Collins, K. Bradley, M. Ishigami, and Z. Zettl, *Science*, **287**, 1801, (2000).

Chapter 6 Carbon Supported Catalysts

It has been reported that transition metals dispersed on the surface of activated carbon may increase the hydrogen storage capacity. This occurs at a pressure of one bar or greater at temperature near 77 K [1].

In recent years, a number of studies have been devoted to the phenomenon of *spillover*, which is defined as the migration of adsorbed species from one solid phase where it is easily adsorbed, onto another solid phase in contact with the first, where it is not directly adsorbed. Hydrogen adsorbed on the metal crystallites can migrate to the metal support in an activated form [6]. This effect could be extremely sensitive to the impregnation procedure and to modifications due to the impregnation process.

Recently, a group of researchers at the Oak Ridge National Laboratory and the Materials & Electrochemical Research Corporation claimed that they achieved 6 wt.% hydrogen storage capacity around 200°C using fullerenes and some liquid organic hydrides by adding liquid catalysts or doping alkali ions into fullerenes [8, 9]. This capacity corresponds to $C_{60}H_{48}$.

The work described in this chapter involved the preparation of nickel catalysts supported on fullerenes and activated carbon samples. Their hydrogen adsorption/desorption isotherms were measured at various temperatures.

6.1 Ni Catalyst Particle Size Control and Calculation

A fullerite sample obtained from MER in 1999 was used as the starting fullerite for the support of impregnation. (This fullerite sample was denoted as fullerite #3 in Chapter 5.) An activated carbon from Darco (KB-B-100), denoted as DAC, was also used as the medium of a catalyst support. The surface area of DAC is 1550 m²/g

as measured by BET. The support was impregnated with a solution of nickelous nitrate to obtain a designated metal loading. After impregnation, the catalyst was dried overnight in a fume hood at room temperature and reduced in a furnace under hydrogen flow.

During impregnation of the solution, the concentration of the solution, the metal compounds' readiness to be absorbed onto the substrate and capillarity will all contribute to the impregnation profile. During the subsequent drying step, the segregation and evaporation speed are important parameters. For the activation step, conditions of calcination and reduction, such as temperature and gas composition, need to be controlled properly. The detailed preparation techniques are described in section 2.1.5. A total of ten Ni/DAC samples and several Ni/fullerite samples were prepared. The preparation conditions are listed in Table 6.1.

sample	solution concentration (g/ml)	Ni composition (wt.%)	reduction temperature (°C)	particle diameter (nm)
Ni/DAC #1	0.1	~ 10	550°C	~50
Ni/DAC #3	0.05	2	400°C	~ 5
Ni/DAC #4	0.025	1.0	500°C	~ 5
Ni/DAC #5	0.025	2	450°C	~ 9
Ni/DAC #7	0.05	6	500°C	~15
Ni/DAC #8	0.1	5	500°C	~10
Ni/DAC #9	0.05	2	500°C	~ 7
Ni/DAC #10	0.1	2	500°C	~ 8
Ni/Fullerite	0.05	5	500°C	~ 20

Table 6.1: Preparation and characterization of carbon supported Ni catalyst particles.

To characterize the nickel particles, dark field transmission electron microscopy was performed with a Philips EM430 transmission electron microscope operated at 200 kV. X-ray powder diffractometry was performed on samples with an Inel CPS-120 powder diffractometer using Co K_α radiation. The particle sizes were determined by X-ray line broadening and direct measurement in the TEM images.

6.1.1 Ni/Activated Carbon

A dark field TEM image of Ni/DAC #5 is shown in Figure 6.1. Nanosized nickel particles were distributed on the surface of activated carbon. Although the pore structure of the carbon is unclear, we expect there are numerous micropores, consistent with the high specific surface area ($1550 \text{ m}^2/\text{g}$).

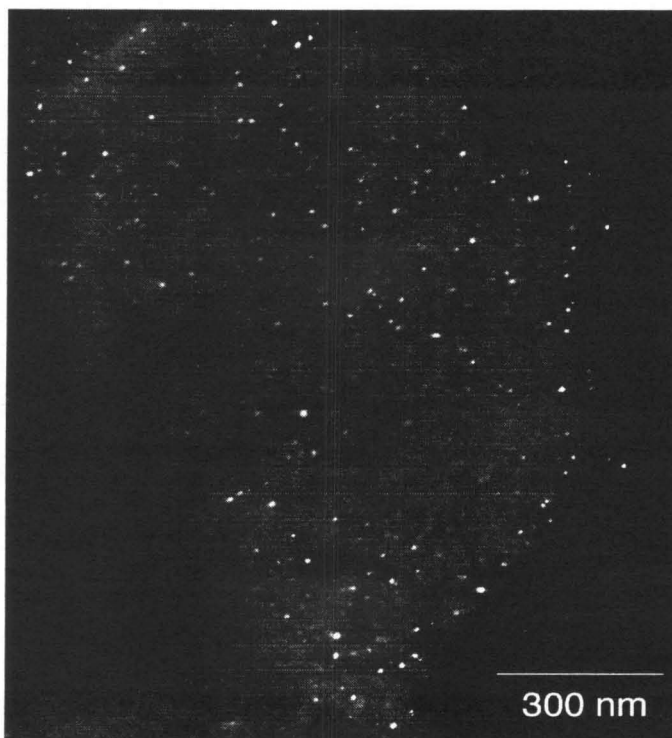


Figure 6.1: Dark field TEM images of Ni catalyst particles supported on the Darco activated carbon.

X-ray diffraction patterns of Ni/DAC samples are shown in Figure 6.2 and the calculated particle sizes from the line shapes are summarized in Table 6.1. The large particle size of Ni/DAC #1 was due to the high Ni composition. Differing reduction temperature also resulted in the change of particle size and distribution. This suggests that Ni composition and reduction temperature are two dominant factors in the catalyst preparation process.

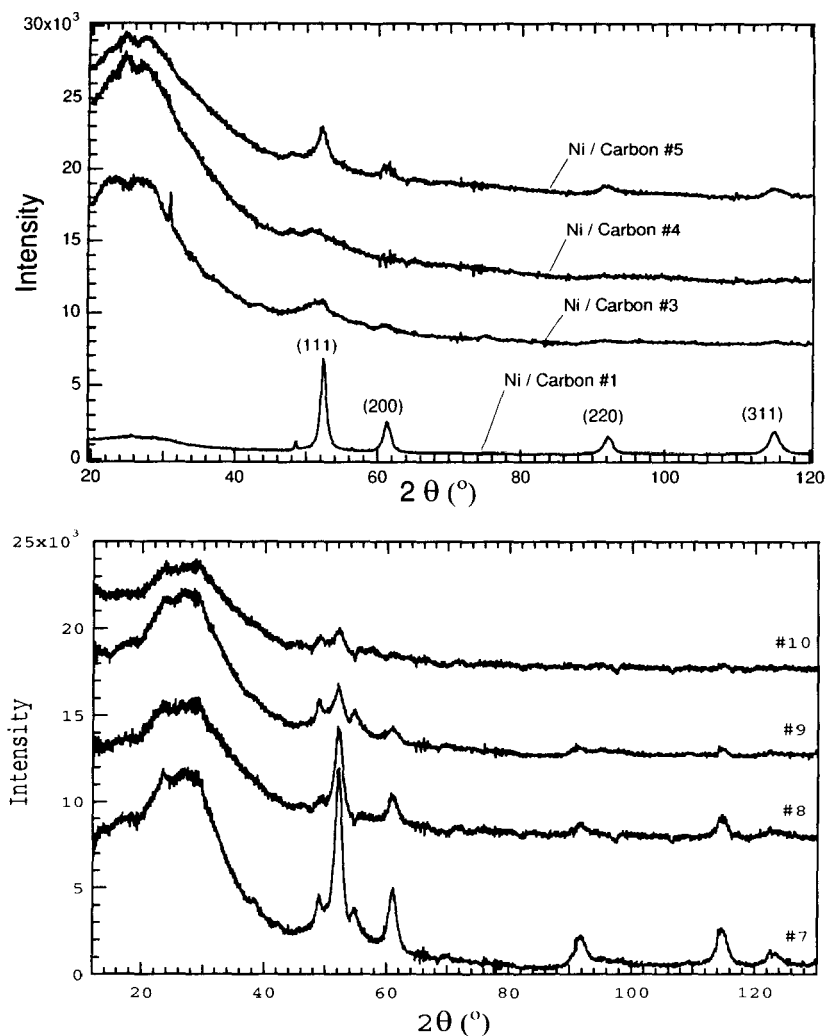


Figure 6.2: X-ray diffraction patterns of Ni/activated carbon samples.

6.1.2 Ni/Fullerite

The solubility of fullerenes in water is very low, thus the fullerite sample was not readily to adsorb the nickelous component from its aqueous solution. An ultrasonic bath was employed to agitate and mix the sample thoroughly. Sonication treatment is beneficial for catalyst preparation, catalyst activation, and catalytic reaction involving solid catalyst/reagents. It is normally considered that the improvement of reactivity of solid catalysis was caused by the creation of surface defects, the reduction of particle size, and the dispersion of the catalyst particles on the support [7]. The X-ray diffraction patterns of a set of Ni/fullerite samples are shown in Figure

6.3. The particle size of the Ni catalyst was smaller after sonication treatment, when all other preparation parameters were the same.

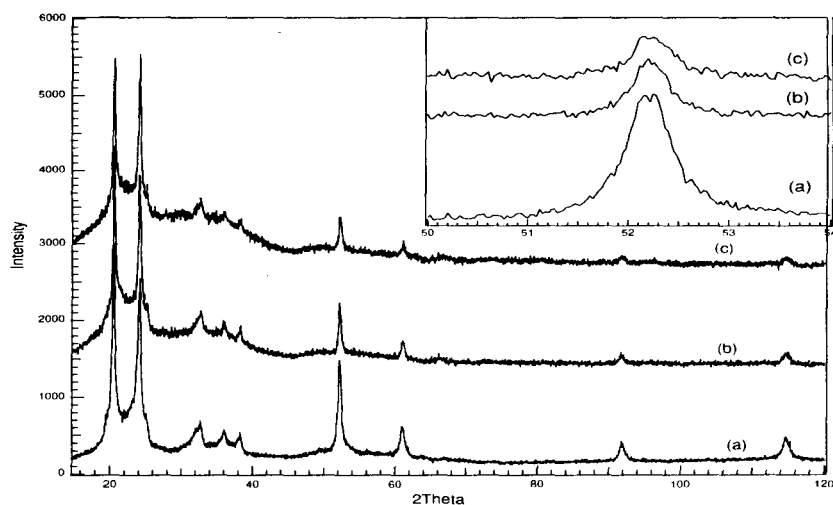


Figure 6.3: X-ray diffraction patterns of Ni/fullerite samples. (a) fullerite from Aesca, (b) fullerite from MER, and (c) fullerite from MER with sonication used for catalyst preparation process.

6.2 Results and Analysis

6.2.1 Isotherm Measurement

Before measurements of hydrogen adsorption and desorption, the samples were degassed at 200°C overnight. The Sieverts' apparatus was thoroughly leak-checked at 200 bar and calibrated to ensure reliable determination of the hydrogen storage properties.

Desorption measurements were performed at 77 K, 300 K and 450 K. H₂ gas was admitted into the evacuated reactor to achieve a typical pressure of 80 bar. This pressure was maintained for 15 hr to allow the sample to reach equilibrium and to check for leaks in the system. The reactor was valved off from the rest of the system and the system was evacuated again. The desorbed H₂ was then determined from the system volume and data measured by a pressure transducer. Desorption isotherms of fullerite and Ni/fullerite samples are shown in Figure 6.5 and 6.5.

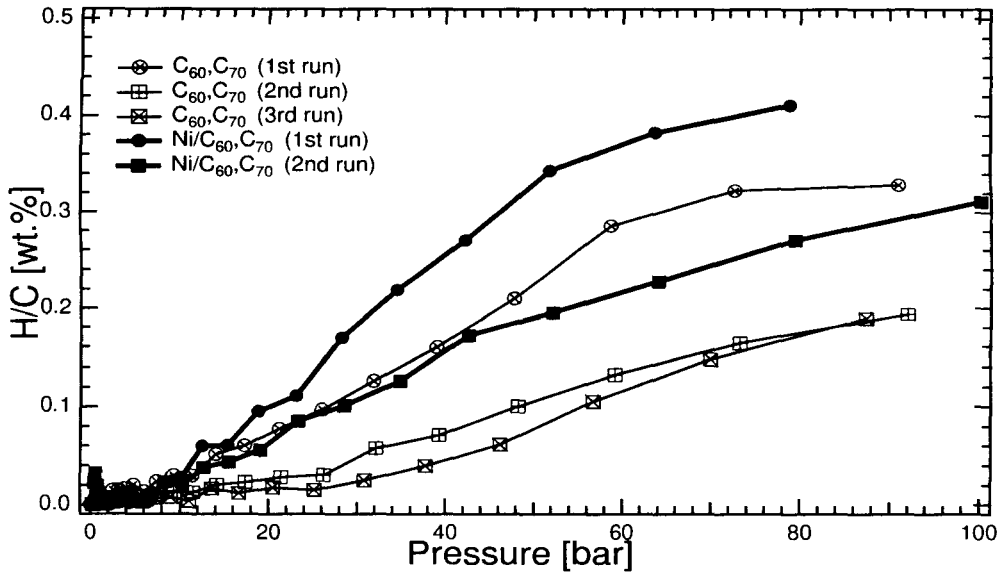


Figure 6.4: Desorption isotherms of composition versus pressure at 77K for fullerite and Ni/fullerite samples.

Adsorption isotherm measurements were also performed manually. The sample was first degassed at 200°C and the manifold was evacuated. The reactor was valved off before H₂ was introduced into the rest of the system and the pressure was recorded. A valve was opened to allow the sample to make contact with H₂, and the pressure was recorded again after equilibrium was achieved. This was one complete step of the adsorption measurement. The reactor was valved off and the pressure of the manifold was raised by introducing more hydrogen into the system. These steps were repeated and the pressure before and after the valve was opened was recorded until the pressure of the whole system reached about 100 bar. Some adsorption isotherms are shown in Figure 6.6.

6.2.2 Isotherm Results

The results of desorption and adsorption isotherms at 77 K, 300 K, and 450 K are summarized in Table 6.2. From Table 6.2, we see several trends. The desorption capacity of the sample was lower than the adsorption capacity of the same sample at the same isotherm condition. By adding Ni particles on the sample, the hydrogen

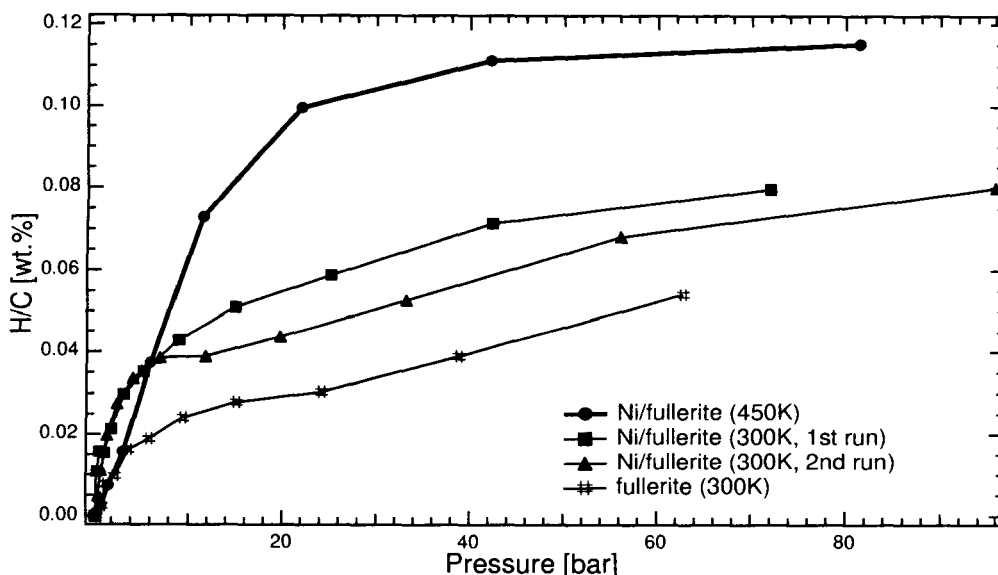


Figure 6.5: Desorption isotherms of composition versus pressure at 300K and 450K respectively, for Ni/fullerite samples.

storage capacity of fullerite sample was increased. This was also observed for the DAC samples. The Ni particles may adsorb some hydrogen, but this can not account for the total increased capacity even by assuming complete coverage of hydrogen molecules on the Ni particle surface. Assuming 5 wt.% of Ni particles are aggregated as spheres of 20 nm diameter; the complete coverage of hydrogen on the Ni particle surface is equivalent to 0.01 wt.% hydrogen storage capacity. We suggest that the hydrogen adsorbed and dissociated on the surface of Ni particle may migrate onto the surface of supporting carbon, which is called hydrogen *spillover*.

The capacities of both Ni/fullerite and Ni/DAC samples at elevated temperature

Sample	H ₂ Capacity @77K (wt%)		H ₂ Capacity @300K (wt%)		H ₂ Capacity @450K (wt%)	
	abs.	des.	abs.	des.	abs.	des.
DAC			0.2		0.04	0.02
Ni/DAC			0.27		0.4	0.12
fullerite		0.2-0.3		0.06		
Ni/fullerite		0.3-0.4	0.1	0.08	0.2	0.11

Table 6.2: Hydrogen storage capacities of carbon samples with or without catalysts.

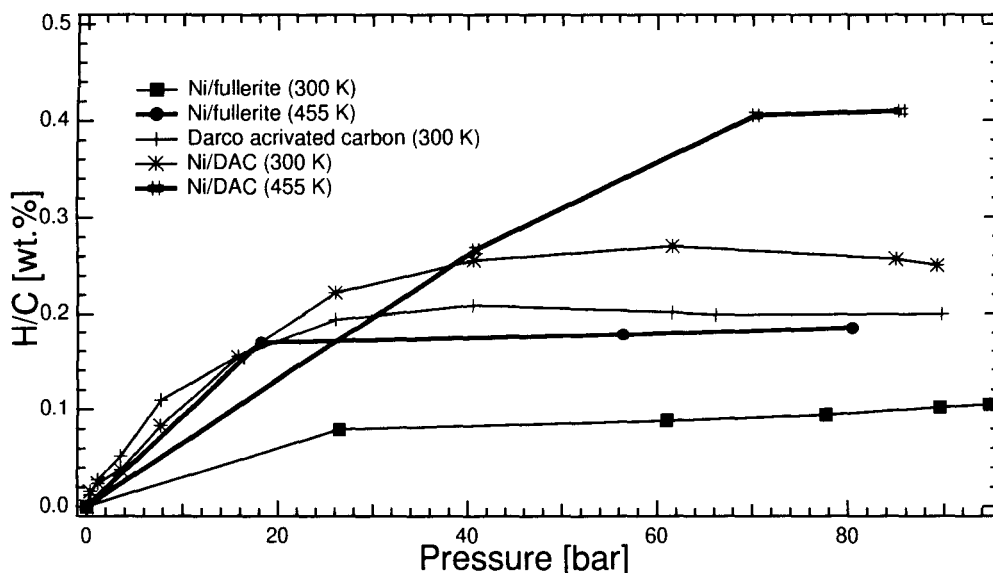


Figure 6.6: Adsorption isotherms of composition versus pressure at 300K and 450K respectively, for Darco activated carbon, Ni/DAC, fullerite and Ni/fullerite samples.

(450 K) increased by a factor of two compared to those measured at ambient temperature. From the thermodynamics of adsorption, the fractional coverage of the surface increases with decreasing temperature and increasing pressure. However, the fullerite sample with Ni catalyst adsorbed more hydrogen at 450 K. This can be explained as the better performance and higher activity of Ni catalysts at high temperature.

6.2.3 Fourier Transform Infrared Spectrometry

Since the amount of hydrogen desorbed was less than adsorbed, some hydrogen molecules must have remained on the sample after the desorption. To determine the mechanism of adsorption and check if there were any hydrogen carbon bonds formed, infrared spectrum were measured with a 860 Magna series FTIR spectrometer. Infrared spectroscopy is a standard chemical analysis tool to identify molecular structures through molecular vibrations. The peaks around 2900 cm^{-1} are due to CH bond stretching.

To obtain the transmission spectrum, samples were prepared into potassium bromide pellets. Approximately 1 mg sample and 200 mg KBr were ground and mixed

in the mortar and pressed into a transparent pellet in a press. The pellet was then placed in a pellet holder to obtain the spectrum. A background spectrum was also obtained from an empty pellet holder.

A strong absorption at 2900 cm^{-1} was observed for the as-received samples of both fullerite and Darco activated carbon. This indicates that there may be some contamination and/or a portion of CH bonds on the surface of carbon samples. It was reported that there are several types of hydrogen bonds in coal, formed by hydroxyls with various hydrogen-bonding acceptors [10, 11].

After isotherm measurement at ambient temperature, the fullerite sample showed a weaker absorption peak at 2900 cm^{-1} . The absorption intensity of as-prepared Ni/fullerite sample was also weaker than that of as-received sample. There is no significant absorption for the Ni/fullerite sample after isotherm at elevated temperature.

Before each hydrogen isotherm measurement, the sample was degassed at about 200°C . This process may have driven off the contamination. The reason for the disappearance of CH bonds after high temperature hydrogen isotherm is unclear.

6.3 Conclusion

The hydrogen storage capacity of fullerite and activated carbon samples was increased by adding Ni particles onto the sample. The adsorption of hydrogen on Ni particles cannot account for the total increased capacity, even by assuming complete coverage of hydrogen molecules on the Ni particle surface. The increasing of adsorption capacity was much more significant at elevated temperature, suggesting improved catalytic activity rather than improved thermodynamic adsorption.

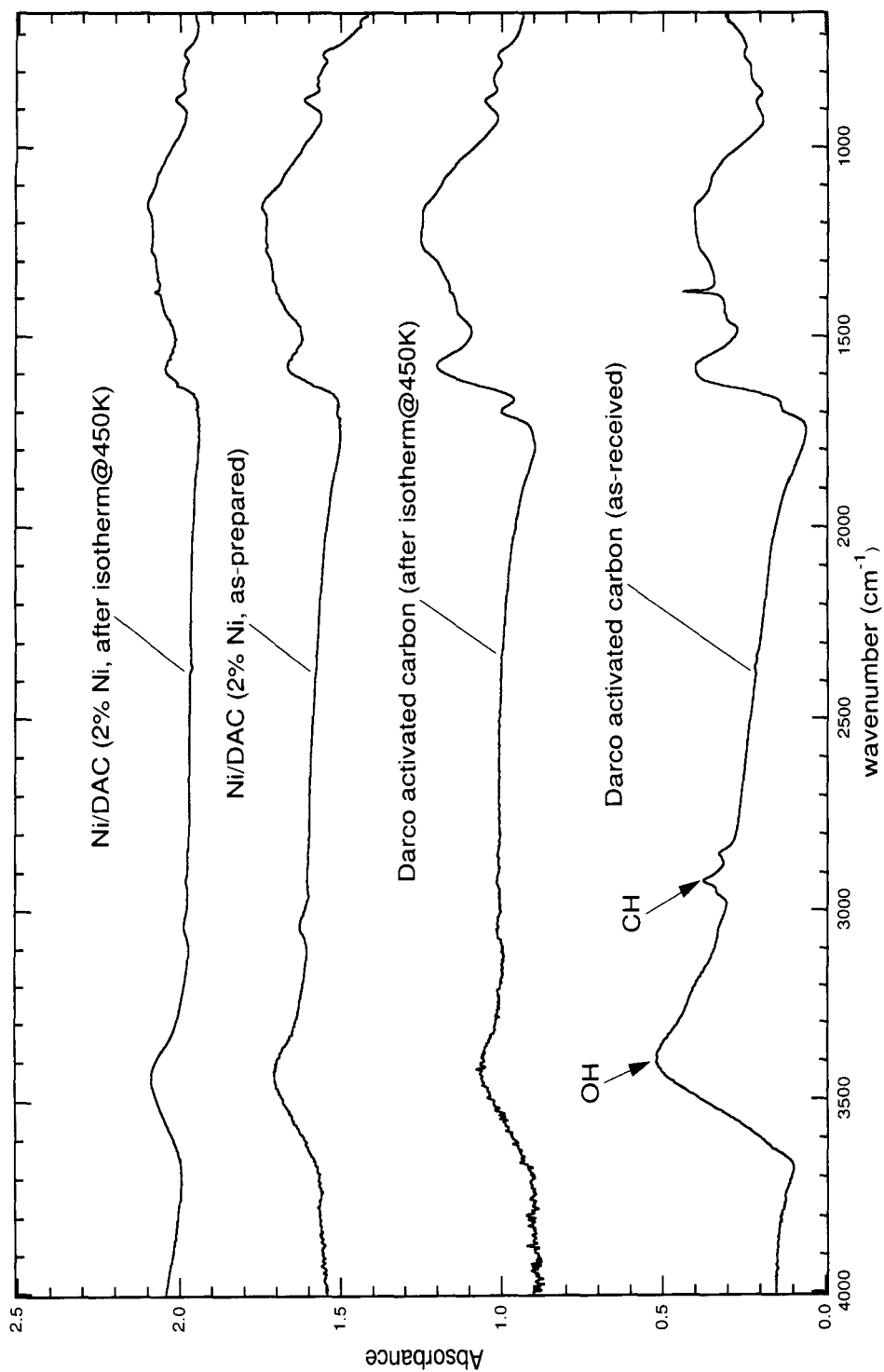


Figure 6.7: Fourier transform infrared spectrum of Darco activated carbon and Ni/DAC samples.

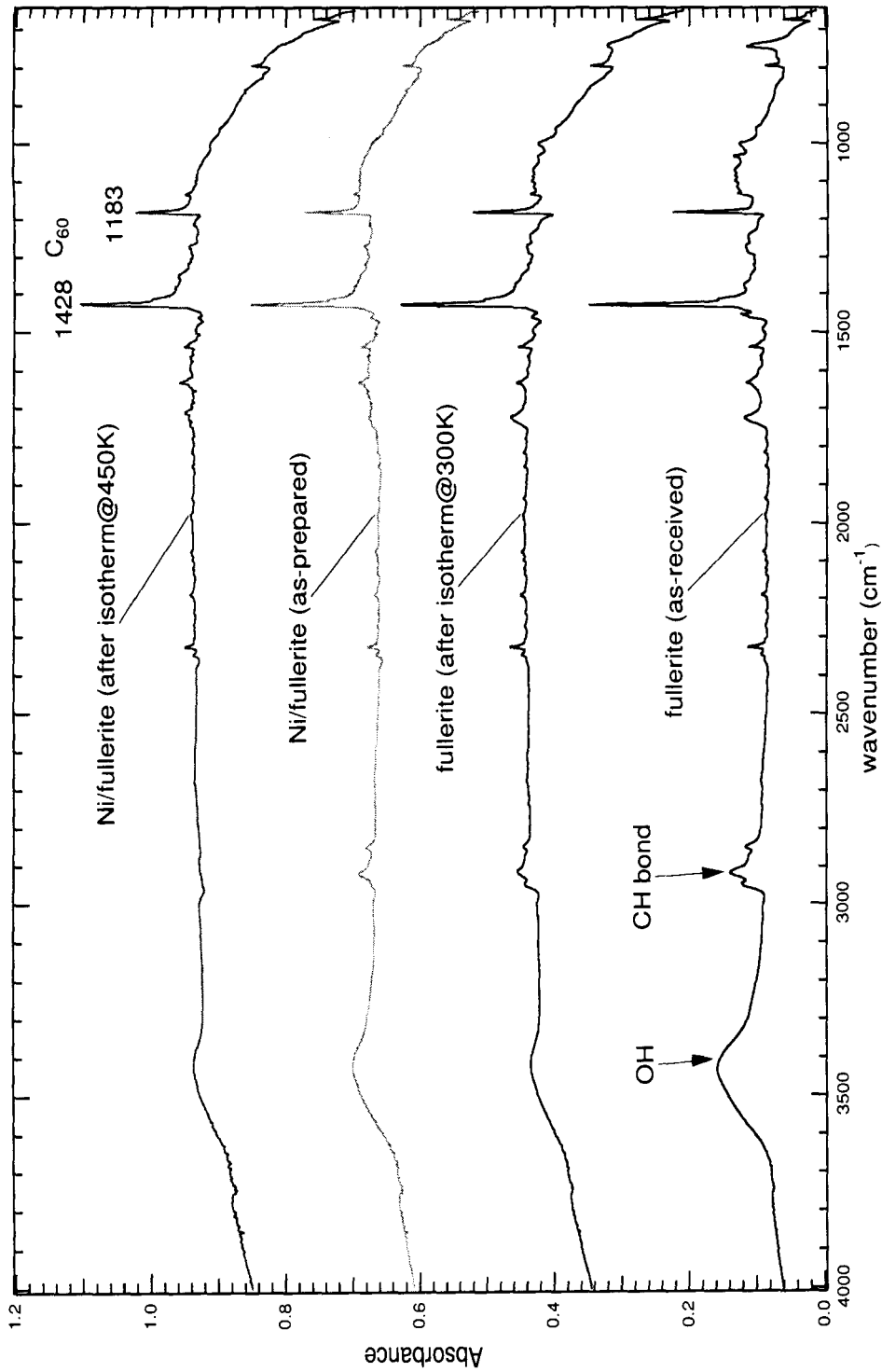


Figure 6.8: Fourier transform infrared spectrum of fullerite sample and Ni/fullerite samples.

Bibliography

- [1] J. A. Schwarz, "Metal Assisted Carbon Cold Storage of Hydrogen," U. S. Patent #4,716,736, Issued Jan. 5, 1988.
- [2] Yu. A. Borisov, Yu. A. Zolotarev, E. V. Laskatelev, and N. F. Myasoedov, "Quantum-chemical calculation of a spillover model on a graphite support." *Russian Chem. Bulletin.*, **46**, 428 (1997).
- [3] A. Sepúlveda-Escribano, F. Coloma, and F. Rodríguez-Reinoso, *Appl. Catal. A: General* **173** 247 (1998).
- [4] Z. X. Cheng, S. B. Yuan, J. W. Fan, Q. M. Zhu, and M. S. Zhen, in Spillover and Migration of Surface Species on Catalysts, Elsevier Science (1997).
- [5] I. Nakamura, A. Zhang, Y. Fan, and K. Fujimoto, in Spillover and Migration of Surface Species on Catalysts, Elsevier Science (1997).
- [6] B. Mahipal Reddy, S. T. Srinivas, and P. K. Rao, *Indian J. of Chem.*, **31A**, 957(1992).
- [7] S. Ley and C. Low, Ultrasonics in Synthesis, Springer-Verlag, Berlin Heidelberg (1989).
- [8] J. C. Wang, R. W. Murphy, F. C. Chen, R. O. Loutfy, E. Veksler, and W. Li, "Hydrogen Storage in Fullerenes and in Organic Hydrides," in *Proceedings of the 1998 U. S. DOE Hydrogen Program Review*, NREL/CP-570-26938.
- [9] J. C. Wang, R. W. Murphy, F. C. Chen, R. O. Loutfy, E. Veksler, and A. Singh, "Hydrogen Storage in Fullerenes and Liquid Organic Hydrides," in *Proceedings of the 1999 U. S. DOE Hydrogen Program Review*, NREL/CP-570-25315.

- [10] C. Chen, J. Gao, and Y. Yan, *Energy & Fuels*, **12**, 446 (1998).
- [11] R. W. Snyder, P. C. Painter, J. R. Havens, and J. L. Koenig, *Appl. Spectrosc.*, **37**, 497 (1983).

Chapter 7 Conclusions and Outlook for Further Work

7.1 Conclusions

The hydrogen storage properties of some traditional carbon materials (activated carbon) and novel ones (fullerenes, graphite nanofibers and carbon nanotubes) were explored. The results are summarized in Table 7.1.

Carbon samples	Specific Surface Area (m ² /g)	H ₂ Capacity wt% 77K		H ₂ Capacity wt% 300K		H ₂ Capacity wt% 450K	
		ads.	des.	ads.	des.	ads.	des.
AX-21	3000		2		0.5		
Saran carbon	1600		2.2		0.4		
GNF	20-30		0.15		0.1-0.2		
SWNT	285		4-7		0.8		
C ₆₀		0.8	0.7	0.07	0.08		
C ₇₀			0.3	0.12	0.12		
Fullerite #1	0.9-11	4	0.6-4				
Fullerite #3	3-4		0.2-0.3		0.06		
Ni/fullerite			0.3-0.4	0.1	0.08	0.2	0.11
Darco activated C	1550			0.2		0.04	0.02
Ni/DAC				0.27		0.4	0.12

Table 7.1: Summary of hydrogen storage capacities and surface areas of carbon samples.

As a result of our analysis, it seems unlikely that carbon in nanofiber form shows H₂ adsorption/desorption properties that would have the spectacular impact as a solid state storage medium claimed by Rodriguez's group at Northeastern University. Thus there is no point in following up with graphite nanofibers.

A phase transition between crystal SWNT and a new hydride phase was found at high pressures at 80K. The phase transition was of first order, and involved the

separation of the individual tubes within a rope, exposing a high surface area for hydrogen adsorption. From the change in chemical potential of the hydrogen gas upon adsorption, we were able to calculate the cohesive van der Waals energy between the tubes as 5 meV/C atom. This is much smaller than expected from previous theoretical work, and shows that defects in the crystal structure cause large suppressions of the cohesive energy. We were able to alter this cohesive energy by changing the state of the material.

Hydrogen desorption and adsorption properties of fullerene materials C₆₀, and C₇₀ and fullerite were measured. Over several cycles of isotherm measurements at 77 K, the hydrogen storage capacities of one of the fullerite samples increased from an initial value of 0.4 wt% for the first cycle to a capacity of 4.2 wt% for the fourth cycle. Correspondingly, the surface area increased from 0.9 m²/gm to 11 m²/gm, and showed a phase transformation, characterized by X-ray powder diffraction. In comparison, two other fullerite samples, prepared by a different procedure, showed no such behavior. Pure C₆₀ and pure C₇₀ were cycled and exhibited small and constant capacities of 0.7 wt% and 0.33 wt%, respectively, as a function of number of cycles. The enhanced storage capacity of fullerite material is tentatively attributed to the presence of C₆₀ oxide.

Compared to SWNT materials, mixed fullerites have much lower cost. If the fullerite instabilities could be controlled to provide a large change in hydrogen adsorption over a narrow range of pressure, as is possible for SWNT materials, fullerites may be candidate materials for some hydrogen storage applications. The relationship between the structure and properties of the mixed fullerite samples remains uncertain, however. Further investigation will be required to identify the origin of the structural instability of fullerites like fullerite #1.

By adding Ni particles onto the sample, the hydrogen storage capacity of fullerite and activated carbon sample was increased. The adsorption of hydrogen on Ni particle can not account for the total increased capacity even by assuming complete coverage of hydrogen molecules on the Ni particle surface.

7.2 Further Work

Theoretically, the likely upper limits of hydrogen adsorption in various forms of carbon can be considered as that under conditions where H_2 molecules are able to form two close-packed layers within each graphite plane, that the atomic ratio of H:C approaches 1:1 (~ 8 wt%). This value is consistent with the capacity of SWNT at 77 K and it is the best capacity among all the materials listed in Table 7.1.

However, capillary effect is possible for the condensation of hydrogen into nanotube. By altering the diameter of SWNT, one may find the capillarity varies, thus optimizing the hydrogen storage capacity. Adding catalyst particles onto SWNT may even improve its hydrogen storage property.

Carbon materials are not promising for the H_2 storage at 300 K. it seems unlikely that carbon nanofiber shows any spectacular H_2 adsorption/desorption properties, thus there is no point in following up with graphite nanofiber works. SWNT's are interesting but expensive for hydrogen storage at 77 K. Fullerenes are cheaper and showed some performance. However, sample-to-sample variation, which was caused by oxidation, will require further work to understand. Carbon supported catalyst system may have promise to service at elevated temperatures. The amount of hydrogen storage is small, but there seems to be an effect worth pursuing in future work.